PCSI-49 Program Overview

Room /Time	Ballroom South
SuA	PCSI-SuA: New Developments in Oxide Materials & Growth
SuE	PCSI-SuE: Probing Exotic Order Parameters with Photoemission Spectroscopy
MoM	PCSI-MoM1: Semiconductor Heterostructures (Growth, Nanostructures & Interfaces) I PCSI-MoM2: 2D Materials and Graphene I
MoA	PCSI-MoA1: Materials for Catalysis, Energy Storage, and Energy Harvesting PCSI-MoA2: Topological Materials & Interfaces I
MoE	PCSI-MoE: Topological Materials & Interfaces II
TuM	PCSI-TuM1: Magnetic Materials (2D, Monolayers, & Heterostructures) PCSI-TuM2: Organic and Hybrid Semiconductor Materials & Interfaces
TuE	PCSI-TuE: Point Defects for Quantum Information Applications
WeM	PCSI-WeM1: Ferroelectric & Neuromorphic Computing Materials PCSI-WeM2: Spin Transport and Spintronics
WeA	PCSI-WeA1: Characterization of Interfaces and Devices PCSI-WeA2: Semiconductor Heterostructures (Growth Nanostructures & Interfaces) II
ThM	PCSI-ThM1: Wide Bandgap Materials PCSI-ThM2: 2D Materials and Graphene II

PCSI
Room Ballroom South - Session PCSI-SuA
New Developments in Oxide Materials & Growth
Moderator: Alex Demkov, The University of Texas

4:00pm	**INVITED: PCSI-SuA-1** Crystal-Chemical Origins of the Ultrahigh Conductivity of Metallic Delafossites, ***Chris Leighton,*** University of Minnesota	
4:40pm	**INVITED: PCSI-SuA-9** Superconductivity and Magnetism in Infinite-Layer Nickelate Heterostructures, ***Jennifer Fowlie,*** SLAC National Lab	
5:20pm	**PCSI-SuA-17** The Redox Chemistry of Oxide Molecular Beam Epitaxy, ***Oliver Bierwagen,*** Paul-Drude-Institut für Festkörperelektronik Leibniz-Institut im Forschungsverbund Berlin, Germany	
5:25pm	**PCSI-SuA-18** Optical Phonon Modes in $LaInO_3$: Lattice Dynamics and Complete Polarization Analysis of Raman-Active Modes, ***Hans Tornatzky,*** Paul-Drude Institute for Solid State Electronics, Germany; *Z. Galazka,* Institut für Kristallzüchtung, Germany; *R. Gillen,* Friedrich-Alexander-University Erlangen-Nürnberg (FAU), Germany; *O. Brand, M. Ramsteiner, M. Wagner,* Paul-Drude Institute for Solid State Electronics, Germany	
5:30pm	**PCSI-SuA-19** Non-Trivial Electronic States in the $EuO/KTaO_3$ Interface Revealed by Quantum Oscillations in High Magnetic Fields, ***K. Rubi,*** Los Alamos National Laboratory; *M. Dumen, S. Chakraverty,* Institute of Nano Science and Technology, India; *S. Zeng, A. Ariando,* National University of Singapore; *M. Chan, N. Harrison,* Los Alamos National Laboratory	
5:35pm		

Sunday Evening, January 14, 2024

PCSI
Room Ballroom South - Session PCSI-SuE
Probing Exotic Order Parameters with Photoemission Spectroscopy
Moderator: Chris Leighton, University of Minnesota

7:30pm	**INVITED: PCSI-SuE-1** Searching for the Excitonic Insulator State in Quantum Materials, ***Edoardo Baldini,*** The University of Texas at Austin	
7:35pm		
7:40pm		
7:45pm		
7:50pm		
7:55pm		
8:00pm		
8:05pm		
8:10pm	**PCSI-SuE-9** Comparative Study on Non-Linear and Linear Least Square Analyses Applied to X-Ray Induced Auger Electron Spectroscopy Transitions, *A. Gagliardi,* CNRS, ILV, France*; N. Fairley,* Casa Software Ltd, UK*;* ***Solene Bechu,*** CNRS, ILV, France	
8:15pm	**PCSI-SuE-10** Probing Electrons and Light in Nanomaterials Using the Photoelectric Effect, ***Taisuke Ohta,*** *A. Boehm, S. Gennaro, C. Doiron, A. Kim, K. Thuermer, J. Sugar, C. Spataru,* Sandia National Laboratories*; J. Fonseca Vega, J. Robinson,* Naval Research Laboratory*; T. Beechem,* Purdue University*; M. Sinclair, I. Brener, R. Sarma,* Sandia National Laboratories	
8:20pm	**INVITED: PCSI-SuE-11** Layer-by-Layer Engineering and Deciphering of Topological Orders in Magnetic Topological Insulators, *W. Lee,* University of Chicago*; S. Fernandez-Mulligan,* Yale University*; H. Tan,* Weizmann Institute of Science, Israel*; C. Yan,* University of Chicago*; Y. Guan, S. Lee, R. Mei, C. Liu,* Pennsylvania State University*; B. Yan,* Weizmann Institute of Science, Israel*; Z. Mao,* Pennsylvania State University*;* ***Shuolong Yang,*** University of Chicago	
8:25pm		
8:30pm		
8:35pm		
8:40pm		
8:45pm		
8:50pm		
8:55pm		

Monday Morning, January 15, 2024

	Room Ballroom South	
8:30am	**INVITED: PCSI-MoM1-1** Mechanisms and Applications for Remote Epitaxy of Heusler Compounds, ***Jason Kawasaki,*** University of Wisconsin - Madison	**PCSI** **Session PCSI-MoM1** **Semiconductor Heterostructures (Growth, Nanostructures & Interfaces) I** **Moderator:** **Kirstin Alberi**, National Renewable Energy Laboratory
9:10am	**PCSI-MoM1-9 UPGRADED:** High-Mobility Two-Dimensional Electron Gas with Quantized States in Polar-Discontinuity Doped $LaInO_3/BaSnO_3$ Heterostructure Grown by Molecular Beam Epitaxy, *G. Hoffmann,* Paul-Drude-Institut für Festkörperelektronik Leibniz-Institut im Forschungsverbund Berlin, Germany; *A. Hartl,* Paul Scherrer Institut, Switzerland; *M. Zupancic,* Leibniz-Institut für Kristallzüchtung, Germany; *A. Riaz,* University College London, UK; *V. Strocov,* Paul Scherrer Institut, Switzerland; *M. Albrecht,* Leibniz-Institut für Kristallzüchtung, Germany; *A. Regoutz,* University College London, UK; ***Oliver Bierwagen,*** Paul-Drude-Institut für Festkörperelektronik Leibniz-Institut im Forschungsverbund Berlin, Germany	
9:30am	**PCSI-MoM1-13** Enabling Direct-Write Fabrication of Low Dimensional Micro- and Nanostructures on Supported and Suspended Substrates, ***Irma Kuljanishvili,*** Saint Louis University	
9:35am	**PCSI-MoM1-14** Silicon (111) - Aluminum (111) - Amorphous Alumina: Asymmetric Quantum Well and Band Alignment, ***Hanran Jin,*** University of Texas at Austin, China; *A. Demkov,* University of Texas at Austin	
9:40am	**PCSI-MoM1-15** Silicene Ribbons: Synthesis, Electronic and Geometric Structure at the Atomic Scale, *A. Costine,* University of Virginia; *Z. Gai,* Orak Ridge National Laboratory; ***Petra Reinke,*** University of Virginia	
9:45am	**PCSI-MoM1-16** Spontaneous Growth of Silver on Si(001) Tuned by Substrate Temperature, ***Xiaohang Huang,*** *K. Huang,* Guangdong Technion - Israel Institute of Technology, China	
9:50am	**Coffee Break & Poster Viewing**	
11:00am	**INVITED: PCSI-MoM2-31** Interplay of Valley Polarized Dark Trion and Dark Exciton-Polaron in Monolayer WSe_2, ***Xiao-Xiao Zhang,*** University of Florida	**PCSI** **Session PCSI-MoM2** **2D Materials and Graphene I** **Moderator:** **Robert Wallace,** University of Texas at Dallas
11:40am	**PCSI-MoM2-39** Evidence of Single Photon Emitters from 1L WSe_2 under Electrostatically Induced Strain, ***Frances Camille Wu,*** *S. Wu, B. Fang, X. Li, J. Incorvia, E. Yu,* The University of Texas at Austin	
11:45am	**PCSI-MoM2-40** Comprehensive Study of Interface Chemistry and Electrical Property of Metal Contacts on TMDs, *S. Kim,* ***Joy Roy,*** *X. Wang, R. Wallace,* University of Texas at Dallas	
11:50am	**PCSI-MoM2-41** Transport Anisotropy in One-dimensional Graphene Superlattice in the High Kronig-Penney Potential Limit, ***Tianlin Li,*** *H. Chen, K. Wang, Y. Hao, L. Zhang,* University of Nebraska - Lincoln; *K. Watanabe, T. Taniguchi,* National Institute for Materials Science, Japan; *X. Hong,* University of Nebraska - Lincoln	
11:55am	**PCSI-MoM2-42** Excitons, Electrons, and Holes in Monolayer Semiconductors: Insights from Spectroscopy in (Really) High Magnetic Fields, ***Scott Crooker,*** National High Magnetic Field Lab	
12:00pm		

Monday Afternoon, January 15, 2024

	Room Ballroom South	
2:00pm	**INVITED: PCSI-MoA1-1** Interface Control of III-Nitride Semiconductors: From High Efficiency Artificial Photosynthesis to Ferroelectric Switching, ***Zetian Mi***, University of Michigan, Ann Arbor	**PCSI** **Session PCSI-MoA1** **Materials for Catalysis, Energy Storage, and Energy Harvesting** **Moderator: Edward Yu**, The University of Texas at Austin
2:40pm	**PCSI-MoA1-9 UPGRADED:** Wafer-Scale Si-Based Metal-Insulator-Semiconductor Photoanodes for Water Oxidation Fabricated Using Thin Film Reactions and Electrodeposition, ***Shang-Hsuan Wu***, *S. Lee, Y. Choi, E. Yu,* The University of Texas at Austin	
3:00pm	**PCSI-MoA1-13 UPGRADED:** Field-Assisted Oxidation of a Fe Single Nanoparticle, Nanoscale Observations by Operando Atom Probe, ***Sten V Lambeets***, Pacific Northwest National Laboratory*; N. Cardwell, I. Onyango,* Washington State University*; T. Visart de Bocarmé,* Université Libre de Bruxelles, Belgium*; J. McEwen,* Washington State University*; D. Perea,* Pacific Northwest National Laboratory	
3:20pm	**Coffee Break & Poster Viewing**	
4:30pm	**INVITED: PCSI-MoA2-31** Crystalline Materials with Anisotropic Conduction Polarities, ***Joshua Goldberger***, The Ohio State University	**PCSI** **Session PCSI-MoA2** **Topological Materials & Interfaces I** **Moderator:** **Jun Sung Kim**, Pohang University of Science and Technology (POSTECH), Republic of Korea
5:10pm	**PCSI-MoA2-39** Weyl Semimetals and the Interface: Surface State Transport Probed via Weak Antilocalization in Ultrathin Taas Films, ***Ian Leahy***, *A. Rice, C. Jiang, G. Paul, K. Alberi,* National Renewable Energy Laboratory*; J. Nelson,* National Renewable Energy Laboratory	
5:15pm	**PCSI-MoA2-40** Topological Hall Effect in Dirac Semimetal, ***Saurav Islam***, *E. Steinebronn,* Pennsylvania State University*; B. Neupane,* University of North Texas*; K. Yang,* Pennsylvania State University*; Y. Wang,* University of North Texas*; C. Liu,* Pennsylvania State University*; S. Ghosh,* University of Minnesota*; K. Mkhoyan,* University of Minho, Portugal*; J. Chamorro, T. McQueen,* Johns Hopkins University*; N. Samarth,* Pennsylvania State University	
5:20pm	**PCSI-MoA2-41** Helical Dislocations in 2D Materials and the Connection to Transport in Topological Insulators, *T. Rakib, M. Choi, E. Ertekin,* University of Illinois at Urbana-Champaign*; P. Pochet,* Universite Grenoble-Alpes, France*;* ***Harley Johnson***, University of Illinois at Urbana-Champaign	
5:25pm	**PCSI-MoA2-42** Layer-dependent Optical Conductivity of MBE-grown $ZrTe_2$, *E. Houser,* ***Frank Peiris***, Kenyon College*; A. Richardella, M. Stanley, N. Samarth,* Pennsylvania State University	
5:30pm	**PCSI-MoA2-43** Surface Dependent Doping Efficiency in Te:Cd_3As_2 Thin Films, ***Anthony Rice***, *I. Leahy,* National Renewable Energy Laboratory*; K. Alberi,* National Renewable Energy Laboratory	
5:35pm	**PCSI-MoA2-44** Investigating the Structural and Electronic Properties of FeSn on $LaAlO_3$ (111) Grown by Molecular Beam Epitaxy, *T. Erickson,* ***Sneha Upadhyay***, *A. Shrestha, A. Abbas, H. Hall, D. Ingram, S. Kaya, A. Smith,* Ohio University	
5:40pm	**PCSI-MoA2-45** Ultra-quantum Limit Magnetotransport in the Topological Pentatellurides, ***Johanna Palmstrom***, *C. Ribeiro, C. Mizzi, L. Winter, S. Thomas,* Los Alamos National Laboratory*; J. Liu, L. Jauregui,* University of California Irvine*; J. Mutch, Q. Jiang, J. Ayres-Sims, J. Chu,* University of Washington*; E. Peterson, J. Zhu,* Los Alamos National Laboratory	

PCSI
Room Ballroom South - Session PCSI-MoE
Topological Materials & Interfaces II
Moderator: Joshua Goldberger, The Ohio State University

7:30pm	**INVITED: PCSI-MoE-1** Large Magnetotransport Responses and Spintronic Functionalities of Topological van der Waals Ferromagnets, ***Jun Sung Kim***, Pohang University of Science and Technology (POSTECH), Republic of Korea	
8:10pm	**PCSI-MoE-9** Epitaxial Kagome Thin Films as a Platform for Topological Flat Bands and Dirac Cones, *S. Cheng, M. Nrisimhamurty,* Ohio State University*; T. Zhou,* University at Buffalo*; N. Bagues, W. Zhou, A. Bishop, I. Lyalin,* Ohio State University*; C. Jozwiak, A. Bostwick, E. Rotenberg,* Advanced Light Source, Lawrence Berkeley National Laboratory*; D. McComb,* Ohio State University*; I. Zutic,* University at Buffalo*;* ***Roland Kawakami****,* Ohio State University	
8:15pm	**PCSI-MoE-10** Kagome Antiferromagnetic Mn_3GaN grown on MgO(001) using Molecular Beam Epitaxy*, A. Abbas***,** *A. Smith,* ***Ashok Shrestha****, S. Upadhyay, T. Erickson,* Ohio University*; K. Sun,* University of Michigan*; D. Ingram,* Ohio University	
8:20pm	**PCSI-MoE-11** Investigation of Smooth Epitaxial Growth of Mn_3Sn Films on *C*-Plane GaN Using Molecular Beam Epitaxy*,* ***Sneha Upadhyay****, H. Hall, C. D'Mello,* Ohio University*; J. Hernandez,* Universidad Autonoma de Puebla, Mexico*; T. Erickson,* Ohio University*; K. Sun,* The University of Michigan, Ann Arbor*; G. Cocoletzi,* Universidad Autonoma de Puebla, Mexico*; N. Takeuchi,* Universidad Nacional Autónoma de México*; A. Smith,* Ohio University	
8:25pm	**PCSI-MoE-12** Symmetry Constraints on Topological Invariants*,* ***Jing Zhang****,* Imperial College London, UK	
8:30pm	**PCSI-MoE-13 UPGRADED:** Tuning the Curie Temperature of a 2D Magnet/Topological Insulator Heterostructure to Above Room Temperature by Epitaxial Growth*,* ***Wenyi Zhou****, A. Bishop,* The Ohio State University*; X. Zhang,* Cornell University*; K. Robinson, I. Lyalin, Z. Li, R. Bailey-Crandell,* The Ohio State University*; T. Cham,* Cornell University*; S. Cheng,* The Ohio State University*; Y. Luo,* University of Southern California*; D. Ralph, D. Muller,* Cornell University*; R. Kawakami,* The Ohio State University	

Tuesday Morning, January 16, 2024

	Room Ballroom South	
8:30am	**INVITED: PCSI-TuM1-1** Efficient Control of 2D Magnets, ***Cheng Gong,*** University of Maryland, College Park	**PCSI** **Session PCSI-TuM1** **Magnetic Materials (2D, Monolayers, & Heterostructures)** **Moderator:** **Xiao-Xiao Zhang**, University of Florida
9:10am	**INVITED: PCSI-TuM1-9** Surface-Bulk Difference in van der Waals Magnets, ***Liuyan Zhao,*** University of Michigan, Ann Arbor	
9:50am	**PCSI-TuM1-17** Surface Investigation of Hexagonal Non-Collinear $D0_{19}$-Mn_3Ga Thin Film on Gan(0001) Substrate, ***Ashok Shrestha,*** *A. Abbas, D. Ingram, A. Smith,* Ohio University	
9:55am	**PCSI-TuM1-18** Enhancement of Microwave to Optical Spin-Based Quantum Transduction via a Magnon Mode, ***Tharnier O. Puel,*** Department of Physics and Astronomy, University of Iowa; *A. T. Turflinger, S. P. Horvath, J. D. Thompson,* Department of Electrical Engineering, Princeton University; *M. E. Flatté,* Department of Physics and Astronomy, University of Iowa, Department of Applied Physics, Eindhoven University of Technology, Eindhoven, The Netherlands	
10:00am	**PCSI-TuM1-19** Magnetic Modulation and Large Magnetoresistance in Cr_5Te_8, *M. Vaninger, S. Kelley,* University of Missouri; *F. Ye,* Oak Ridge Natinal Laboratory; *X. Zhang,* Nanjing University, China; *T. Heitmann,* University of Missouri; *A. Mazza,* Los Alamos National Laboratory; *Y. Hor, A. Sarikhani,* Missouri S&T; *G. Bian,* ***Paul Miceli,*** University of Missouri	
10:05am	**Coffee Break & Poster Viewing**	
11:00am	**PCSI-TuM2-31** Development of Surface Chemistry on-Top of Organic Semiconductor Thin Films to Improve Optoelectronic Devices, ***Jacob W. Ciszek,*** Loyola University Chicago	**PCSI** **Session PCSI-TuM2** **Organic and Hybrid Semiconductor Materials & Interfaces** **Moderator:** **Wanyi Nie**, Los Alamos National Laboratory
11:05am	**PCSI-TuM2-32** Characterizing Nanopattern Formation of Polymer Thin Films on Silicon Substrates with Ion Beam Sputtering, ***Jocelyn Zhang,*** Boston University, Del Norte High School; *G. Pettis,* Oregon State University, Boston University; *B. Jiang,* Boston University, Turkey; *N. Baker,* Boston University; *E. Guney,* Sabanci University, Turkey; *G. Ince,* Sabanci University IICEC, Turkey; *K. Ludwig, Jr.,* Boston University	
11:10am	**PCSI-TuM2-33** Functionalizing Organic Semiconductors with Dipole Monolayers, ***Matthew Williams,*** Loyola University Chicago	
11:15am	**INVITED: PCSI-TuM2-34** Catching the Sun and Beyond: The Development of Perovskites for Efficient Photovoltaic and Detector Applications, ***Amanda Neukirch,*** Los Alamos National Laboratory	
11:55am		

PCSI
Room Ballroom South - Session PCSI-TuE
Point Defects for Quantum Information Applications
Moderator: Roland Kawakami, The Ohio State University

7:00pm	**INVITED: PCSI-TuE-1** Rare Earth Doped Oxide Thin Films on Silicon for Chip Scale Quantum Emitters and Memories, ***Supratik Guha,*** *D. Awschalom,* University of Chicago, Argonne National Laboratory*; C. Ji, G. Grant, S. Seth, I. Masiulionis,* University of Chicago*; A. Dibos, J. Zjang,* Argonne National Laboratory*; S. Chattaraj,* University of Chicago*; M. Singh,* University of Chicago, memQ*; J. Wen,* Argonne National Laboratory	
7:40pm	**INVITED: PCSI-TuE-9** Erbium sites in Silicon for Quantum Information Processing, ***Sven Rogge,*** University of New South Wales, Australia	

	Room Ballroom South	
8:30am	**INVITED: PCSI-WeM1-1** Emergent Phenomena at Ferroelectric/van der Waals Heterointerfaces, ***Xia Hong***, University of Nebraska - Lincoln	**PCSI** **Session PCSI-WeM1** **Ferroelectric & Neuromorphic Computing Materials** **Moderator:** **Alec Talin**, Sandia National Laboratories
9:10am	**PCSI-WeM1-9** Impact of High-Power Impulse Magnetron Sputtering Pulse Width on the Nucleation, Crystallization, Microstructure, and Ferroelectric Properties of Hafnium Oxide Thin Films, ***Samantha Jaszewski***, Sandia National Laboratories	
9:15am	**PCSI-WeM1-10** Fabrication and Gamma Radiation Effects on Endurance of Ferroelectric Hafnium Zirconium Oxide Capacitors, ***M. David Henry***, Sandia National Laboratories; *M. Lenox,* University of Virginia; *A. Hillsman,* North Carolina State University; *S. Jaszewski, G. Esteves,* Sandia National Laboratories, USA; *J. Jones,* North Carolina State University; *J. Ihlefeld,* University of Virginia	
9:20am	**INVITED: PCSI-WeM1-11** Design of Memristive Devices Towards Neuromorphic Computing, ***Aiping Chen***, Los Alamos National Laboratory	
10:00am		
10:05am	**PCSI-WeM1-20** Neuromorphic Memristors with TiO_2 and a-IGZO Bilayer Structure, ***Jae-Yun Lee***, College of Electrical and Computer Engineering, Chungbuk National University, South Korea; *H. Zhao, X. Wang, S. Shi,* College of Electrical and Computer Engineering, Chungbuk National University, South Korea, China; *B. Lee, S. Kim,* College of Electrical and Computer Engineering, Chungbuk National University, South Korea	
10:10am	**PCSI-WeM1-21** Origin of Large Electro-Optic Response in Ferroelectrics, ***Alex Demkov***, *I. Kim, T. Paoletta, S. Apte,* The University of Texas at Austin	
10:15am	**Coffee Break & Poster Viewing**	
11:00am	**INVITED: PCSI-WeM2-31** Direct Visualization of Electronic Transport in a Quantum Anomalous Hall Insulator, ***Katja Nowack***, Cornell University	**PCSI** **Session PCSI-WeM2** **Spin Transport and Spintronics** **Moderator: Ezekiel Johnston-Halperin**, The Ohio State University
11:40am	**PCSI-WeM2-39** Magneto-Optical Detection of the Orbital Hall Effect in Chromium, ***Igor Lyalin***, *R. Kawakami,* The Ohio State University	
11:45am	**PCSI-WeM2-40** Temperature Dependent Study of Na_xSi_{136} Type II Si Clathrate Spin Dynamics, ***Joseph Briggs***, *Y. Liu, S. Saiter, A. Faricy, C. Burns, C. Taylor, M. Singh, R. Collins, C. Koh,* Colorado School of Mines	
11:50am	**PCSI-WeM2-41** Spin-orbit coupling in InGaAs random and digital alloy quantum wells, ***Jason Dong***, University of California at Santa Barbara; *Y. Gul,* University College London, UK; *A. Engel, C. Dempsey,* University of California at Santa Barbara; *T. van Schijndel,* University of California Santa Barbara; *M. Pepper,* University College London, UK; *C. Palmstrøm,* University of California at Santa Barbara	
11:55am	**PCSI-WeM2-42** Screw Dislocations-Based Spin Valves, ***Finley Haines***, *E. Renteria, M. Debasu, F. Cavallo,* University of New Mexico	

Wednesday Afternoon, January 17, 2024

	Room Ballroom South	
2:00pm	**INVITED: PCSI-WeA1-1** Imaging the Properties of Atoms and Fields at the Picometer Scale inside Materialsand Devices, ***David Muller***, Cornell University	**PCSI** **Session PCSI-WeA1** **Characterization of Interfaces and Devices** **Moderator: Paul M. Koenraad**, Eindhoven University of Technology, Netherlands
2:40pm		
2:45pm	**PCSI-WeA1-10** Cryogenic Growth and *in-Situ* Fabrication of Superconducting Tantalum Devices, ***Teun van Schijndel***, UC Santa Barbara; *A. McFadden,* NIST-Boulder; *A. Engel, J. Dong, S. Chatterjee,* UC Santa Barbara; *R. Simmonds,* NIST-Boulder; *C. Palmstrøm,* UC Santa Barbara	
2:50pm	**PCSI-WeA1-11** Multi-Technique Characterization of GaN-Based Devices: A Powerful Tool to Probe the in-Depth Chemistry, ***Kirène Gaffar***, CNRS, Université Paris-Sud, France; *S. Béchu, G. Patriarche, M. Bouttemy,* CNRS, France	
2:55pm	**PCSI-WeA1-12** Mo-SiN_x Granular Metal High-pass Filters, ***Laura Biedermann***, *M. McGarry, S. Gilbert, W. Bachman, M. Meyerson, L. Yates, P. Sharma, J. Flicker, P. Kotula, M. Siegal,* Sandia National Laboratories	
3:00pm	**PCSI-WeA1-13** Restructuring Cracks in Rutile TiO_2 with Radiolysis-Driven Rolling of Octahedral Units, ***Silu Guo***, *H. Yun, S. Nair, B. Jalan, K. Mkhoyan,* University of Minnesota, USA	
3:05pm	**PCSI-WeA1-14 UPGRADED:** Growth and Angle-Resolved Photoemission of Strain- and Thickness- Tuned Epitaxial α-Sn Thin Films, ***Aaron Engel***, *H. Inbar,* University of California, Santa Barabara; *P. Corbae, C. Dempsey, S. Nishihaya, Y. Chang,* University of California, Santa Barbara; *A. Fedorov,* Advanced Light Source, Lawrence Berkeley National Laboratory; *M. Hashimoto, D. Lu,* SLAC National Accelerator Laboratory; *C. Palmstrøm,* University of California, Santa Barbara	
3:25pm	**PCSI-WeA1-18** Characterization of Buffer Layers for Remote Plasma-Enhanced Chemical Vapor Deposition of Germanium-Tin Epitaxial Layers, ***Stefan Zollner***, *C. Armenta,* New Mexico State University; *B. Rogers,* Vanderbilt University; *G. Grzybowski, B. Claflin,* Air Force Research Laboratory	
3:30pm	**PCSI-WeA1-19** Near Zero-Field Magnetoresistance and Defects in GaN pn Junctions, *M. Elko, A. Higgins, D. Hassenmayer,* ***Patrick Lenahan***, Pennsylvania State University; *M. Flatte, D. Fehr,* University of Iowa; T.D. Larsen, M.D. Craven, NexGen Power Systems	
3:35pm	**Coffee Break & Poster Viewing**	
4:30pm	**INVITED: PCSI-WeA2-31** Heteroepitaxy of PbSe-SnSe Semiconductors on GaAs for Infrared Optoelectronics, ***Kunal Mukherjee***, Stanford University	**PCSI** **Session PCSI-WeA2** **Semiconductor Heterostructures (Growth Nanostructures & Interfaces) II** **Moderator: Jason Kawasaki**, University of Wisconsin - Madison
5:10pm	**PCSI-WeA2-39** Investigation of Localized Electric Fields of InAs/GaAs Quantum Dot Interfaces, *T.I. Kang*, ***Jong Su Kim***, Department of Physics, Yeungnam University; *S. Lee,* Division of Convergence Technology, Korea Research Institute of Standards and Science	
5:15pm	**PCSI-WeA2-40** X-STM Study of Interlayer Effects on InAs Quantum Dots in InP, ***Edoardo Guido Banfi***, Eindhoven University of Technology, Netherlands; *E. Sala,* Sheffield University, UK; *R. Gajjela,* Eindhoven University of Technology, Netherlands; *J. Heffernan,* Sheffield University, UK; *P. Koenraad,* Eindhoven University of Technology, Netherlands	
5:20pm	**PCSI-WeA2-41 UPGRADED:** Atomic Scale Analysis of N Dopants in InAs, *T. Verstijnen, D. Tjeertes, E. Banfi,* Eindhoven University of Technology, Netherlands; *Q. Zhuang,* Lancaster University, UK; ***Paul Koenraad***, Eindhoven University of Technology, Netherlands	
5:40pm	**PCSI-WeA2-45** Direct Wafer Bonding of GaN on AlN Through the Optimization of Chemical Mechanical Polishing, ***Kaicheng Pan***, *K. Huynh, M. Li, Y. Ge, T. Fisher, Y. Hu, M. Goorsky,* UCLA	
5:45pm	**PCSI-WeA2-46** Strategies for Analyzing Non-Common-Atom Heterovalent Interfaces: The Case of CdTe-on-InSb, ***Esperanza Luna***, *A. Trampert,* Paul-Drude-Institut für Festkörperelektronik Leibniz-Institut im Forschungsverbund Berlin, Germany; *J. Lu, T. Aoki, Y. Zhang, M. McCartney, D. Smith,* Arizona State University	
5:50pm	**PCSI-WeA2-47** Multi-Material Deposition for Spatial Atomic Layer Deposition Process, ***Simone Santucci***, *M. Baraket, A. Varga, M. Carnoy, M. Plakhotnyuk, I. Kundrata,* ATLANT 3D, Denmark; *J. Bachmann,* Friedrich-Alexander-University Erlangen-Nürnberg (FAU), Germany	

Thursday Morning, January 18, 2024

	Room Ballroom South	
8:30am	**INVITED: PCSI-ThM1-1** Surface Transfer - Modulation Doping at a Diamond-Dielectric Interface, ***Robert Nemanich,*** Arizona State University	**PCSI** **Session PCSI-ThM1** **Wide Bandgap Materials** **Moderator: Christopher Palmstrøm**, University of California, Santa Barbara
9:10am	**INVITED: PCSI-ThM1-9** Operation-Induced Short-Term Degradation Mechanisms of 275-Nm-Band AlGaN-Based Deep-Ultraviolet Light-Emitting Diodes Fabricated on a Sapphire Substrate, ***Shigefusa Chichibu,*** Tohoku University, Japan*; K. Okuno, M. Oya, Y. Saito, H. Ishiguro,* Toyoda Gosei Co. Ltd., Japan*; T. Takeuchi,* Meijo University, Japan*; K. Shima,* Tohoku University, Japan	
9:50am	**PCSI-ThM1-17** Impact of Interfacial Defects and Lattice Strain on NbN_x Films for Integration with Wide Bandgap Semiconductors, ***Annaliese Drechsler,*** University of Maryland College Park*; P. Shea,* Northrop Grumman*; A. Christou,* University of Maryland College Park	
9:55am	**PCSI-ThM1-18** Impact of Unintentional Boron Supply on Sapphire Nitridation Process for GaN Growth by Rf-MBE, ***Tohru Honda,*** *K. Yajima, T. Yayama, T. Onuma, T. Yamaguchi,* Kogakuin University, Japan	
10:00am	**PCSI-ThM1-19** Photoluminescence Maps of Surface Defects in β-Ga_2O_3, ***Matthew McCluskey,*** Washington State University*; J. Huso,* Klar Scientific*; C. Remple, J. McCloy,* Washington State University*; S. Rebollo, S. Krishnamoorthy, J. Speck,* University of California at Santa Barbara	
10:05am	**PCSI-ThM1-20 UPGRADED:** Epitaxial Growth and Properties of Wide Bandgap *P*-Type $NiGa_2O_4$ on *β*-Ga_2O_3 for High Voltage *P-N* Heterojunctions with Superior Performance at Elevated Temperatures, ***Kingsley Egbo,*** *B. Tellekamp, W. Callahan, A. Zakutayev,* National Renewable Energy Laboratory	
10:25am	**PCSI-ThM1-24** Quantum Oscillations in GaN/AlN 2D Hole Gas and Extraction of Light Hole Effective Mass, ***Chuan Chang,*** *J. Dill, Z. Zhang,* Cornell University*; S. Crooker, O. Valenzuela, R. McDonald,* Los Alamos National Laboratory*; D. Jena, G. Xing,* Cornell University	
10:30am	**Coffee Break & Poster Viewing**	
11:00am	**PCSI-ThM2-31 UPGRADED:** Reduced Metal Contact Resistances for Moire MoS_2 Interfaces, ***John Robertson,*** Cambridge University, UK	**PCSI** **Session PCSI-ThM2** **2D Materials and Graphene II** **Moderator: Scott Crooker**, Los Alamos National Laboratory
11:20am	**PCSI-ThM2-35 UPGRADED:** A Generalized and Modular Approach to Tunnel-Junction Spectroscopy for Quantum Systems, *M. Kavand, Z. Phillips, M. Hamilton, E. Perez-Hoyos,* The Ohio State University*; D. Freedman,* Massachusetts Institute of Technology*; M. Flatté,* University of Iowa*; J. Gupta,* ***Ezekiel Johnston-Halperin,*** The Ohio	

Author Index

Bold page numbers indicate presenter

Author Index

Superconductivity and magnetism in infinite-layer nickelate heterostructures

J. Fowlie[1,2]

[1] *Stanford Institute for Materials and Energy Sciences, SLAC National Lab, 2575 Sand Hill Road, Menlo Park, CA 94025*

[2] *Department of Applied Physics, Stanford University, 476 Lomita Mall, Stanford, CA 94305*

Nickel and copper are nominally very similar in chemistry so the search for superconductivity in nickelates is a story as old as the quest to understand the high temperature superconductivity of the cuprates.

In this talk, I will introduce the recent discovery of superconductivity in infinite-layer nickelates [1] and the ever-growing family of nickelate superconductors. I will touch on some of the materials challenges involved before summarizing the key physics we have learned so far including results from x-ray scattering [2] that identify a Mott-Hubbard-like character to the infinite-layer nickelate electronic structure as well as a significant rare earth 5d influence at the Fermi level. In particular I will focus on muon spin rotation [3] that reveals local magnetism in these materials that 1) onsets at rather high temperature, 2) is independent of the rare earth 4f electrons, 3) appears to be robust to doping 4) is antiferromagnetic and possibly short-range-ordered in nature and 5) coexists with superconductivity at low temperatures.

Finally, I will come back to the comparison between nickelates and cuprates and discuss how the disparities in the magnetic properties may be understood.

[1] D. Li et al, Nature **572**, 624 (2019).
[2] H. Lu et al, Science **373**, 213 (2021).
[3] J. Fowlie et al, Nat. Phys. **18**, 1043 (2022).

[+] Author for correspondence: jfowlie@stanford.edu

The redox chemistry of oxide molecular beam epitaxy

O. Bierwagen[1]

[1] *Paul-Drude-Institut für Festkörperelektronik, Leibniz-Institut im Forschungsverbund Berlin e.V., Hausvogteiplatz 5 – 7, 10117 Berlin, Germany*

The materials class of crystalline oxides provides a plethora of functional (dielectric, semiconducting, superconducting, ferroelectric, or ferromagnetic) properties. For harnessing this potential, molecular beam epitaxy (MBE) has proven an established method that realizes high quality oxide thin films. In its mostly used variety, the corresponding cation is evaporated from an effusion cell in vacuum onto the heated substrate where it gets oxidized by molecular oxygen, ozone, or an oxygen plasma.

This contribution will review the peculiar redox chemistry of oxide MBE, related to the existence of suboxides with significantly higher vapor pressure than their cation elements, not only taking place at the growth surface but also in effusion cells. I will discuss the implications of this chemistry on growth rate, film composition, and flux emanating from the effusion cells with the example of the plasma-assisted MBE growth of the semiconducting oxides Ga_2O_3, In_2O_3, GeO_2, SnO_2 and its suboxide SnO. Three major reactions describe the suboxide-related chemistry:

(1.) The reaction of the metal with its oxide towards the suboxide, which can be utilizied to etch oxide films in-situ [1,6], but also provides efficient suboxide sources [2].

(2.) The reaction of the cation element with oxygen, resulting in unintentional suboxide fluxes from elemental sources, leading to unexpectedly high cation incorporation in the grown films [3]. On the substrate, the same reaction provides the *p*-type oxide SnO [4] as well as an efficient way of removing a cation layer in-situ. Generally, the suboxide formation on the growth front is the first step during oxide growth, its desorption limits the growth rate.

(3.) The reaction of the suboxide with activated oxygen in the source leads to source passivation [9]. On the growth front, it is the second step that completes oxide growth. A kinetic growth model that involves both these steps, describes the observed, peculiar growth rate dependence on metal-to-oxygen flux ratio and substrate temperature for SnO_2, Ga_2O_3, In_2O_3 [5], and GeO_2 [6]. A simpler, single- and zero-step growth kinetics can be realized when the suboxide instead of an elemental cation flux is provided to the growth front, as demonstrated for SnO_2 [2], Ga_2O_3 [7], and SnO [8] films grown by suboxide MBE (S-MBE).

[1] P. Vogt, O. Bierwagen, Appl. Phys. Lett. **106**, 081910 (2015).
[2] G. Hoffmann, M. Budde, P. Mazzolini, O. Bierwagen, APL Mater. **8**, 031110 (2020).
[3] G. Hoffmann, Z. Cheng, O. Brandt, O. Bierwagen, APL Mater. **9**, 111110 (2021).
[4] M. Budde et al., Phys. Rev. Mater. **4**, 124602 (2020).
[5] P. Vogt, O. Bierwagen, Phys. Rev. Mater. **2**, 120401(R) (2018).
[6] W. Chen et al. APL Mater. **11**, 071110 (2023).
[7] P. Vogt et al., APL Mater. **9**, 031101 (2020).
[8] K. Egbo et al., J. Appl. Phys. **133**, 045701 (2023).
[9] A. Ardenghi et al., Appl. Phys. Lett. **121**, 042109 (2022).

[+] Author for correspondence: bierwagen@pdi-berlin.de

Optical phonon modes in $LaInO_3$: Lattice dynamics and complete polarization analysis of Raman-active modes

H. Tornatzky[1], Z. Galazka[2], R. Gillen[3], O. Brandt[1], M. Ramsteiner[1], M. R. Wagner[1]
[1] *Paul-Drude-Institute for Solid State Electronics, Hausvogteiplatz 5–7, 10117 Berlin Germany*
[2] *Leibniz-Institut for Crystal Growth, Max-Born-Str. 2, 12489 Berlin, Germany*
[3] *Friedrich-Alexander University Erlangen-Nuremberg, Staudtstrasse 7, 91058 Erlangen, Germany*

$LaInO_3$ is part of the family of ABO_3 perovskites, and is considered promising for next generation devices, such as for power electronics, due to its band gap of about 4.5 eV. A detailed knowledge of phonon modes in $LaInO_3$ is important as they determine a number of material properties, such as the mechanical and elastic properties, thermal transport and carrier dynamics, phonon-assisted optical excitations, and many more. However, little is known about the vibrational properties of this material. In this study, we investigate the lattice dynamics by polarization- and angle-resolved Raman spectroscopy and density functional theory (DFT). We experimentally observe all but one of the Raman active modes and compare them to our simulated values from DFT. Furthermore, we present the DFT-derived phonon dispersion relation along the high symmetry directions in reciprocal space and depict the oscillation patterns for selected phonons at the Γ point. Finally, we determine the relative Raman tensor elements of the observed modes from the angular dependence of their corresponding scattering efficiencies (cf. Fig. 2).

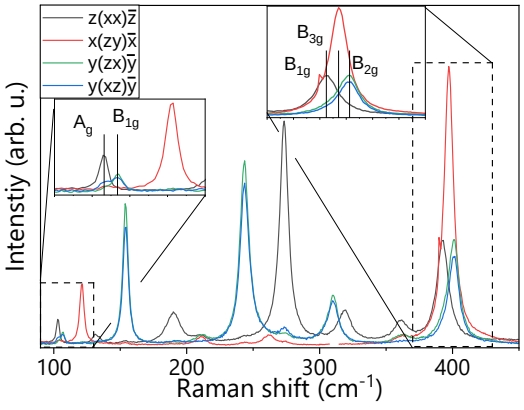

Figure 1: Polarized Raman spectra allow to distinguish overlapping modes based on their symmetry (see insets).

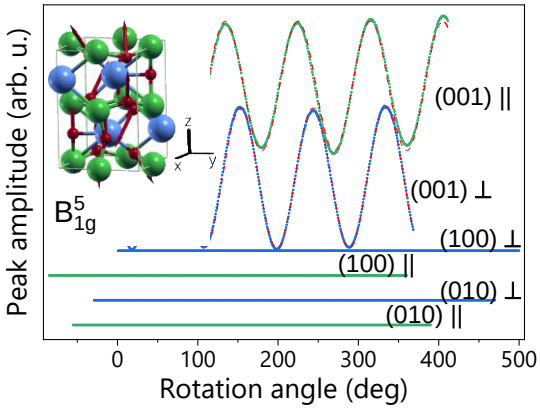

Figure 2: Angle resolved peak amplitude of the B^5_{1g} mode for different scattering configurations (vertically offset). Blue and green symbols depict the measurement, red dashed lines depict the fit.

+ Author for correspondence: Tornatzky@PDI-Berlin.de

Supplementary Pages

Figure 3 shows the polarized Raman spectra on the (100), (010) and (100) faces of macroscopic melt-grown crystals. The coordinate system *xyz* is chosen to be parallel to the a, b and c lattice vectors. By careful analysis of the polarization resolved spectra, one can identify 23 of the 24 active Raman modes, of which many overlap and are indistinguishable in unpolarized measurements. The positions of all observed modes are indicated by vertical dashed lines in Fig. 3. The remaining mode is expected to be either obscured by a mode of the same symmetry or very weak in intensity.

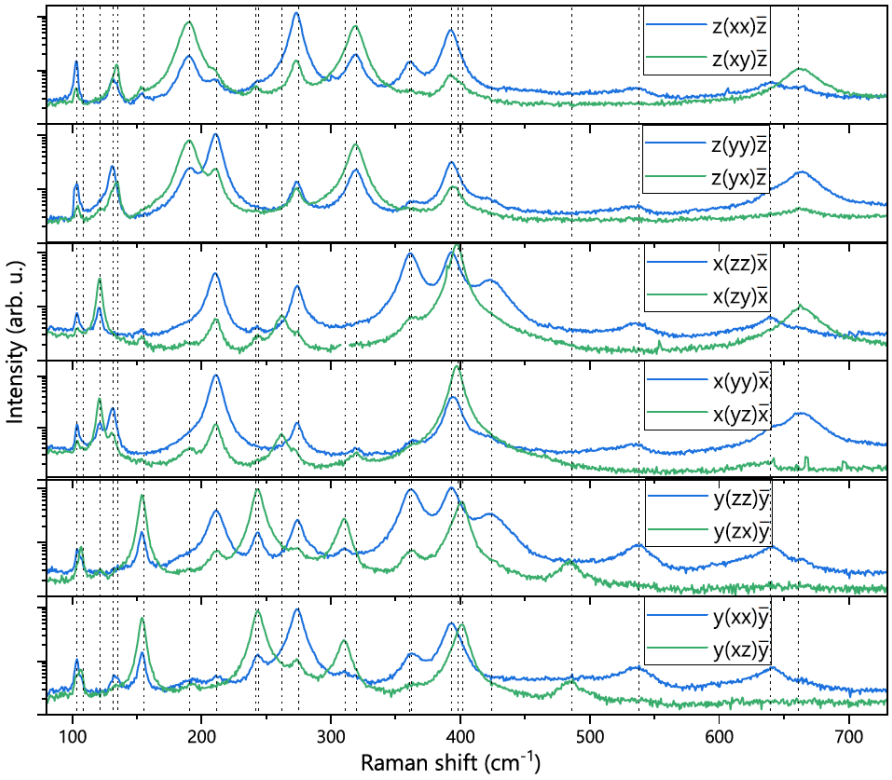

Figure 3: Polarization-resolved Raman spectra of $LaInO_3$ with scattering direction and polarization parallel to the lattice vectors (scattering geometry is given in Porto notation). Vertical dashed lines indicate the position of observed Raman active phonon modes.

DFT as implemented in the Quantum Espresso-suite [1] was used with Perdew-Burke-Ernzerhof functionals to calculate the phonon dispersion and derive the oscillation patterns of the phonon modes at the Γ point. Norm conserving ultra-soft pseudopotentials were used with a kinetic cutoff-energy of 80 Ry (800 Ry) for the wave function (charge density and potential). Both, electronic and vibrational properties were calculated on a regular 6 × 6 × 4 k/q-grid pattern. The obtained lattice parameters of a = 5.776 Å, b = 6.015 Å and c = 8.348 Å are in good agreement with values measured by x-ray diffraction. Figure 4 shows the obtained phonon dispersion along the high-symmetry path ΓXSYΓZURTZ|UX|SR|YT (cf. inset). The obtained phonon energies are generally in good agreement with the experiment, but deviate for some modes, especially for the high frequency modes. This deviation is considered as an effect of a nonideal oxygen pseudopotential. The results from DFT further suggest that the final mode to be observed experimentally is the B^3_{3g} mode which is nearly degenerate with the A^6_g mode. Further analysis of the data will be needed to potentially distinguish these two lines. The phonon density of states has been calculated on a regular 50×50×50 q-point grid and is depicted in the right panel of Fig. 4.

Non-trivial electronic states in the EuO/$KTaO_3$ interface revealed by quantum oscillations in high magnetic fields

K. Rubi,[1*] **M. Dumen**,[2] **S. Chakraverty**,[2] **S. Zeng**,[3] **A. Ariando**,[3] **M. Chan**,[1] **N. Harrison**[1]

[1] *MPA-MAGLAB, Los Alamos National Laboratory, Los Alamos, NM 87545, USA*
[2] *Quantum Materials and Devices Unit, Institute of Nano Science and Technology, Mohali, Punjab 140306, India*
[3] *Department of Physics, National University of Singapore, 117551 Singapore*

The coexistence of electric-field controlled superconductivity and spin-orbit interaction in two-dimensional electron gas (2DEG) based on complex oxides (e.g., $SrTiO_3$ and $KTaO_3$) hold great promise for advancement in spintronics and quantum computing. However, a comprehensive understanding of the electronic bands that give rise to the multifunctional character of these 2DEGs remains elusive. To address this, we recently investigated quantum oscillations in the magnetoresistance of the $KTaO_3$-2DEG in high magnetic fields (60 T).

$KTaO_3$ is a 5*d* transition metal oxide, exhibiting a lighter effective mass of electrons and a stronger spin-orbit interaction at its conducting surface/interface than its counterpart $SrTiO_3$ [1-2]. A high-mobility spin-polarized 2DEG with the superconducting feature is discovered at the EuO/$KTaO_3$ interface [3]. In this talk, I will present novel insights into the electronic states of the EuO/$KTaO_3$ interface investigated through Shubnikov-de Haas (SdH) oscillations (Fig.1a). Remarkably, we observed a progressive increase in cyclotron mass and oscillation frequency with the magnetic field (Fig. 1b and c), indicating the presence of non-trivial electronic bands [4]. Besides providing experimental evidence for topological-like electronic states in $KTaO_3$-2DEG, these findings shed light on the recent predictions of topological states in the 2DEG based on similar perovskite transition metal oxides.

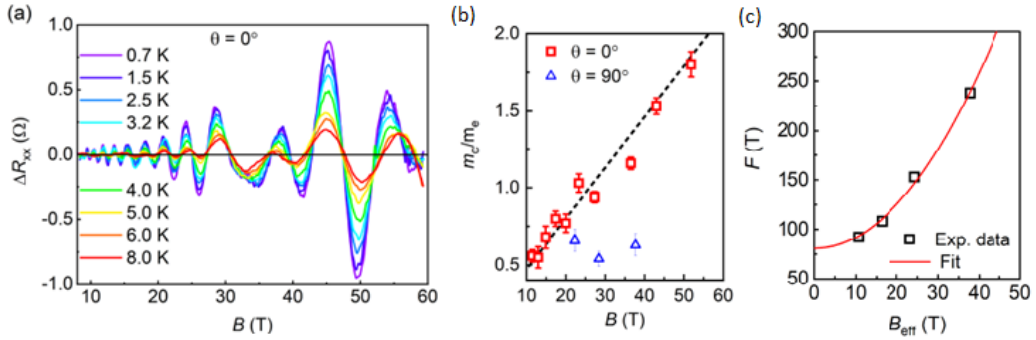

Fig. 1 (a) SdH oscillations in EuO/$KTaO_3$ measured at different temperatures. Magnetic field dependencies of cyclotron mass and oscillations frequency in 1/*B* are displayed in (b) and (c).

[1] K. Rubi *et al*., npj Quantum Materials **5**, 1 (2020); King, P. D. C. *et al*. Phys. Rev. Lett. **108**, 117602 (2012).
[2] K. Rubi *et al*., Phy. Rev. Research **3**, 033234 (2021).
[3] H. Zhang *et al*., Phys. Rev. Lett. **121**, 116803 (2018); Liu *et al*., Science **371**, 716 (2021).
[4] K. Rubi *et al*., arXiv:2307.04854 (2023).

* Author for correspondence: rubi@lanl.gov

Searching for the Excitonic Insulator State in Quantum Materials

E. Baldini[1]

[1] *Department of Physics, The University of Texas at Austin, Austin, TX, USA*

The excitonic insulator is an electronically driven phase of matter that emerges upon the spontaneous formation and Bose condensation of excitons. Detecting this exotic order in candidate materials is a subject of paramount importance, as the size of the excitonic gap in the band structure establishes the potential of this collective state for superfluid energy transport. However, the identification of this phase in real solids is hindered by the coexistence of a structural order parameter with the same symmetry as the excitonic order. Only a few materials are currently believed to host a dominant excitonic phase, Ta_2NiSe_5 being the most promising. In this talk, I will describe how advanced protocols based on time- and angle-resolved photoemission spectroscopy can shed light on primary order parameter of a candidate excitonic insulator [1]. Finally, I will discuss the opportunities offered by the development of novel momentum microscopy tools to extend these studies to the realm of two-dimensional material flakes that may host similar physics.

[1] E. Baldini et al., Proc. Natl. Acad. Sci. 120, e2221688120 (2023)

[+] Author for correspondence: edoardo.baldini@austin.utexas.edu

Comparative study on non-linear and linear least square analyses applied to X-ray induced Auger electron spectroscopy transitions

Anna Gagliardi,[1] N. Fairley,[2] S. Béchu[1]

[1] *Institut Lavoisier de Versailles (ILV), Université de Versailles Saint-Quentin-en-Yvelines, Université Paris-Saclay, CNRS, UMR 8180, 45 avenue des Etats-Unis, 78035 Versailles Cedex, France.*

[2] *Casa Software Ltd, Bay House, 5 Grosvenor Terrace, Teignmouth, Devon TQ14 8NE, United Kingdom.*

With the exception of the modified Auger parameter, X-ray induced Auger electron (X-AES) transitions aren't exploited to their full potential. Indeed, they can provide as much information (oxidation degree, chemical environment, atomic composition) as the classic photopeaks used in XPS, but their shapes' complexities limit their decompositions.

We offer here to explore the decomposition of Ga $L_3M_{4,5}M_{4,5}$ and In $M_{4,5}N_{4,5}N_{4,5}$ X-AES lines by comparing two approaches: the non-linear [1] and the linear [2] least square analyses. By combining non-linear and linear fitting procedures, PCA, and vectorial method [3], those two analyses have been implemented on the materials $Cu(In_xGa_{1-x})Se_2$ and InSb, to unveil their surface oxidation when exposed to different atmospheres. The growth of oxide phases (Ga_2O_3 and In_2O_3, determined by PCA, vectorial method and by comparison with reference spectra) was monitored on the X-AES lines with non-linear and linear approaches, showing a very good coherence between both, as illustrated in Fig 1 for the In $M_{4,5}N_{4,5}N_{4,5}$ X-AES transition of InSb. We will provide keys to perform non-linear and linear least squares analysis on X-AES lines, to explore new approaches for chemical determination.

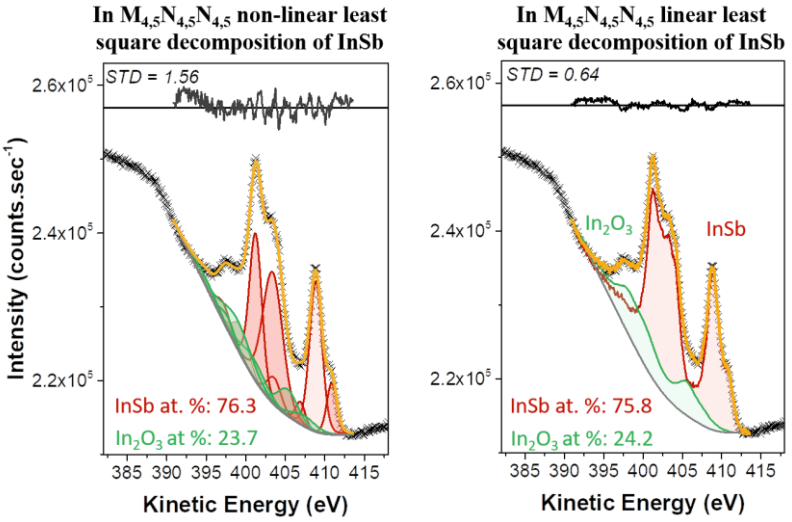

Figure 1 Curves to fitted data of InSb using non-linear (left) and linear (right) approaches.

[1] J.J. Moré, Numer. Anal. **630**, 105 (1978).
[2]G.H. Golub and C. Reinsch, Linear Algebr. **420**, 403 (1971).
[3] S. Béchu et al., Appl. Surf. Sci. **447**, 528 (2018).

+ Author for correspondence: solene.bechu@uvsq.fr

Supplementary Pages (Optional)

In Figure S1, we provide the example of Ga $L_3M_{4,5}M_{4,5}$ non-linear and linear least square approaches for CIGS material after aging. When using the non-linear approach, 5 arbitrary photopeaks are necessary to simulate the CIGS environment and 5 others for the Ga_2O_3 one. The fit results thus in a decomposition with 10 photopeaks while reference spectra of Ga in CIGS and in Ga_2O_3 are injected within the linear least square decomposition. If the fit is easier to perform with the linear least square decomposition (less error), its quality is slightly improved when using the non-linear least square decomposition approach. This aspect will be also evocated.

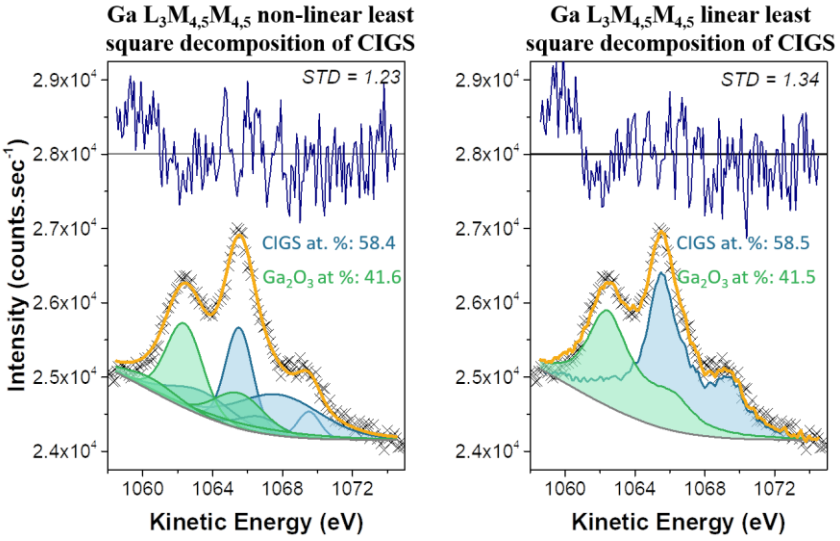

Figure S2 Curves to fitted data of CIGS using non-linear (left) and linear (right) approaches.

To show the coherence of the two approaches over a set of evolving data, we followed the percentage of Ga_2O_3 growth in CIGS Ga $L_3M_{4,5}M_{4,5}$ X-AES transition over time. Table S1 resumes this evolution for the non-linear and the linear approaches and the relative errors remain inferior to 5% for all the comparative data.

		t_0	t_1	t_2	t_3	t_4	t_5	t_6	t_7	t_8
Ga_2O_3 at. %	Non-linear approach	0.1	27.9	35.2	39.6	42.9	41.3	45.4	46.3	53.4
	Linear approach	0.0	27.6	34.3	39.1	42.3	41.1	45.9	45.9	53.1
Relative error (%)		0.0	1.1	2.6	1.3	1.4	0.5	1.1	0.9	0.6

Probing electrons and light in nanomaterials using the photoelectric effect

T. Ohta,[1] A. Boehm,[1] S. D. Gennaro,[1] C. F. Doiron,[1] A. Kim,[1] K. Thürmer,[2] J. D. Sugar,[2] C. D. Spataru,[2] J. J. Fonseca,[3] J. T. Robinson,[3] T. E. Beechem,[4] M. B. Sinclair,[1] I. Brener,[1] R. Sarma[1]

[1] Sandia National Laboratories, Albuquerque, NM 87185
[2] Sandia National Laboratories, Livermore, CA 94550
[3] US Naval Research Laboratory, Washington, DC 20375
[4] Purdue University, West Lafayette, IN 47907

The photoelectric effect is sensitive to both the occupied electronic density of states and the electromagnetic field distribution. Thus, capturing the energy, yield, and spatial origin of photoelectrons from the sample enables us to examine local electronic properties and light-matter interactions concurrently. In this talk, we will describe two case studies using photoelectron emission microscopy (PEEM), revealing the spatial variations of Schottky barrier height between WS_2 and Au, and the local electromagnetic near-field profiles of Si metasurfaces. We will discuss the impact of crystallographic facets of Au grains as well as how the attractive interaction of Au with WS_2 can modify the crystallographic alignment among WS_2 layers. For near-field imaging, we will demonstrate the sensitivity of photoemission yield to the light absorptivity in visible to near infrared range, and evaluate the field profiles around Si meta atoms at the sub-(photon) wavelength scale on and off resonance excitation. Altogether we will discuss the potential of photoelectron imaging to examine the intertwined light-matter coupled phenomena abundant in two-dimensional and quantum materials.

The work was supported by Sandia's LDRD program and in part by the US Department of Energy, Office of Basic Energy Sciences, Division of Materials Sciences and Engineering). The work performed at the U.S. Naval Research Laboratory (NRL) was supported through Base Programs funded by the Office of Naval Research and through the NeuroPipe ARAP funded by the Office of the Secretary of Defense. Samples were fabricated, in part, at the Center for Integrated Nanotechnologies, an Office of Science User Facility operated for the US Department of Energy, Office of Science. Sandia National Laboratories is a multimission laboratory managed and operated by National Technology and Engineering Solutions of Sandia, LLC., a wholly owned subsidiary of Honeywell International, Inc., for the U.S. Department of Energy's National Nuclear Security Administration under contract DE-NA0003525. This paper describes objective technical results and analysis. Any subjective views or opinions that might be expressed in the paper do not necessarily represent the views of the U.S. Department of Energy or the United States Government.

[+] Author for correspondence: tohta@sandia.gov

Layer-by-layer engineering and deciphering of topological orders in magnetic topological insulators

Woojoo Lee,[1] Sebastian Fernandez-Mulligan,[1] Hengxin Tan,[2] Chenhui Yan,[1] Yingdong Guan,[3] Seng Huat Lee,[3,4] Ruobing Mei,[3] Chaoxing Liu,[3] Binghai Yan,[2] Zhiqiang Mao,[3] and Shuolong Yang,[1,+]

[1] Pritzker School of Molecular Engineering, The University of Chicago, Chicago, Illinois 60637, USA

[2] Department of Condensed Matter Physics, Weizmann Institute of Science, Rehovot 7610001, Israel

[3] Department of Physics, Pennsylvania State University, University Park, State College, Pennsylvania 16802, USA

[4] 2D Crystal Consortium, Materials Research Institute, Pennsylvania State University, University Park, State College, Pennsylvania 16802, USA

The advent of intrinsic magnetic topological insulators enables us to envisage various low-dimensional topological orders, such as the quantum anomalous Hall insulators and the axion insulators, at realistic cryogenic temperatures. These materials are represented by $MnBi_2Te_4$ and its derived superlattices $MnBi_{2n}Te_{3n+1}$. However, it has been controversial whether these materials exhibit the key ingredient for magnetic topological phases: an energy gap due to the time-reversal symmetry breaking. Moreover, the construction of high-quality magnetic topological insulators at the ultrathin limit has met significant challenges. In this talk, I will present a new technique, layer-encoded frequency-domain photoemission spectroscopy, which allows us to decipher the layer origins of various electronic states. By encoding layer indices with intralayer phonon frequencies, we measure the strengths of coupling with layer-specific phonons. This experiment reveals that the topological surface states on antiferromagnetic $MnBi_4Te_7$ are partially relocated to the nonmagnetic layers, reconciling the mystery of vanishing broken-symmetry gaps [1]. Moreover, I will present our recent progress on the "carpet-growth" of Bi_2Te_3 ultrathin films and $MnBi_2Te_4/Bi_2Te_3$ heterostructures using molecular beam epitaxy. These thin films extend coherently across a millimeter spatial scale without disruptions by substrate step edges. Angle-resolved photoemission spectroscopy studies yield unprecedentedly sharp electronic structures in agreement with first-principles calculations layer-by-layer, and suggest opportunities to realize the quantum spin Hall effect and quantum anomalous Hall effect at near-ambient temperatures [2].

[1] W. Lee *et al.*, Nature Physics **19**, 950-955 (2023).
[2] W. Lee *et al.,* Submitted (2023).

[+] Author for correspondence: yangsl@uchicago.edu

Supplementary Page 1

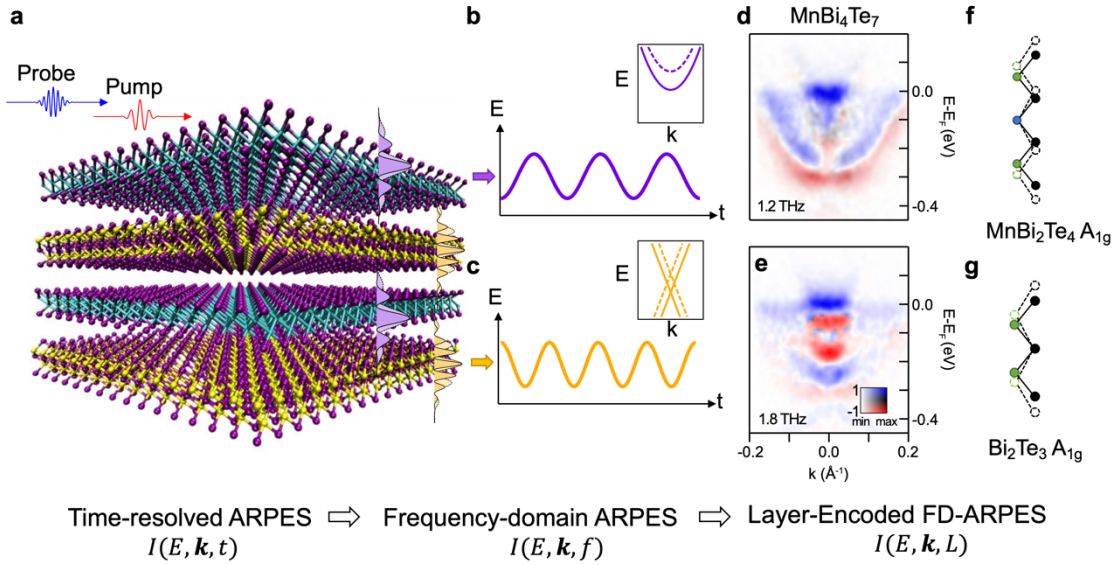

Figure 1. Resolving the layer origins of electronic states in $MnBi_4Te_7$ using layer-encoded, frequency-domain ARPES. (a) Schematic of pump-probe setup on a superlattice material. (b,c) Different electronic states are coupled to layer-specific coherent phonon oscillations. (d,e) Frequency-domain (FD) ARPES allows us to resolve the electronic states coupled to the $MnBi_2Te_4$ A_{1g} mode and the Bi_2Te_3 A_{1g} mode, respectively. The layer-frequency correspondence leads to layer-encoded FD-ARPES. The mode configurations are shown in panels (f) and (g).

Mechanisms and applications for remote epitaxy of Heusler compounds

J. K. Kawasaki,[1]
[1] *University of Wisconsin - Madison, 1509 University Ave, Madison, WI 53706*

Remote epitaxy on monolayer graphene is promising for synthesis of highly lattice mismatched materials, exfoliation of free-standing membranes, and re-use of expensive substrates. However, due to contaminants at the transferred graphene/substrate interface, other mechanisms such as pinhole-seeded lateral epitaxy often dominate rather than the intrinsic growth via remote interactions [1]. I will describe our understanding of the synthesis science of remote epitaxy, focusing on III-V semiconductors and Heusler compounds [1,2]. I will also show how exfoliated free-standing membranes of rare earth Heusler compounds can be used to tune (flexo)magnetism and novel superconductivity [3,4].

[1] S. Manzo, et. al., Nature Commun., 13, 4014 (2022).
[2] D. Du et. al., Nano Lett. 22, 21, 8647 (2022).
[3] D. Du, et. al., Nature Commun., 12, 2494 (2021).
[4] D. Du, e. al. APL, 122, 170501 (2023).

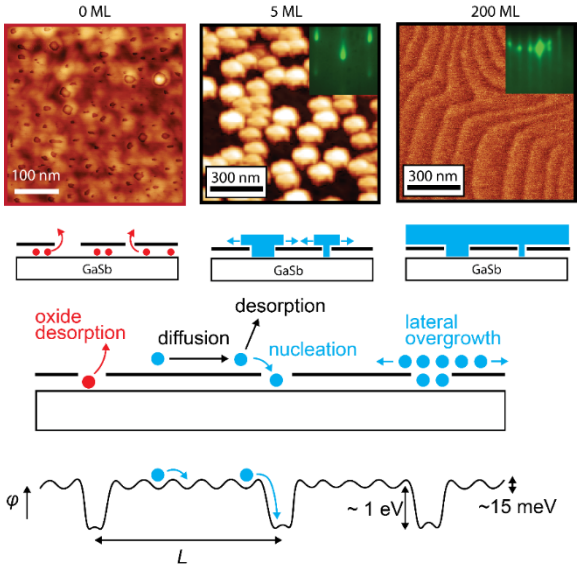

Figure 1. Pinhole seeded lateral epitaxy. S Manzo, et. al., Nature Commun 2022.

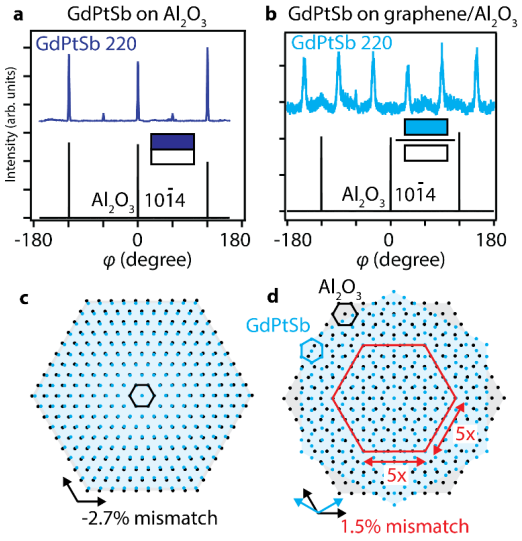

Figure 2. Epitaxial rotation of GdPtSb on graphene/sapphire. D Du, et. al., Nano Lett 2022.

[+] Author for correspondence: jkawasaki@wisc.edu

High-mobility two-dimensional electron gas with quantized states in polar-discontinuity doped $LaInO_3/BaSnO_3$ heterostructure grown by molecular beam epitaxy

G. Hoffmann,[1] A. Hartl,[2] M. Zupancic,[3] A.A. Riaz,[4] V.N. Strocov,[2] M. Albrecht,[3] A. Regoutz,[4] O. Bierwagen[1]

[1] *Paul-Drude-Institut für Festkörperelektronik, Leibniz-Institut im Forschungsverbund Berlin e.V., Hausvogteiplatz 5—7, 10117 Berlin, Germany*

[2] *Swiss Light Source, Paul Scherrer Institute, CH-5232 Villigen-PSI, Switzerland*

[3] *Leibniz-Institut für Kristallzüchtung, Max-Born-Straße 2, 12489 Berlin, Germany*

[4] *University College London, 20 Gordon Street, London WC1H 0AJ, UK*

Transistor applications of semiconducting oxides require, both high room-temperature electron mobilities (μ_{RT}) and high charge carrier densities (CCDs), ideally realized with a two-dimensional electron gas (2DEG). So far, prototype oxide 2DEG systems have either high μ_{RT} but limited CCD such as modulation-doped $(Al_xGa_{1-x})_2O_3/Ga_2O_3$, or a high CCD but low μ_{RT} such as the polar-discontinuity doped $LaAlO_3/SrTiO_3$ interface. Interfacing the more suitable, wide-bandgap, nonpolar semiconductor $BaSnO_3$ (BSO), having high bulk μ_{RT} (up to 320 cm^2/Vs), with polar $LaInO_3$ (LIO) is predicted to create and confine a 2DEG with CCD up to $2x10^{14}$ cm^{-2} for the SnO_2/LaO interface termination.

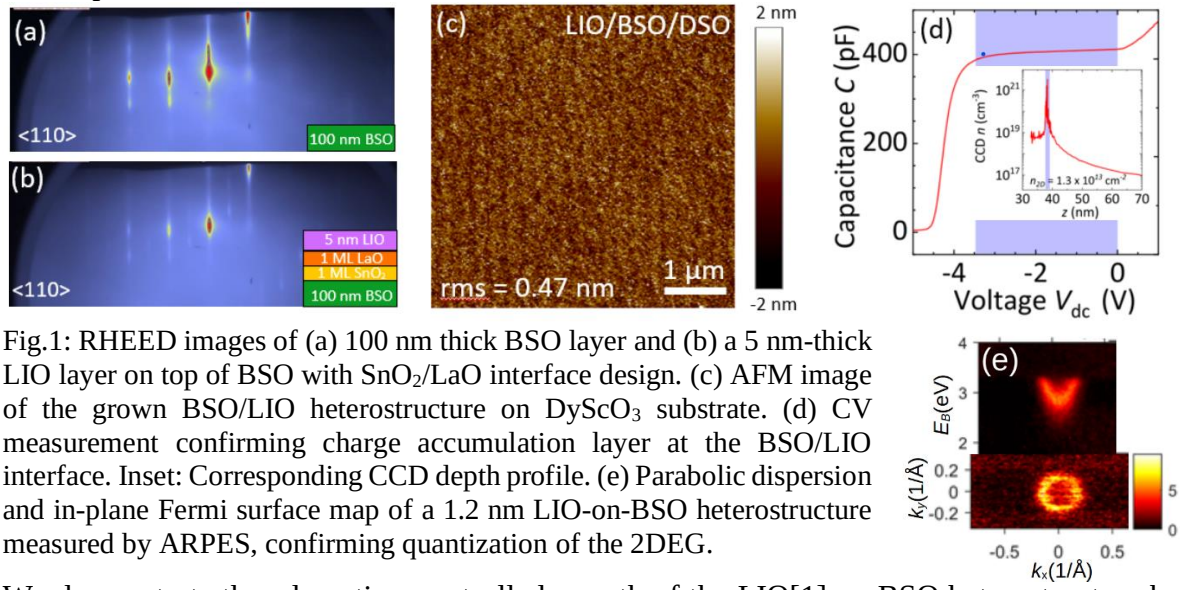

Fig.1: RHEED images of (a) 100 nm thick BSO layer and (b) a 5 nm-thick LIO layer on top of BSO with SnO_2/LaO interface design. (c) AFM image of the grown BSO/LIO heterostructure on $DyScO_3$ substrate. (d) CV measurement confirming charge accumulation layer at the BSO/LIO interface. Inset: Corresponding CCD depth profile. (e) Parabolic dispersion and in-plane Fermi surface map of a 1.2 nm LIO-on-BSO heterostructure measured by ARPES, confirming quantization of the 2DEG.

We demonstrate the adsorption-controlled growth of the LIO[1] on BSO heterostructure by molecular beam epitaxy using a shutter sequence to control the SnO_2/LaO interface termination. The films were analyzed by reflection high-energy electron diffraction (RHEED) [Figs. 1(a) and 1(b)], x-ray diffraction, atomic force microscopy (AFM) [Fig. 1(c)]. The interface structure is investigated by cross-sectional transmission-electron microscopy. The formation of the quantized 2DEG at their interface is confirmed by capacitance-voltage (CV) [Fig. 1(d)] and angular-resolved photo-electron spectroscopy (ARPES) [Fig. 1(e)]. Van der Pauw-Hall measurements confirm CCD>$10^{13}cm^{-2}$ and μ_{RT}>$100cm^2/Vs$.

[1] G. Hoffmann et al., Phys. Rev. Mater. **7**, 084606 (2023).

+ Author for correspondence: bierwagen@pdi-berlin.de

Enabling direct write fabrication of low dimensional micro- and nanostructures on supported and suspended substrates

I.Kuljanishvili[1], Y. Kim[1], N. Schaper[1], K. McCormack[1], R. Divan[2], D.J. Gosztola[2]
[1] Department of Physics, Saint Louis University, St. Louis, MO 63103, USA
[2] Center for Nanoscale Materials, Argonne National Laboratory, 9700 S. Cass Avenue, Lemont, IL 60439, USA

Low-dimensional nanomaterials, such as one-dimensional (1D) or two-dimensional (2D) systems, assembled in vertical or lateral arrangements, often lead to enhanced properties and new functionalities. Nanotubes, nanowires (NWs), and 2D layered structures (graphene and graphene like materials) are emerging as key building blocks for the next generation devices and emerging technologies. Practical implementation of such nanomaterials necessitates their successful incorporation with well-established processes for fabricating electronic and/or mechanical devices. While preparing layered architectures usually involves multi-step fabrication processes but relies on mask-assisted fabrication techniques. Here, we present a methodology for the controlled and selective preparation of nanostructures such as 1D NWs on 2D materials-substrates in various controlled geometric assemblies by employing direct write patterning (DWP) of custom ink precursors on supported or suspended architectures for subsequent chemical vapor deposition (CVD) synthesis. Our two-step fabrication approach enables simple and flexible routes to produce various architectures in a precisely controlled fashion. Location-specific materials synthesis provides access to as-grown interfaces and rapid testing of materials' quality, crystallinity, chemical composition, etc.

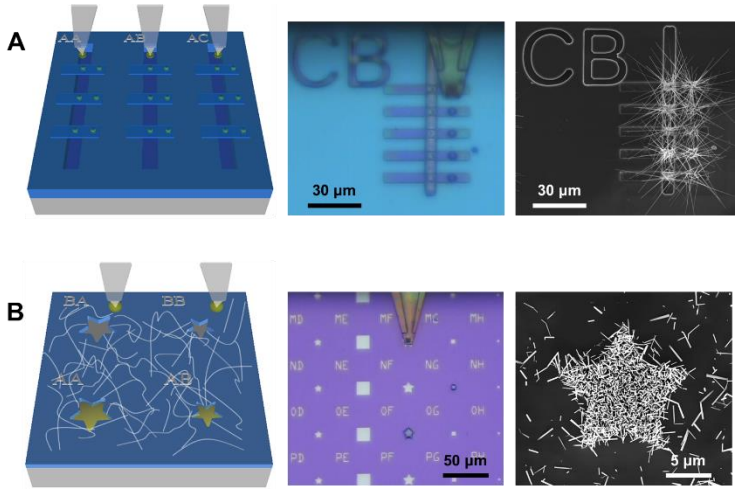

Figure1. Direct-write fabrication and synthesis of the nanostructures (**A)** Selective growth of ZnO NWs assemblies on suspended architectures via DWP approach and CVD synthesis. **(B)** 1D-2D interface formation using DWP and CVD synthesis.

[1] McCormack, K. et al. *Mater. Today Nano* **20**, 100241 (2022).
[2] Schaper, N. et al. *Nanomaterials* **11**, 1836 (2021).

[+] Author for correspondence: irma.kuljanishvili@slu.edu

Silicon (111) - Aluminum (111) - Amorphous Alumina: Asymmetric Quantum Well and Band Alignment

H. Jin[1] and Alexander A. Demkov[1]
[1]*Department of Physics, The University of Texas at Austin, Austin, Texas 78712, USA.*

Thin single crystal films of Al can be epitaxially grown on Si(111) [1]. When taken out of ultra-high vacuum, Al oxidizes and forms a quantum well structure Si-Al-Al_2O_3. Theoretical calculations can shed light on finding the band alignment across the hetero-structure and its electronic and optical properties. However, one needs to build a structural model. The structure of Al on Si(111) has been experimentally determined via the electron microscopy by McSkimming et al. [1]. The Al layer is found to be (111) oriented, with a linear ratio of 3 Si to 4 Al atoms along the interface. Using this information, we construct a periodic model of Si-Al interface and perform density functional theory (DFT) calculations to find the relaxed structure, layer-projected density of states, and planar averaged potential across the interface. From there, we find the band alignment using the valence band offset from the bulk averaged potential. When aluminum metal is exposed to air, a several nanometers thick layer of alumina rapidly forms [2]. This oxide layer is amorphous. We simulate the structure of amorphous alumina using ab-initio molecular dynamics with the melt-and-quench technique [3]. This amorphous alumina can then be directly combined with the previous system to form an asymmetrical quantum well, where the well states and band alignment can be directly obtained from the DFT calculations.

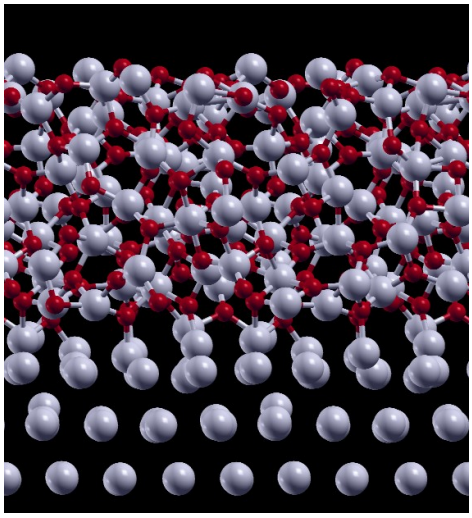

Figure 1. Al-Al_2O_3 interface structure. Red: O; Grey: Al

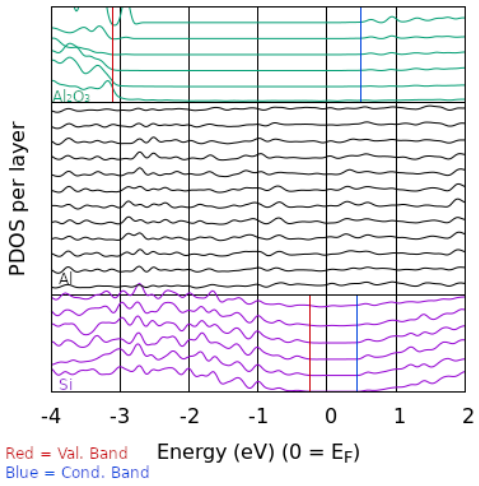

Figure 2. Layer projected DOS of Si-Al-Al_2O_3 asymmetric quantum well.

[1] McSkimming, B. M., Alexander, A., Samuels, M. H., Arey, B., Arslan, I., & Richardson, C. J. (2016). Metamorphic growth of relaxed single crystalline aluminum on silicon (111). J. Vac. Sci. & Technol. A **35**, 021401 (2017).

[2] Jeurgens, L. P., Sloof, W. G., Tichelaar, F. D., & Mittemeijer, E. J. Growth Kinetics and mechanisms of aluminum-oxide films formed by thermal oxidation of aluminum. Journal of Applied Physics, **92**, 1649 (2002).

[3] Gutiérrez, G., asnd Johansson, B. Molecular dynamics study of structural properties of amorphous Al_2O_3. Physical Review B **65**, 104202(2002).

Silicene Ribbons: Synthesis, Electronic and Geometric Structure at the Atomic Scale

A. Costine [1], Z. Gai [2], and P. Reinke [1] #

[1] *Department of Materials Science and Engineering, University of Virginia, 385 McCormick Road, Charlottesville, VA 22904*

[2] *Center for Nanophase Materials Sciences, Oak Ridge National Laboratory, Oak Ridge, TN 37831*

[#] Author for correspondence: Petra Reinke pr6e@virginia.edu

Silicene is a 2D material which poses significant challenges in synthesis and device integration but offers unique electronic properties which are not yet fully understood. Challenges remain in silicene synthesis on non-metallic substrates and the control of buckling. The degree of in-plane buckling is tied to the emergence of a Dirac point and intriguing quantum phases have been predicted. [1-4] In our previous work we discovered a new pathway to silicene synthesis using h-$MoSi_2$ (0001) surfaces as templates, [5] and we present here the formation of silicene nanoribbons on the same surface, and measure their geometric and electronic structure with STM and STS at 77 K. Our work promises a new pathway to create silicene layers and nanoribbons with molecular beam epitaxy directly on silicon wafers.

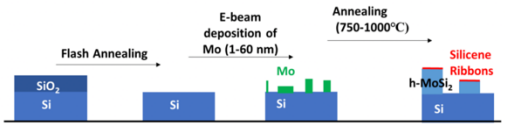

Figure 1: Schematics of synthesis method used for silicene nano-ribbons.

The h-$MoSi_2$ (0001) crystallites are synthesized on Si(100) by deposition of a thin Mo film with electron beam evaporation, and subsequent annealing to form well-defined crystallites with 15 - 120 nm in diameter. Nanoribbons cover the entire surface for all "flat top" silicide crystallites with (0001) surfaces. Several surface reconstructions present intermediate superstructures, and are precursors for the nanoribbons. The STM images in Fig. 2 illustrate the geometric structure of the nanoribbons which are 1.8 nm in width and separated by a distinct groove of roughly a single atomic row in width. Models of the nanoribbon's geometric structure will be discussed. The atoms located at the ribbon edge appear brighter which is likely due to density of states (DOS) modulation by edge states. Characteristic defects are seen in the ribbons and express identical STM. The average DOS (dI/dV) measured with STS is indicative of a Dirac type electronic signature with a V-type dip around E_F, and the position dependent DOS across the ribbons allows to identify the Dirac type regions. We will discuss all aspects of electronic and geometric structure of the nanoribbons including electronic confinement, and localized Dirac type signatures. In addition, point defects, and long range deformations induced by strain are addressed and inform our structural models.

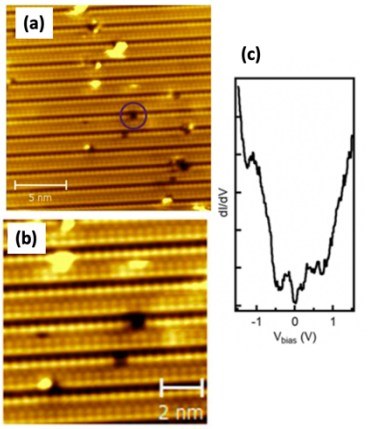

Figure 2: Ribbon-silicene on h-$MoSi_2$ crystallites (a) 20×20 nm empty state image (V_B = +1.5 V), (b) 10×10 nm zoom-in of the empty state image (V_B = +1.5 V), All images are at I_t = 0.1 nA. (c) average STS spectra across a ribbon.

[1] C. Grazianetti et al.. ACS Nano **11**, 3376-3382 (2017). [2] C.-C. Liu et al.. Physical Review Letters **107**, 076802 (2011). [3] A. Molle et al. Chemical Society Reviews **47**, 6370-6387 (2018). [4] H. J. W. Zandvliet. Nano Today **9**, 691-694 (2014). [5] C. Volders et al. Nano Letters **17**, 299-307 (2017).

Spontaneous growth of silver on Si(001) tuned by substrate temperature

Xiaohang Huang,[1] and Kai Huang[1]
[1] *Chemistry Program, Guangdong Technion-Israel Institute of Technology, No. 241, Daxue Road, Shantou, Guangdong Province, China, 515063.*

The development of semiconductor technology features miniaturization of device that approaches the physical limit, i. e., nanostructure of a few atoms and/or molecules. It has been aimed that one could use nanostructures to fabricate functional devices at will. For the system of silver on Si(001), there is a rich collection of nanostructures as revealed in our recent works [1, 2], serving as the candidates to test this aim.

In this work, we examined the spontaneous growth of silver on Si(001) held at 109 to 298 K by scanning tunneling microscopy. As shown in Figure 1, the dimension of the formed silver depends on the substrate temperature during the deposition. That is, silver is formed predominantly as zero-dimensional (0D) objects at less than 120 K, one-dimensional (1D) objects at 120-200 K, and two-dimensional (2D) objects at 200-270 K. These observations are linked to the anisotropic migration of the key intermediate of silver tetramer, as supported by density functional simulations; the barriers are calculated as 0.24 eV along Si-rows, and 0.68 eV across Si-rows [2]. A schematic of the growth dynamics is sketched in Figure 2.

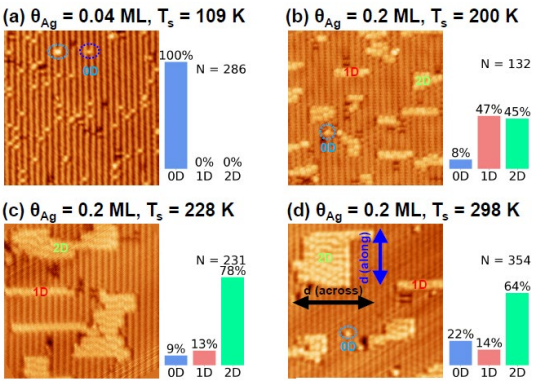

Figure 1. (a)-(d) STM images of Ag deposited on Si(001) held at 109, 200, 228 and 298 K.

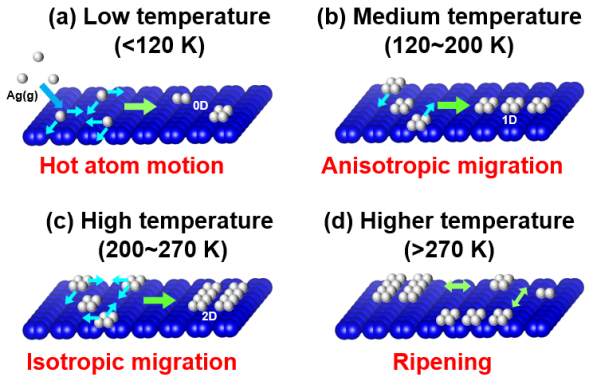

Figure 2. Interpretation of spontaneous formation of silver structures on Si(001) at (a) low (b) medium (c) high and (d) higher temperatures.

[1] K. Huang, X. Huang, J. Nogami, Phys. Chem. Chem. Phys. **7**, 23 (2021).
[2] X. Huang, A. Hoffman, K. Huang, J. Phys. Chem. C. **18**, 126 (2022)

+ Author for correspondence: kai.huang@gtiit.edu.cn

Interplay of valley polarized dark trion and dark exciton-polaron in monolayer WSe_2

X. Cong[1], P. Ali Mohammadi[1], M. Zheng[1], K. Watanabe[2], T. Taniguchi[3], D. Rhodes[4], X.-X. Zhang [1]

[1] Department of Physics, University of Florida, Gainesville, Florida, USA
[2] Research Center for Functional Materials, National Institute for Materials Science, Japan
[3] International Center for Materials Nanoarchitectonics, National Institute for Materials Japan
[4]Department of Materials Science and Engineering, University of Wisconsin Madison, Madison, Wisconsin, USA

The interactions between charges and excitons involve complex many-body interactions at high densities. The exciton-polaron model has been adopted to understand the Fermi sea screening of charged excitons in monolayer transition metal dichalcogenides (TMD). The results provide good agreement with absorption measurements, which are dominated by dilute bright exciton responses. The Fermi-polaron model treats the quasiparticle responses of a single mobile impurity in a surrounding Fermi sea. In comparison, the exciton density in monolayer TMD can be tuned by laser fluence and be comparable to or exceed the charge density, where the analogy to a single mobile impurity no longer applies. The modification to Fermi sea screening at high exciton densities, however, is still not well understood. Apart from the bright excitons previously studied in reflection contrast measurements, different spin and momentum dark exciton species have been established, which are also expected to have many-body interactions with charges. The coupling between these different species of exciton-polarons has not yet been experimentally investigated.

Here we investigate the Fermi sea dressing of spin-forbidden dark excitons in monolayer WSe_2 [1]. With a Zeeman field, the valley-polarized dark excitons show distinct p-doping dependence in photoluminescence when the carriers reach a critical density (see Fig. 1). This density can be interpreted as the onset of strongly modified Fermi sea interactions and shifts with increasing exciton density. Through valley-selective excitation and dynamics measurements, we also infer an intervalley coupling between the dark trions and exciton-polarons mediated by the many-body interactions. Our results reveal the evolution of Fermi sea screening with increasing exciton density and the impacts of polaron-polaron interactions, which lay the foundation for understanding electronic correlations and many-body interactions in 2D systems.

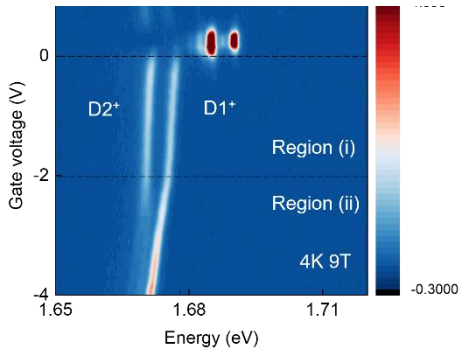

Figure 1. Dark exciton emission from a monolayer WSe_2 device at 4K, 9T out-of-plane magnetic field. D1+ and D2+ and the Zeeman-split dark trions. The dashed line at ~ -2V marks the crossover between region (i) and region (ii), which is also assigned to be the dark trion to dark exciton-polaron crossover for D1+. At the crossover, D2+ broadens and quenches in amplitude.

[1] Cong, Xin, et al. "Interplay of valley polarized dark trion and dark exciton-polaron in monolayer WSe2." arXiv preprint arXiv:2308.04974 (2023).

[+] Author for correspondence: xxzhang@ufl.edu

Evidence of Single Photon Emitters from 1L WSe_2 under Electrostatically Induced Strain

F.C.M. Wu,[1,2] S.-H. Wu,[1] B. Fang,[2] X. Li, [1,2] J.A. Incorvia, [1,2] and E.T. Yu[1,2]
[1] Department of Electrical and Computer Engineering, The University of Texas at Austin, TX, USA
[2] Center for Dynamics and Control of Materials, The University of Texas at Austin, TX, USA

Strain engineering is a powerful tool that strongly influences electronic structure and exciton states in 2D transition metal dichalcogenides (2D TMDs). Among 2D TMDs, monolayer WSe_2 has gained attention as a host for quantum emitters due to its lowest lying dark exciton state that hybridizes with mid-gap defect states under tensile strain, giving rise to bright single photon emitters. The creation of a hybridized state consisting of dark excitons and mid-gap defect states results in the radiative recombination of dark excitons that is otherwise forbidden due to spin and momentum conservation. At cryogenic temperatures, the energetic alignment and coupling of the two abovementioned states results in localized defect emission which possess significant characteristics of single photon emitters. Strain-tunable devices are crucial for investigating the nature of TMD-based single photon emitters which can be beneficial for quantum information processing and secure communications.

In this study, we demonstrate strain modulation of monolayer WSe_2 suspended over a hole-patterned substrate via electrostatic deflection and characterize the resulting photoluminescence. This approach enables the creation of strain-tunable WSe_2 devices that can be operated at cryogenic temperatures, wherein strain fields are generated by applying a bias voltage to the suspended monolayer WSe_2 membrane. We observe a significant monolayer deflection of ~50 nm at 15V gate bias and a ~20 meV redshift of dark exciton peak as the applied is increased to 20V, corresponding to a 0.2% increase in tensile strain of WSe_2. Sharp localized emitters, typically associated with single photon emitters, were observed at 4K which showed less dependence on strain as the applied bias increased. Thus, we attribute these localized emitters to the presence of localized defects which are only weakly influenced by strained lattice environment. We also observe luminescence lifetimes of ~3ns and saturation of luminescence intensity with incident power, both of which are also characteristic of single photon emitters. These realizations are critical for understanding the origin of single photon emitters based on strained monolayer WSe_2.

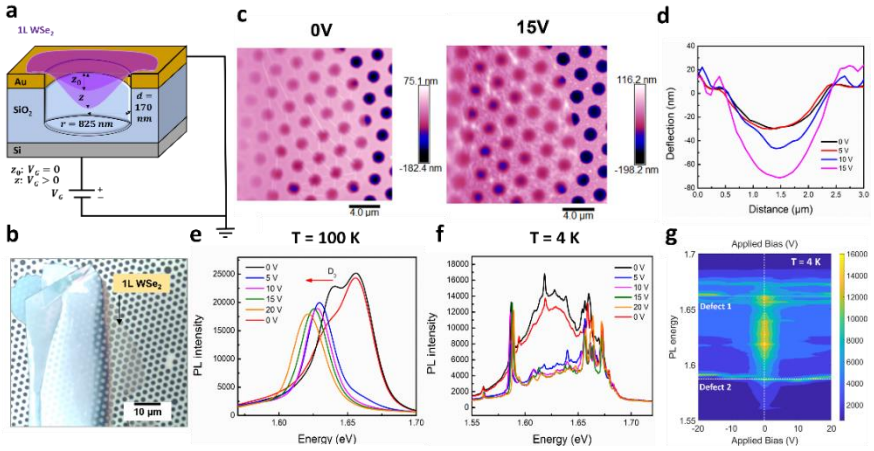

***Figure 1 a**. Schematic diagram of electrostatic straining approach. **b.** Optical image of 1L WSe_2 on hole-patterned substrate. **c.** AFM height images at different applied bias, showing a significant monolayer deflection as the applied bias is increased **(d).** Photoluminescence spectra measured at T = 298 K showing a redshift of dark exciton peak as a function of applied bias **(e)** and at T = 4 K showing the presence of sharp localized emitters **(f)** which are located at energies corresponding to defect level states **(g)**.*

Supplementary Pages

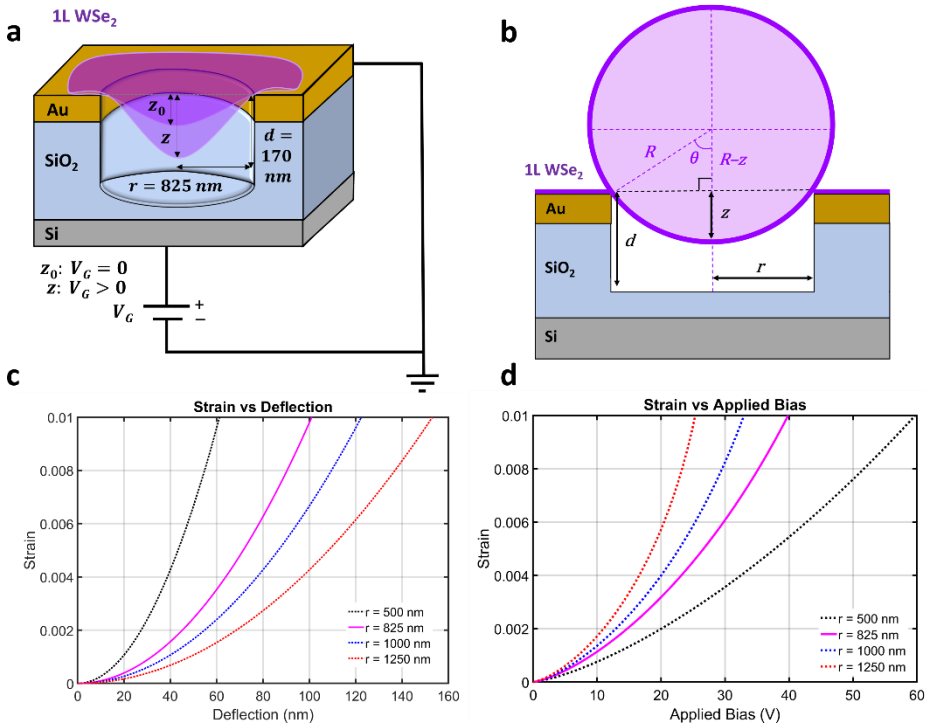

Figure 2 *Strain calculations from electrostatic-induced deflection of suspended monolayer WSe_2. Schematic diagrams of a suspended WSe_2 monolayer over patterned-hole substrate and straining approach (**a**) and a circumferential strain model* of suspended WSe_2 monolayer (**b**). Calculated strain as a function of monolayer deflection (**c**) and strain as a function of applied bias (**d**) assuming a semi-spherical monolayer deflection geometry**.**

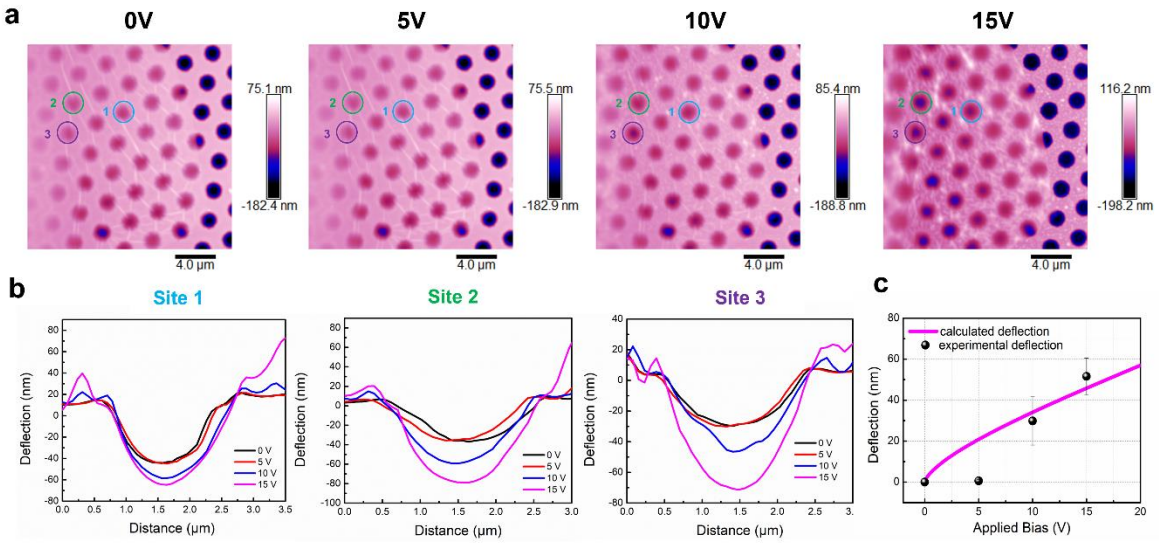

Figure 3 Electrostatic deflection of suspended WSe_2 monolayer at room temperature (T = 100 K). AFM height images taken using tapping mode at different applied biases: 0V, 5V, 10V, and 15V, showing monolayer deflection at increasing applied bias (**a**). Height profiles of monolayer WSe_2 at three different hole sites (b). Comparison between calculated (pink curve) and experimental (black sphere) deflection, showing that the monolayer starts deflecting in between 5V and 10V (c).

Comprehensive Study of Interface Chemistry and Electrical Property of Metal Contacts on TMDs

S. Y. Kim,[1] J. Roy,[1] X. Wang,[1] R. M. Wallace[1]
[1]*Materials Science and Engineering, University of Texas at Dallas, Richardson, TX, USA*

Transition metal dichalcogenides (TMDs) have been introduced due to their exceptional electronic, optical mechanical, and magnetic properties, even in atomically thin thickness, for advanced electronic, optoelectronic, and spintronic devices [1]. However, the limitations in tuning the Schottky barrier height with metal contacts, based on work function greatly hinder efficient carrier injection and electronic performance of TMD-based devices [2]. This study examines contact interfaces and their relationship to electrical contact characteristics. The research encompasses interface chemistry, band alignment, and electronic contact properties of Ni, Ag, Bi, Co and Sn.

An ultrahigh vacuum (UHV) cluster system was employed to investigate the contact properties where in-situ X-ray Photoelectron Spectroscopy (XPS) showed the contact bonding features of metal/TMD interfaces. Ni and Co contacts exhibited stronger bonds with TMD surfaces, resembling covalent-like interfaces, with notable interface reaction products resulting from annealing. However, Bi and Sn showed no robust chemical bonding features under the XPS analysis and van der Waals contact interface was formed due to a weak interaction between metal and TMD. The subsequent ex-situ atomic force microscopy (AFM) measurement supported these contact interface properties. The subsequent electrical characterization using XPS and scanning tunneling microscopy (STM) suggests that the roles of surface defect impact the metal contacts as well. In conclusion, comprehensive research and investigation of metal materials and their contact interface properties with TMDs have shed light on the potential and advantages of metal contact studies.

v; van der Waals bonding interface **n; n-type friendly** **☑; Investigated**
c; covalent bonding interface **p; p-type friendly**

	MoS_2			$MoSe_2$			$MoTe_2$			WS_2			WSe_2			WTe_2		
Ag	☑	v	n	☑	v	n	☑	v	n	☑	v	n	☑	v	n	☑	v	
Ni	☑	c		☑	c		☑	c		☑	c		☑	c	p	☑	c	
Bi	☑	v	n	☑	v	n	☑	v	n	☑	v	n	☑	v	n			
Co	☑	c	p							☑	c	p	☑	c	p			
Sn	☑	v	n	☑	v	n				☑	v	n	☑	v	n			

Table 1. Summary of contact interface investigations.

This work was supported in part by NEWLIMITS, a center in nCORE, a Semiconductor Research Corporation (SRC) program sponsored by NIST through award number 70NANB17H041, and by the National Science Foundation through award DMR-2002741. RMW also acknowledges the support of the Erik Jonsson Distinguished Chair in this work.

[1] Pi, L., Li, L., Liu, K., Zhang, Q., Li, H., and Zhai, T, Adv. Funct. Mater., **29**(51), 1904932 (2019).
[2] Guo, Y., Liu, D., and Robertson, J, ACS Appl. Mater. Interface. **7**, 25709-25715 (2015).

Author for correspondence: rmwallace@utdallas.edu

Transport Anisotropy in One-dimensional Graphene Superlattice in the High Kronig-Penney Potential Limit

Tianlin Li,[1] Hanying Chen,[1] Kun Wang,[1] Yifei Hao,[1] Le Zhang,[1] Kenji Watanabe,[2] Takashi Taniguchi,[3] Xia Hong[1]†

[1] *Department of Physics and Astronomy University of Nebraska, Lincoln, Nebraska, USA*
[2] *Research Center for Electronic and Optical Materials, National Institute for Materials Science, 1-1 Namiki, Tsukuba 305-0044, Japan*
[3] *Research Center for Materials Nanoarchitectonics, National Institute for Materials Science, 1-1 Namiki, Tsukuba 305-0044, Japan*

One-dimensional (1D) graphene superlattice (GSL) has drawn considerable research interest as it is promising for realizing the electron lensing effect [1]. Despite the intensive theoretical studies, 1D GSL has only been realized experimentally via periodic dielectric gates in previous studies [2, 3], which yields a moderate Kronig-Penney (KP) potential profile that is not viable to achieve electron supercollimation.

In this work, we demonstrate 1D GSL in the high KP potential limit exploiting nanoscale domains patterning in a ferroelectric bottom gate [4]. We work with 50 nm (001) $PbZr_{0.2}Ti_{0.8}O_3$ (PZT) films deposited on 10 nm $La_{0.67}Sr_{0.33}MnO_3$ buffered $SrTiO_3$ substrates. Monolayer graphene field-effect transistors with top h-BN global gates are fabricated on PZT prepatterned with periodic polarization up (P_{up}) and down (P_{down}) stripe domains, with the period L varying from 200 to 300 nm (Fig. 1a). The polarization shifts the Fermi level of graphene, leading to a KP potential V_0 of about 0.9 eV at 2 K. We fabricate 1D GSL samples in two configurations, with current along the SL vector $\hat{s}$ and perpendicular to $\hat{s}$. For the former samples, additional Dirac points (DP) emerge in the sheet resistance (R_{xx}) *vs.* top-gated induced electron doping δn (Fig. 1b), from which emanates multiple Landau fan branches in the magnetic field (Fig. 1c). This feature is absent in the latter configuration (R_{yy}), which can be attributed to the SL modulated band crossings along $\hat{s}$. The carrier density between consecutive DP positions (Δn_{DP}) scales with the SL period as $\Delta n_{DP} \propto L^{\beta}$, with $\beta = -1.18 \pm 0.06$ (Fig. 1d), which closely resembles the inversely proportional relation predicted for the high KP potential limit. Figure 1e shows the simulated 1D GSL band structure for our ferroelectric doping scheme, with dimensionless KP potential $u = \frac{V_0 L}{\hbar v_F} = 90\pi$, which reveals a highly flattened band that can potentially host electron lensing effect.

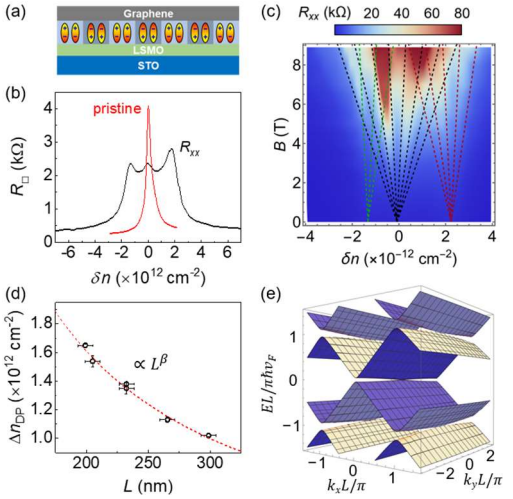

Figure 1. (a) Schematic of 1D GSL. (b) $R_{xx}(\delta n)$ of a 1D GSL at 2 K with L = 205 nm. (c) R_{xx} *vs.* n and B for a 1D GSL, with the modeled Landau fans (dashed lines). (d) $\Delta n_{DP}(L)$ for six 1D GSL samples with a fit. (e) Simulated energy band for $u = 90\pi$.

[1] C. H. Park, et al., Nano Letters **8**, 2920 (2008)
[2] S. Dubey, et al., Nano Letters **13**, 3990 (2013)
[3] Y. Li, et al., Nature Nanotechnology **16**, 525 (2021)
[4] T. Li, et al., arXiv: 2309.04931 (2023)

† Author for correspondence: xia.hong@unl.edu

Supplementary Information

1. Periodic Stripe Domains Writing and Device Fabrication

We define Cr/Au electrodes in the four-point measurement configuration on the PZT films and pattern 100 nm wide P_{down} stripe domains spaced by 100-200 nm in a uniformly polarized P_{up} background between the two voltage probes. Figure S1a shows the piezoresponse force microscopy (PFM) image of a stripe domain region with L = 205 nm. The h-BN/graphene stacks are then transferred onto the SL regions (Fig. S1b) followed by Cr/Au deposition on h-BN as the global top-gate electrode.

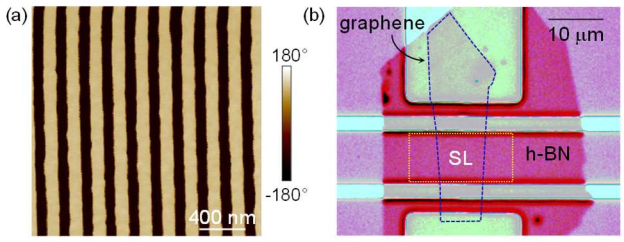

FIG. S1 (a) PFM phase image of strip domains on PZT with L = 205 nm. (b) Optical image of h-BN/graphene transferred on prepatterned domain structure of PZT. The dashed (dotted) lines highlight the boundary of graphene (SL region).

2. Magnetotransport with Current Perpendicular to SL Vector

For 1D GSL with current perpendicular to SL vector $\hat{s}$, the sheet resistance (R_{yy}) exhibits a single peak as a function of top-gate doping (Fig. S2a) with one set of Landau fan branch evolving at high magnetic field (Fig. S2b). This resembles that of pristine graphene, which can be attributed to the suppressed Klein tunneling along the stripe domains and the absence of band crossing perpendicular to the SL vector direction.

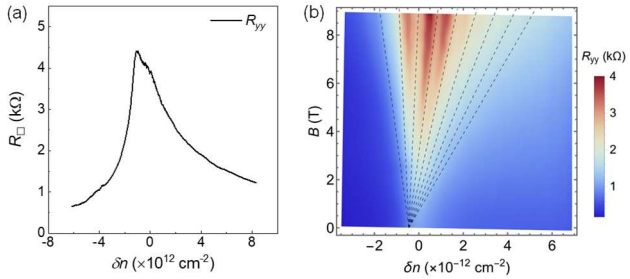

FIG. S2. (a) $R_{yy}(\delta n)$ for a 1D GSL with L = 199 nm, and (b) R_{yy} *vs.* n and B with the modeled Landau fan (dashed lines).

3. Band Flattening at High KP Potential

Figure S3 shows the simulated energy contour plot of the conduction band of 1D GSL with dimensionless KP potential $u = 90\pi$, corresponding to the band structure shown in Fig. 1e. The isopotential contours resemble rectangles, revealing a highly flattened dispersion along k_y, with a Fermi velocity v_y quenched to about 1% of that for pristine graphene.

Terahertz Emission Spectroscopy Revealing Nanoscale Vectorial Photocurrents in Symmetry-Broken Optoelectronic Metasurfaces

J. Pettine,[1] P. Padmanabhan,[1] L. Gingras,[2] R. Holzwarth,[2] R. P. Prasankumar,[1] A. J. Taylor,[1] S.-Z. Lin,[1] and H.-T. Chen[1]

[1] *MPA-CINT, Los Alamos National Laboratory, Los Alamos, NM, USA*
[2] *Menlo Systems, Martinsried, Bavaria, Germany*

Terahertz (THz) emission spectroscopy has emerged in the past several decades as a versatile method for directly tracking the ultrafast evolution of physical properties, quasiparticle distributions, and order parameters within bulk materials and nanoscale interfaces. Ultrafast optically-induced THz radiation is widely utilized to analyze nonlinear polarization, magnetization, and various transient free charge currents, where the underlying broken symmetries (surface and bulk) enable THz emission by defining a system directionality in space and/or time [1]. The broken spatial or temporal symmetries responsible for second-order nonlinearities and bias-free photocurrent generation in materials are typically either intrinsic to the lattice and thus constrained to specific light–matter interaction geometries, or otherwise dependent upon applied static fields that are difficult to texture on small length scales.

In this talk we show that asymmetric gold nanoantennas on graphene exhibit strong light-driven directional responses [2]. The local photocurrent directionality is determined by the orientation of individual nanoantennas, which can be patterned into an arbitrary direction profile for global spatially-varying and optically-controlled photocurrents. We use THz emission spectroscopy, complementary to the direct photocurrent readout, to validate such a concept. Our experimental results clearly demonstrate that these vectorial optoelectronic metasurfaces serve as efficient and versatile sources of ultrafast THz radiation, including broadband THz vector beams. Electrostatic gating and multiphysics modeling reveal a local photothermoelectric driving mechanism and elucidate previously unexplored dynamics occurring at the intersection of femtosecond excitation and nanoscale localization.

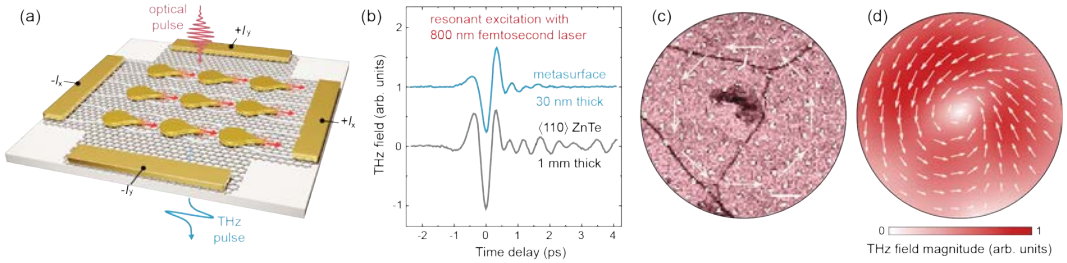

Figure 1. (a) Illustration of the metasurface consisting of symmetry-broken gold nanoantennas on graphene. (b) Femtosecond laser illumination stimulates vectorial photocurrents and consequently efficient emission of ultrafast THz pulses comparable to a ZnTe crystal. (c) SEM image of an azimuthal vector metasurface. (d) Spatial mapping of the measured azimuthal THz vector field upon circularly-polarized excitation.

[1] J. Pettine *et al.*, arXiv.2307.11928 (2023).
[2] J. Pettine *et al.*, *Light Sci. Appl.* **12**, 133 (2023).

+ Author for correspondence: chenht@lanl.gov

Supplementary Figures

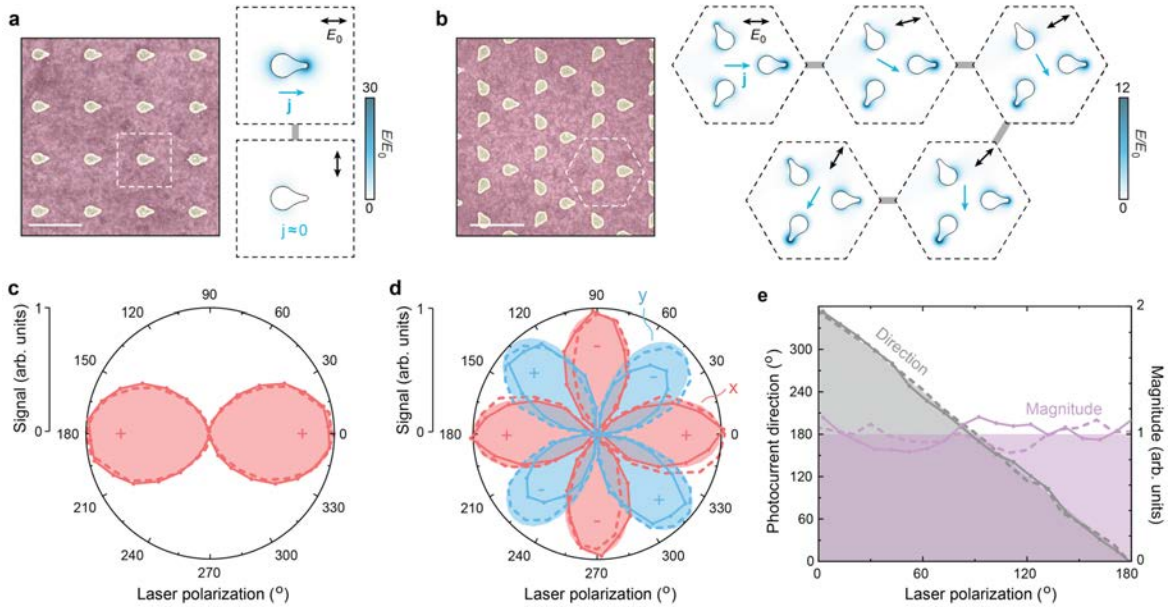

Figure 2. Polarization-dependent local responses and omni-directional control. (a,b) SEM images of uniformly-oriented (a) and Kagome (b) metasurfaces with 800 nm resonances. Scale bars, 500 nm. Insets: Simulated resonant plasmonic field enhancements for different incident linear polarization angles (black double arrows), with the calculated net current direction indicated (blue single arrows). (c,d) Measured *x* (red) and *y* (blue) components of the radiated THz field (solid lines with data markers) and photocurrent (dashed lines) for the uniformly-oriented (c) and Kagome (d) metasurfaces with respect to the incident linear polarization angle. Calculated linear responses (solid fills) are shown for comparison, with ± signs indicating lobe polarity. For clarity, a small residual *y* component is not shown in (c). (e) The Kagome metasurface exhibits nearly constant photocurrent magnitude (purple) and continuously-rotatable direction (gray), consistent with analytic predictions.

Excitons, electrons, and holes in monolayer semiconductors: Insights from spectroscopy in (really) high magnetic fields

S.A. Crooker *
National High Magnetic Field Laboratory, Los Alamos, NM 87545 USA

Historically, magnetic fields have played an essential role in revealing the properties of semiconductors, and the many-body physics that can emerge when they are doped with mobile carriers. However, for atomically-thin 'transition metal dichalcogenide' (TMD) semiconductors such as MoS_2 and WSe_2, the relevant field scale is substantial (of order 100 tesla!) due to heavy carrier masses, huge exciton binding energies, and typically large Fermi energies. Fortunately, modern pulsed magnets can achieve this scale. This talk will discuss a few recent optical studies that probe the physics of -- and many-body correlations between -- excitons, electrons, and holes in TMD monolayers. These experiments used dual-gated TMD monolayers, assembled via van der Waals stacking directly atop single-mode optical fibers to enable polarized absorption spectroscopy at low temperatures in 60-100T fields.

*In charge-neutral monolayers, spectroscopy up to ~90T reveals the diamagnetic shifts of the neutral exciton's *1s* ground state *and* its excited *2s*, *3s*,… *ns* Rydberg states, revealing exciton masses, radii, binding energies, dielectric properties, and free-particle bandgaps – essential ingredients for the rational design of optoelectronic van der Waals structures. [1]

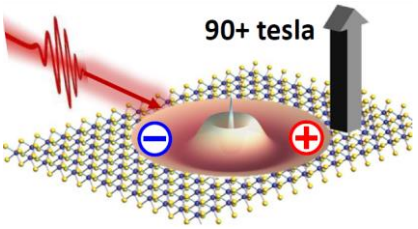

*In hole-doped monolayer WSe_2, high-field spectroscopy of both neutral and charged exciton transitions revealed the (often-hypothesized) spontaneous valley polarization of mobile holes, due to exchange interactions, occurring at ~40T. [2]

*In electron-doped WSe_2 monolayers, the ordering of the conduction bands in the *K* and *K'* valleys allows studies of not only neutral excitons (*X0*) and charged excitons (*X*- trions) at low carrier density, but also many-body states that can emerge at higher doping. We investigate the so-called *X-'* resonance that emerges at high electron density, known since 2013 but never understood. The data suggest that *X-'* is, in fact, a six-particle "hexciton" state that arises when the photoexcited electron-hole pair couples simultaneously to two Fermi seas having quantum-mechanically distinguishable spin/valley quantum numbers. This state also appears in WS_2 and may appear in MoS_2, and appears in $MoSe_2$ at the B-exciton resonance [3,4]

**In collaboration with Xiaodong Xu (U. Washington), Xavier Marie & Bernhard Urbaszek, (INSA-Toulouse), and Hanan Dery (U. Rochester)*

[1] Revealing exciton masses and dielectric properties of monolayer semiconductors with high magnetic fields, *Nat. Commun.* **10**, 4172 (2019).
[2] Spontaneous Valley Polarization of Interacting Carriers in a Monolayer Semiconductor, *PRL* **125**, 147602 (2020).
[3] Many-body exciton and intervalley correlations in heavily electron-doped WSe_2, *Nano Letters* **22**, 426 (2022).
[4] Six-body and Eight-body Exciton States in Monolayer WSe_2, *PRL* **129**, 076801 (2022).

+ Author for correspondence: crooker@lanl.gov

Interface Control of III-Nitride Semiconductors: From High Efficiency Artificial Photosynthesis to Ferroelectric Switching

Zetian Mi

Department of Electrical Engineering and Computer Science, University of Michigan
Ann Arbor, MI48109
ztmi@umich.edu

In this talk, I will discuss the recent advances of nanoscale III-nitride semiconductors and their applications in artificial photosynthesis and ferroelectric devices. Artificial photosynthesis, the chemical transformation of sunlight, CO_2, and H_2O into clean chemicals and fuels, has been extensively studied but faces fundamental challenges of efficiency, stability, and selectivity. Recent studies of III-nitride semiconductors, e.g., GaN, InN, and their alloys, have shown that their surfaces can be transformed to be oxynitride during harsh photocatalysis conditions, leading to significantly improved efficiency and stability. With the integration of various co-catalysts, we have demonstrated high efficiency, long-term stable solar water splitting and hydrogen production. The recent advances of converting CO_2 to liquid fuels, reduction of N_2 to ammonia, and methane oxidation to methanol will also be discussed.

Another recent exciting development is the discovery of ferroelectricity in III-nitride semiconductors. The incorporation of rare-earth elements such as scandium (Sc) can transform conventional III-nitride semiconductors to be ferroelectric. I will present recent advances of ferroelectric Sc-III-nitride heterostructures and nanostructures, including epitaxy, properties, and emerging device applications. Molecular beam epitaxy and properties of ScAlN and ScGaN with a wide range of Sc compositions will be discussed. The realization of ultrathin ferroelectric nitride heterostructures and the underlying physics and interface properties will be discussed, together with their applications in quantum photonics and electronics.

Wafer-Scale Si-Based Metal-Insulator-Semiconductor Photoanodes for Water Oxidation Fabricated Using Thin Film Reactions and Electrodeposition

Shang-Hsuan Wu[1], Soonil Lee[1], Yunho Choi[1], and Edward T. Yu[1*]
[1] *Department of Electrical and Computer Engineering, The University of Texas at Austin, TX, USA*

The environmentally friendly generation of hydrogen (H_2) is anticipated to have a pivotal role in shifting from fossil-based to greener and more sustainable energy systems. Photoelectrochemical (PEC) water splitting is a promising technology for converting solar energy into clean and storable chemical energy and providing carbon-free production of hydrogen for other key applications, e.g., ammonia production. In PEC cells, semiconductors play a key role in absorbing photons from the light source to create mobile charge carriers. Si-based photoelectrodes have drawn much attention due to their moderate bandgap, high charge mobility, long carrier diffusion length, cost-effectiveness, and scalability in manufacturing. To improve the stability of Si-based PEC cells in operation, metal-insulator-semiconductor (MIS) structures have been widely employed [1]. In MIS photoelectrodes, the insulator thickness plays a key role in such MIS photoelectrodes since it influences both efficiency and long-term stability. Photo-generated charges are typically extracted from the semiconductor to the metal catalyst via tunneling through the insulator, mandating the use of extremely thin insulators. However, optimal stability generally motivates the use of thicker insulators.

In this work, we employ a simple and highly scalable method to fabricate high-performance, extremely stable Si-based MIS photoanodes and demonstrate its application to the fabrication of wafer-scale photoanodes. Localized conduction paths formed via an Al/SiO_2 thin-film reaction enable low-resistance charge extraction even through thick insulating layers, and this approach has been shown in our previous work to yield photoanodes with excellent stability [2]. In addition, we demonstrate a two-step Ni/NiFe electrodeposition process to create efficient OER catalysts. The Ni/NiFe catalyst allows for a high Schottky barrier between Si and Ni, lowering the photoanode onset potential, while the NiFe surface layer improves catalytic performance. An unassisted solar-driven water splitting system integrated with wafer-scale photoanode and monocrystalline Si solar cells is demonstrated under both AM 1.5G sunlight simulator and outdoor illumination, with solar-to-hydrogen efficiency of 6.9% achieved with a full-wafer photoanode and minimal optimization.

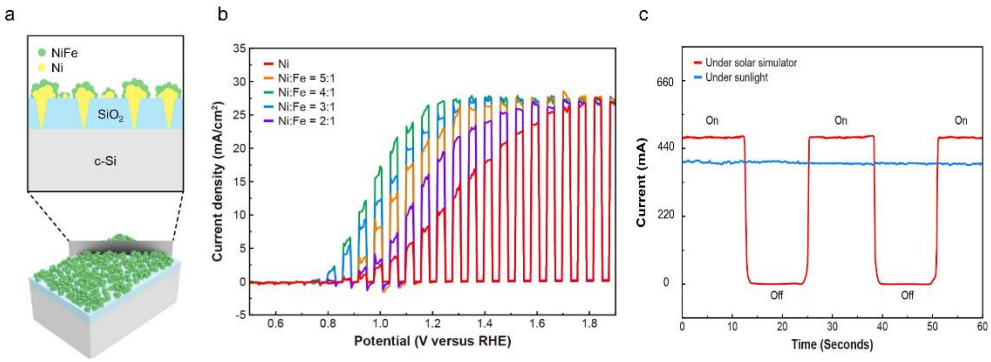

Figure 1. ***(a)*** *Schematic illustrations of the spiked NiFe/Ni/SiO_2/Si MIS photoanode structures.* ***(b)*** *LSV curves for spiked NiFe/Ni/SiO_2/Si photoanodes with different Ni:Fe ratios in the NiFe catalyst layers (Ni:Fe = 5:1, 4:1, 3:1, and 2:1).* ***(c)*** *chronoamperometry test of the unassisted solar-driven wafer splitting system under AM 1.5G simulated solar illumination and real outdoor sunlight.*

[1] M. J. Kenney, M. Gong, Y. Li, J. Z. Wu, J. Feng, M. Lanza, H. Dai, Science, 342, 6160, 836-840, (2013)
[2] S. Lee, L. Ji, A. C. De Palma, E. T. Yu, Nature Communications, 12, 3982, (2021)

Supplementary Pages

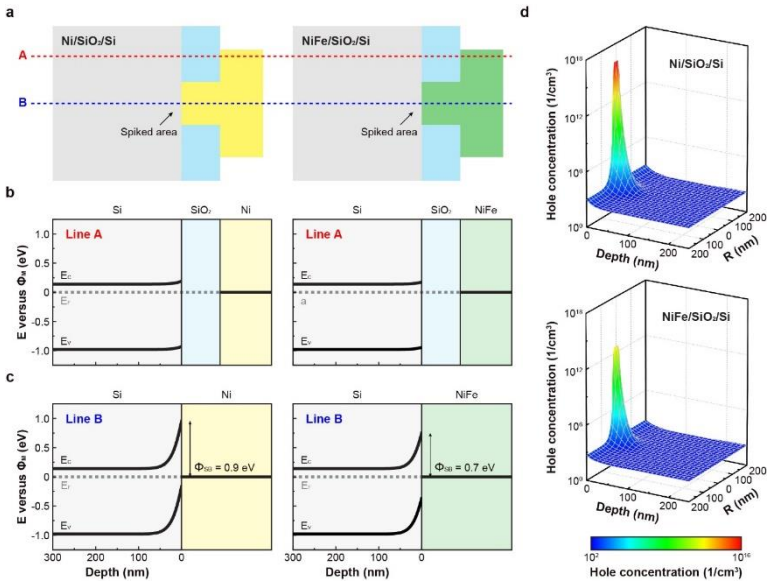

Figure 2. *Simulations showing potential distributions for different models.* ***(a)*** *Schematic illustration of simulated model structures for MIS photoanodes: Ni/SiO₂/Si (Model 1) and NiFe/SiO₂/Si (Model 2) with 90 nm SiO₂ thickness and center spikes.* ***(b, c)*** *Simulated band diagrams at the interface area along the lines labeled in part (a) as A (b) and B (c) for Ni/SiO₂/Si and NiFe/SiO₂/Si.* ***(d)*** *Simulated hole concentration near the spiked area for Ni/SiO₂/Si and NiFe/SiO₂/Si structures.*

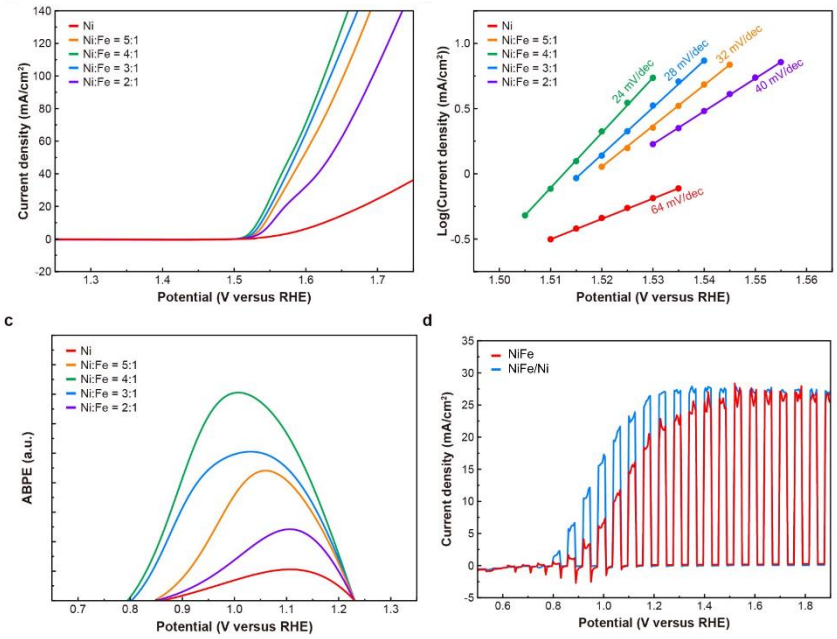

Figure 3. *PEC characterization of photoanodes for different Ni:Fe ratios.* ***(a)*** *OER polarization curves and* ***(b)*** *Tafel plots for electrodeposited NiFe films on Ni plates in 1 M KOH solution with different Ni:Fe ratios in NiFe alloys (Ni:Fe = 5:1, 4:1, 3:1, and 2:1).* ***(c)*** *normalized ABPE curves for spiked NiFe/Ni/SiO₂/Si photoanodes with different Ni:Fe ratios in the NiFe catalyst layers (Ni:Fe = 5:1, 4:1, 3:1, and 2:1).* ***(d)*** *LSV curves with chopped illumination in 1 M KOH solutions for the spiked NiFe/SiO2/Si and spiked NiFe/Ni/SiO₂/Si photoanodes (Ni:Fe = 4:1).*

Field-assisted oxidation of a Fe single nanoparticle, nanoscale observations by Operando Atom Probe

Sten V Lambeets[1+], Naseeha Cardwell[2], Isaac Onyango[2], Thierry Visart de Bocarmé[3]; Jean-Sabin McEwen[1,2], Daniel E Perea[3]

[1] PCSD, Pacific Northwest National Laboratory, Richland WA, USA

[2] The Gene and Linda Voiland school of Chemical Engineering and Bioengineering, Washington State University, Pullman WA, USA

[3] Chemistry of Surfaces, Interfaces and Nanomaterials, Campus Plaine - CP 243, Université Libre de Bruxelles, B-1050 Brussels, Belgium

[4] EMSL, Pacific Northwest National Laboratory, Richland WA, USA

Mechanisms governing surface chemical reactions involved in heterogenous catalysis fundamentally depends on the synergistic interactions between the reactants and the different surface structures present at the surface. Recently, special attention has been raised regarding the influence of intense electric fields on these mechanisms [1]. An increasing number of analytical surface science techniques are achieving their conversion to their respective in-situ/operando version to study surface reactions at the "applied" conditions. Amongst them, Atom Probe Microscopy (APM) techniques are particularly interesting for their inherent use of intense electric fields and their capability to image matter at the nanoscale. In this work, we will present a nanoscale study of the field-assisted oxidation of a single Fe nanoparticle using Field Ion Microscopy (FIM) and Operando Atom Probe (OAP).

APM techniques are capable of imaging the apex of sharp needles, mimicking model nanoparticles, with nanometric lateral resolution. FIM is used to image apices with atomic resolution and to identify the crystal orientations with their Miller indices using stereographical projection. OAP relies on the thermally assisted field evaporation of positively charged ions from a needle shaped specimen [2]. Once the FIM characterization is complete the sample is maintained at 300K with an applied electric field of ~20V/nm, before starting OAP analysis and introducing 1.1×10^{-7}mbar of pure O_2. As soon as the O_2 is introduced, Fe_2O^{n+} ion species formation are observed starting from open facets structures, such as Fe{244} and {112}, towards the central Fe(011) and {024} (Fig.1). OAP results allow us to reconstruct the full movie of the surface oxidation in real-time and show how intense electric fields (>10V/nm) play a central role in surface chemistry.

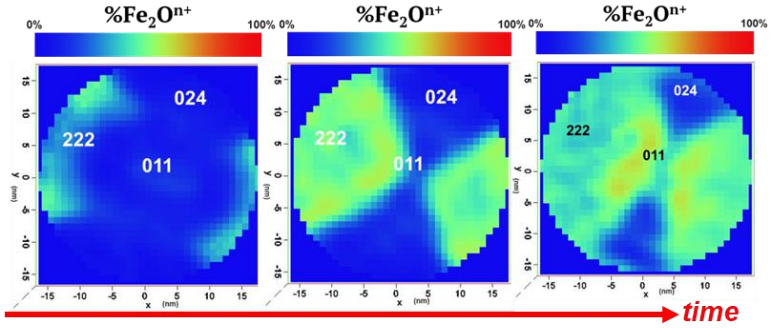

Figure 1. Fe oxidation imaged by OAP.

[1] Che F. et al. ACS Catalysis, **8(6)**, 5153(2018)

[2] Lambeets S.V. et al. Topics in Catalysis, **63(15-18)**, 1606(2020)

[+] Author for correspondence: sten.lambeets@pnnl.gov

Crystalline Materials with Anisotropic Conduction Polarities

J. E. Goldberger[1]

[1]Department of Chemistry and Biochemistry, The Ohio State University, 151 W. Woodruff Ave., Columbus, OH 43210

It is conventionally thought is that a single material will exhibit a single kind of conduction polarity, either n-type or p-type, uniformly along all directions of the crystal. Then, in all modern electronic devices, functionality is achieved by integrating together these p-type or n-type materials together. Here we will describe our recent work in the synthesis, properties, and applications of metals and semiconducting materials that exhibit either n-type or p-type conduction behavior depending on the crystallographic direction, a phenomenon we refer to as "goniopolarity". We will establish the origin of this exotic behavior and the band structure design principles for identifying new goniopolar materials.[1] This has led to a large expansion in the number of compounds that we have experimentally demonstrated to exhibit this effect, such as $NaSn_2As_2$, NaSnAs, WSi_2 and $PdSe_2$.[2-5] Finally, we will show that the unique charge separation in goniopolar materials can overcome limitations of energy-harvesting technologies including thermoelectrics and photocatalysis.

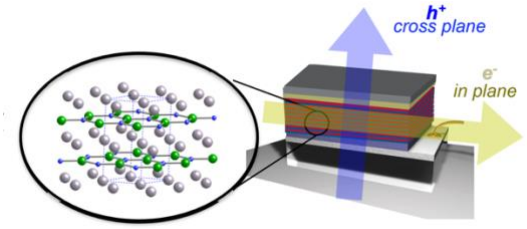

Figure 1. Schematic illustration of a layered material with axis-dependent conduction polarity.

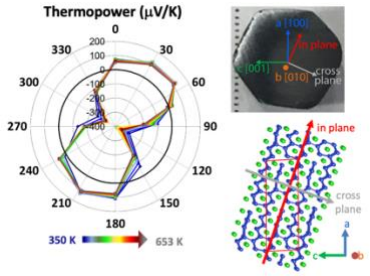

Figure 2**.** Thermopower polar plot of Re_4Si_7 measured from 350–650 K at different orientations along the *ac*-plane. 0° corresponds to the *a* [100] direction and the crystal is in the same orientation as the crystal cross-section and crystal structure shown on the right.

[1] Y. Wang; K. G. Koster; A. M. Ochs; M. R. Scudder; J. P. Heremans; W. Windl; J. E. Goldberger, *J. Am. Chem. Soc.* **142**, 2812-2822(2020).
[2] B. He; Y. Wang; M. Q. Arguilla; N. D. Cultrara; M. R. Scudder; J. E. Goldberger; W. Windl; J. P. Heremans, *Nat. Mater.* **18**, 568-572(2019).
[3] K. G. Koster; Z. Deng; C. E. Moore; J. P. Heremans; W. Windl; J. E. Goldberger, *Chemistry of Materials* **35**, 4228-4234(2023).
[4] R. A. Nelson; Z. Deng; A. M. Ochs; K. G. Koster; C. T. Irvine; J. P. Heremans; W. Windl; J. E. Goldberger, *Mater. Horiz.* **10**, 3740-3748 (2023).
[5] A. M. Ochs; P. Gorai; Y. Wang; M. R. Scudder; K. Koster; C. E. Moore; V. Stevanovic; J. P. Heremans; W. Windl; E. S. Toberer; J. E. Goldberger, *Chem. Mater.* **33**, 946-951(2021).

+ Author for correspondence: Goldberger.4@osu.edu

Weyl Semimetals and the Interface: Surface State Transport Probed Via Weak Antilocalization in Ultrathin TaAs Films

I. A. Leahy, A. D. Rice, C. S. Jiang, G. Paul, K. Alberi, and J. N. Nelson
National Renewable Energy Laboratory, Golden, Colorado 80401, USA

Topological semimetals hold promise for their use in low-powered electronics and spintronic devices [1-4] but these applications await targeted growth on conventional semiconducting substrates and the exploration of their properties in the ultrathin limit. Weak antilocalization (WAL) has been used extensively in the study of surface states in topological insulators and shows promise for the study of surface states in Weyl semimetals (WSMs). WAL is a quantum interference effect that results in an increase in a system's conductivity owing to the suppression of back-scattering from self-intersecting carrier paths. This quantum interference requires carriers maintain phase coherence over multiple scattering events. The length over which carriers maintain coherence is defined as the decoherence length. In an applied field, the WAL is destroyed when the magnetic length approaches the decoherence length, offering a natural insight into the localizing disorder length scales. Here we report on insights from WAL into the surface state and interface properties of the recently synthesized, single-crystal-like ultrathin films of Weyl semimetal TaAs(001) grown on GaAs(001) substrates [5-7].

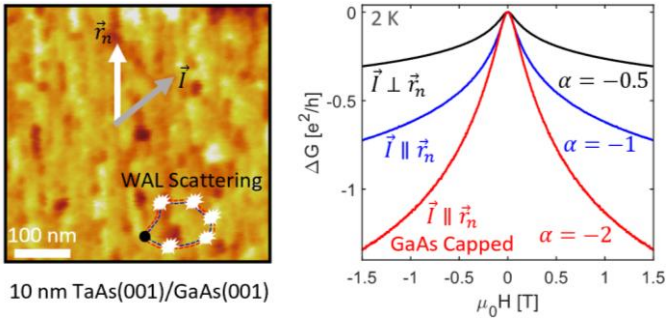

Figure 1: AFM (left) and magnetoconductance (right) for 10 nm TaAs(001) grown on GaAs(001). Rod-like features approximately 100 nm long and 20-40 nm wide are oriented along the $(\bar{1}10)$ direction. The vector $\vec{r}_n$ defines the orientation of the rods. The measured magnetoconductance We observe a magnetoconductance that depends on the orientation of the applied current relative to the film topography as well as the number of GaAs/TaAs interfaces.

Figure 1 shows atomic force microscopy and magnetoconductance for representative TaAs ultrathin films. AFM on a 10 nm thick TaAs film on GaAs reveals oriented, rod-like growth along $\vec{r}_n$ – the $(\bar{1}10)$ direction. At low temperatures, the magnetoconductance exhibits clear signatures of WAL. Intriguingly, we find that the number of apparent WAL conduction channels depends on the orientation of the applied current relative to the film topography as well as the number of GaAs/TaAs interfaces. We hypothesize that this unique anisotropic WAL stems from a topological and trivial state with different decoherence lengths localized at each interface.

References:

[1] J. Hu, S. Xu, Z. Mao, Annual Review of Materials Research 49:1, 207-252 (2019).
[2] I. Leahy, et. al., Proceedings of the National Academy of Sciences, 1808747115 (2018).
[3] H. Chorsi, et. al., Advanced Functional Materials, 32:19, 2110655 (2022).
[4] B. Zhao, et. al., Advanced Materials, 32:38, 200818 (2020).
[5] J. N. Nelson et. al., Matter 6, 2886 (2023).
[6] J. Sadowski et. al., Crystal Growth and Design 22, 6039 (2022).
[7] I. A. Leahy et. al., In Revision at ACS Nano (2023).
[+] Author for correspondence: Ian.Leahy@nrel.gov

Topological Hall effect in Dirac semimetal

S. Islam,[1] E. Steinebronn[1], B. Neupane,[2] K. Yang,[1] Y. Wang,[2] C. Liu,[1] J. Chamorro,[3] T. M. McQueen,[3] and N. Samarth[1]

[1] Department of Physics, Pennsylvania State University, University Park, PA: 16802
[2]Department of Physics, University of North Texas, Denton, Texas 76203
[3]Department of Chemistry, Johns Hopkins University, Baltimore, Maryland 21218

Magnetic skyrmions are chiral spin textures whose non-trivial real space topology is often created by an interfacial anisotropic Dzyaloshinkii-Moriya exchange interaction (DMI) that originates from spin-orbit coupling and broken inversion symmetry [1]. They have been observed in a wide variety of bulk single crystals such as MnSi [2] and thin films such as $Fe_{1-x}Co_xSi$ [3]. More recently, magnetic skyrmions have been probed at ferromagnet/topological insulator interfaces [4] and in magnetic Weyl semimetals [5]. This motivates similar explorations of skyrmion formation in Dirac semimetals (DSMs). We investigate the formation of skyrmions at the interface of a canonical DSM (Cd_3As_2) and a ferromagnetic semiconductor ($In_{1-x}Mn_xAs$) with perpendicular magnetic anisotropy. Our calculations indicate nonzero spin susceptibility in such heterostructures due to Rashba spin-orbit coupling from broken inversion symmetry, implying the DM interaction necessary for skyrmions. To experimentally test this ideas, we grew $Cd_3As_2/In_{1-x}MnAs$ bilayers (Fig. 1a) and mapped out the behavior of the Hall effect as a function of temperature, magnetic field, and gate voltage in electrostatically top gated devices. Below T = 6 K, we observe an emergent gate-tunable topological Hall effect (THE) indicated by an excess Hall resistance (Fig. 1b). This signature is most pronounced at the charge neutrality point, suggesting the formation of a Dirac-electron mediated chiral spin texture at the DSM/ferromagnet interface. Our study provides a new platform to study the interplay between the topological states in DSMs and the chiral spin textures associated with the THE. Supported by the NSF Graduate Research Fellowship Program (Grant No. DGE1255832).

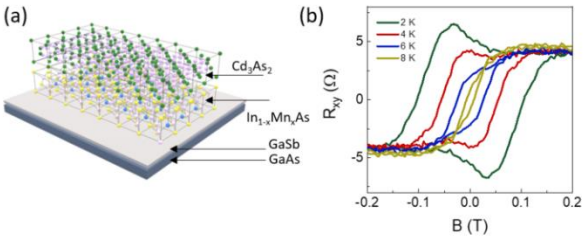

Fig. 1. (a) Device structure. (b) Hall resistance (R_{xy}) at different T showing excess R_{xy}

[1] A. Fert, N. Reyren, and V. Cros, Nat. Rev. Mater., 2, 1 (2017).
[2] S. Mühlbauer et al., Science 323, 915–919 (2009)
[3] X.-Z. Yu *et al.*, *Nature* **465**, 901–904 (2010)
[4] P. Li *et al.*, Nano Lett., 21, 1, 84–90 (2021)
[5] P. Pushpan *et al.*, *Phys. Rev. Lett.* 124, 017202 (2020)

[+] Author for correspondence: ski5160@psu.edu, nxs16@psu.edu

Supplementary Pages

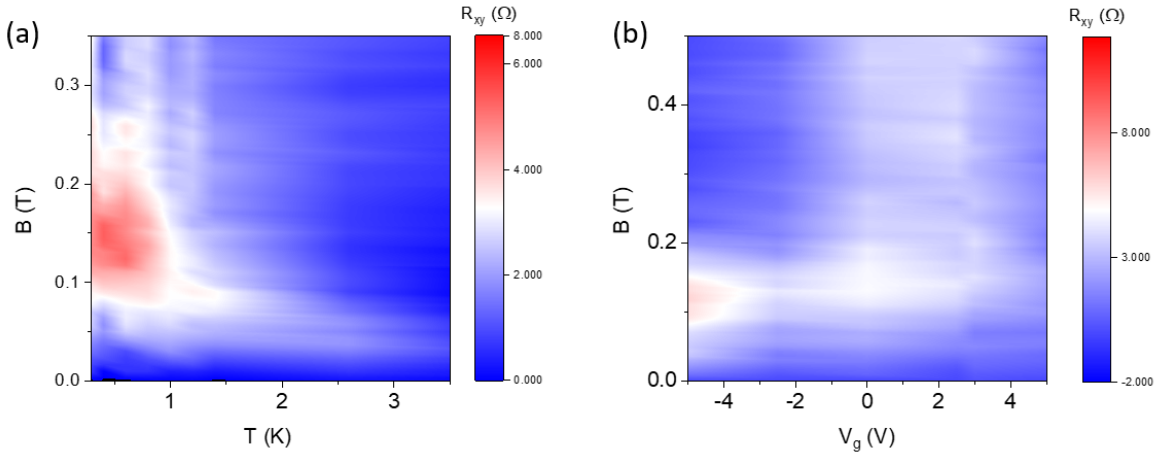

Figure 2. (a) Temperature-dependence of Hall resistance (R_{xy}) showing the excess resistance reduces as temperature is reduced. (b) Gate-voltage dependence of R_{xy} showing the excess resistance is most pronounced close to the charge neutrality point of the heterostructure.

Helical dislocations in 2D materials and the connection to transport in topological insulators

Tawfiqur Rakib,[1] Moon-Ki Choi,[1] Elif Ertekin, [1] Pascal Pochet, [2] and Harley T. Johnson,[1]

[1] Department of Mechanical Science & Engineering, Materials Research Laboratory, University of Illinois at Urbana-Champaign, 104 S. Goodwin Ave., Urbana, IL 61801

[2] Laboratoire Modélisation et Exploration des Matériaux, CEA, 17 Avenue des Martyrs 38000 Grenoble, France

Layered two-dimensional materials host a variety of crystalline defects, including dislocations either in-plane or out-of-plane with respect to the 2D layered structure. Recently, twisted multilayer 2D material structures have been of interest due to the presence of flat bands and other emergent properties associated with moiré superlattices.[1] Periodic regions of crystalline commensurability making up these superlattices are now understood to be separated by interlayer dislocations, with Burgers vectors and line directions in the plane of the 2D material, and having either edge or screw character.[2] Using density functional theory and quantum Monte Carlo-fitted total energy tight-binding calculations, we show that out-of-plane relaxation of the structures makes possible unique helical dislocations in bilayer graphene, and that the presence of these helical dislocation lines coincides precisely with the so-called magic-angle condition at which unconventional superconductivity is observed.[3] We then illustrate a different dislocation structure, with line direction oriented out-of-plane, but which also has a helical structure. Such a screw dislocation, which adopts a double-helix dislocation core configuration in bilayer structures, is expected to create conditions for exotic transport properties in certain classes of layered topological insulator materials. We present initial results demonstrating this possibility in BiTe and BiSe compounds. In these examples, we present relaxed dislocation core structures computed using first-principles methods, and show that the observed configurations match both experimental observations and the theoretical conditions that are expected to lead to quantum conduction in these otherwise topologically insulating materials.

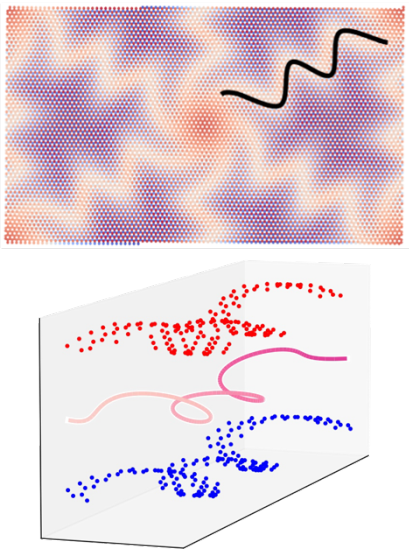

Figure 1: (top) plan view of bilayer graphene moiré superlattice, with local energy shown in color. (bottom) expanded 3D view of atom positions in upper and lower layers along black line from upper image. The center of the helical dislocation core is shown between the layers.

[1] Cao, Y. et al., Unconventional superconductivity in magic-angle graphene superlattices, Nature **556**, 43-50 (2018).

[2] Pochet, P., B. C. McGuigan, J. Coraux, and H. T. Johnson, Toward moiré engineering in 2D materials via dislocation theory, Applied Materials Today **9**, 240-250 (2017).

[3] Rakib, T., P. Pochet, E. Ertekin, and H. T. Johnson, Helical dislocation in twisted bilayer graphene, Extreme Mechanics Letters, **63**, 102053 (2023).

[+] Author for correspondence: htj@illinois.edu

Layer-dependent Optical Conductivity of MBE-grown $ZrTe_2$

E. Houser,[1] F. Peiris,[1] A. Richardella,[2] M. Stanley,[2] and N. Samarth,[2]
[1]Department of Physics, Kenyon College, Gambier, Ohio 43022
[2]Materials Research Institute, Pennsylvania State University, PA 16802.

Besides providing an interesting platform to interrogate fundamental physics questions, two-dimensional transition metal dichalcogenides (TMDCs) are well suited to advance the development of optoelectronic technologies. In this work, we investigated the growth and the optical properties of $ZrTe_2$, a candidate topological Dirac semimetal, grown using molecular beam epitaxy. During the growth of 12 unit cells (u.c.) of $ZrTe_2$ on a sapphire substrate, we obtained in-situ spectroscopic ellipsometry after the deposition of each u.c. Additionally, we obtained temperature dependent ellipsometry data on the sample between 20 °C and 350 °C. After the deposition of the $ZrTe_2$ layers, a Te capping layer was deposited in order to protect the TMDC film. Post-growth X-ray reflectivity measurements indicated that the total thickness of $ZrTe_2$ and the thickness of Te to be 5.95 nm and 19 nm, respectively.

A standard inversion technique was used to model the ellipsometry spectra by specifying a three layer model (i.e., sapphire substrate, $ZrTe_2$ layer and the Te capping layer) to fit the final ellipsometry spectra. The thicknesses obtained from X-ray reflectivity allowed us to obtain the precise dielectric function of the final $ZrTe_2$ layer (i.e., 12 u.c.), which was converted to the optical conductivity. Subsequently, we fit the remaining ellipsometry spectra obtained for 11 u.c. through 1 u.c. $ZrTe_2$ layers. Clearly, the optical conductivity shows a noticeable change with the thickness of the $ZrTe_2$ layers, where the real part increases with the thickness of $ZrTe_2$, as shown in Fig. 1. The layer-dependent conductivity was further analyzed by incorporating a Drude oscillator to account for free electrons, and two Kramers-Kronig-consistent oscillators to represent the band-to-band transitions. Interestingly, we find that the Drude contribution reduces as the thickness of $ZrTe_2$ gets smaller, suggesting that its metallic character diminishes as the thickness reduces.

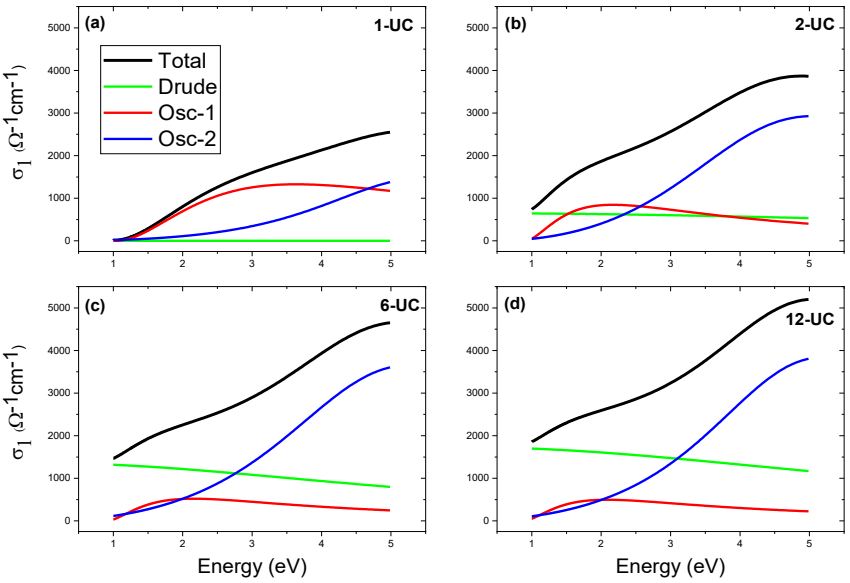

Fig. 1. Total conductivity (black-lines) and contributions from free electrons (green-lines) and band electrons (red and blue lines) for different thicknesses of $ZrTe_2$.

Surface dependent doping efficiency in Te:Cd_3As_2 Thin films

Anthony D. Rice[1], I. Leahy[1], K. Alberi[1]
[1] *National Renewable Energy Laboratory, Golden, CO 80401, USA*

Cd_3As_2 is a prototypical Dirac semi-metal, a class of materials with gapless topologically protected electronic states. In this system, these topological electronic states are close to the intrinsic Fermi level and are well isolated from non-trivial bands. Additionally, this system is air stable and compatible with molecular beam epitaxy, including lattice matching to III-Sb and II-Te layers, and similar elements to conventional semiconductors. These materials could play a role in a large number of applications, including transistors, spintronics, photodetectors, and thermoelectrics. To do this, however, significant progress must be made on achieving tunability of these materials. In particular, routes to altering its typical n-type carrier concentration must be developed.

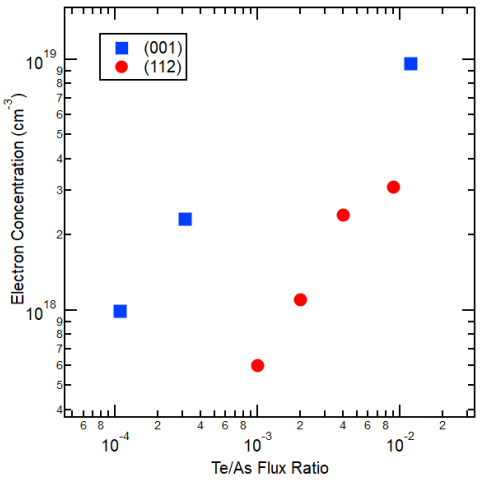

Figure 1. Electron concentration vs dopant flux ratio in Cd_3As_2 thin films of two different orientations

Previous attempts to dope Cd_3As_2(112) with group VI elements, including Te and Se, were successful, allowing for increases of n_{3d} from 5e17 cm^{-3} up to slightly over 3e18 cm^{-3} [1]. Concentration vs mobility relationships appeared similar to doping in convention semiconductors, with mobility decreasing with increased ionized impurities. Attempts to increase doping beyond this level by using increased group VI fluxes resulted in lower measured Hall concentrations and even larger decreases in mobility, a sign that compensating defects are forming. When similar doping is attempted on the (001) surface, however, doping beyond 1e19 cm^{-3} is possible. Furthermore, an order of magnitude smaller Te fluxes are required to achieve similar doping levels. Finally, smaller unintentionally doped carrier concentrations are achievable on this surface. This work highlights the role of surface kinetics in defect incorporation in topological semi-metals.

[1] A.D. Rice et al. Appl. Phys. Lett. 122, 061901 (2023)

+ Author for correspondence: Anthony.rice@nrel.gov

Investigating the Structural and Electronic Properties of FeSn on $LaAlO_3$ (111) Grown By Molecular Beam Epitaxy

T. Erickson,[1] S. Upadhyay,[1] H. Hall,[1] A. Shrestha,[1] A. Abbas,[1] D. Ingram,[1] S. Kaya,[2] and A. R. Smith[1]

[1] Ohio University Department of Physics and Astronomy, 136 University Terrace Athens, Oh 45701

[2] Ohio University Department of Electrical Engineering and Computer Science, 1 Ohio University Stocker Center 270 Athens, Oh 45701

The Kagome lattice of 3-d transition metals produces exciting electronic excitations through correlated topological phases due to a mixture of the unique geometry and spin-orbit coupling [1,2]. Research into these materials continues to provide insight into electronic properties of Dirac-bands in transition metal materials. FeSn with its Fe_3Sn Kagome layers separated by honeycomb Sn_2 layers provides ample opportunity to study these phenomena. Recent scanning tunneling microscopy (STM) studies into FeSn confirm the expected antiferromagnetic spin order consistent with bulk measurements, demonstrating a ferromagnetic alignment within Kagome layers and antiferromagnetic coupling between separate layers [3,4]. Currently, these findings are for bulk FeSn samples transported to and cleaved in ultra-high vacuum chambers. Here, we perform direct *in-situ* UHV-STM analysis of FeSn samples *as-grown* by molecular beam epitaxy. We grew our FeSn on $LaAlO_3$ substrates at temperatures ranging from 450 to 550 °C and Fe:Sn flux ratios of 0.64:1 to 1.52:1. $LaAlO_3$ and FeSn have a lattice match with a difference of only 1%. We also compare the results samples by means of RHEED, XRD, RBS, and AFM. In all cases, smooth streaky RHEED patterns are observed, and from the streak spacing we calculate the *in-plane* lattice constants which are then complemented by the lattice constants calculated from the XRD spectra. For the case of the 1.52:1 flux ratio, using RHEED we find an $a = 5.240 \pm 0.017$ Å as compared to the expected value for the FeSn lattice parameter $a = 5.297$ Å [2], and using XRD we find $c = 4.436 \pm 0.042$ Å as compared to the expected c for FeSn = 4.481 Å [2]. In this presentation, we will discuss the lattice parameters as functions of the incident flux ratios as well as the phases and phase purity of the resultant samples. Additionally, AFM and RBS results are used to describe the smoothness and stoichiometry respectively.

This work is supported by the U.S. Department of Energy, Office of Basic Energy Sciences, Division of Materials Sciences and Engineering under Award No. DE-FG02-06ER46317.

[1] Kang, M., Ye, L., Fang, S. et al. Nat. Mater. 19, 163–169 (2020).
[2] Yin, JX., Zhang, S.S., Li, H. et al. Nature 562, 91–95 (2018).
[3] Li, H., Zhao, H., Yin, Q. et al. Sci Rep 12, 14525 (2022).
[4] Lee, SH., Kim, Y., Cho, B. et al. Commun Phys 5, 235 (2022).
[+] Author for correspondence: te467518@ohio.edu

Supplementary

RHEED is conducted *in-situ* to observe sample growth and calculate in-plane lattice parameters after growth has finished. The RHEED profiles are taken along both directions and show 6-fold symmetry, indicative of a hexagonal lattice. The XRD profiles are taken from a tabletop Rigaku powder diffractometer *ex-situ*.

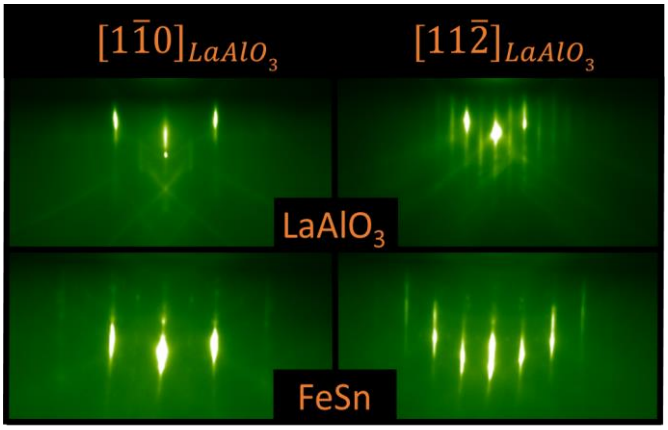

Figure 2. RHEED image of sample 216 grown at 500 °C with Fe:Sn flux ratio of 0.64:1. The RHEED patterns for the FeSn are taken after the growth has finished and the sample has come back down to room temperature.

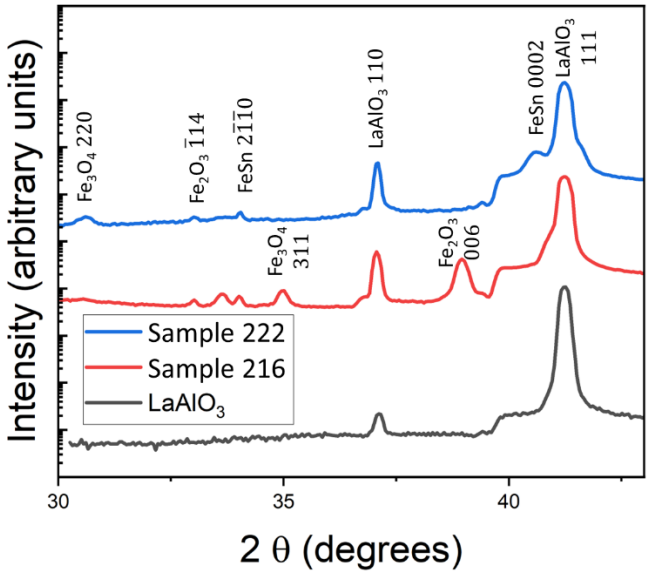

Figure 1. XRD plot of FeSn on $LaAlO_3$. Samples 216 and 222 grown at 500 °C with Fe:Sn flux ratios of 0.64:1 and 1.52:1. The samples are offset from one another to show the positions of identifiable peaks.

Ultra-quantum Limit Magnetotransport in the Topological Pentatellurides

J. C. Palmstrom,[1] C. Kaufmann Ribeiro,[1,2] C. Mizzi,[1] L. E. Winter,[1] S. Thomas,[3] J. Liu[4], L. A. Jauregui,[4] J. Mutch,[5] Q. Jiang,[5] J. Ayres-Sims,[5] J.-H. Chu,[5] E. A. Peterson,[6] and J.-X. Zhu[6,7]

[1] NHMFL, Los Alamos National Laboratory, Los Alamos, NM 87545, USA
[2] Laboratory for Quantum Matter under Extreme Conditions, Institute of Physics, University of São Paulo, São Paulo, Brazil
[3]MPA-Q, Los Alamos National Laboratory, Los Alamos, New Mexico 87545, USA
[4]Department of Physics and Astronomy, University of California, Irvine, CA 92697, USA
[5]Department of Physics, University of Washington, Seattle, WA 98105
[6]Theoretical Division, Los Alamos National Laboratory, Los Alamos, NM 87545, US
[7]Center for Integrated Nanotechnologies, Los Alamos National Laboratory, Los Alamos, NM 87545, US

With low carrier concentrations and high mobilities, the pentatelluride material family ($HfTe_5$ and $ZrTe_5$) typically have a quantum limit of a few Tesla, making them an ideal platform to study ultra-quantum limit phenomena and magnetic field-induced effects in a three dimensional (3D) Dirac fermion system. In the quantum limit, the magnetic field is strong enough to confine all the electrons to their lowest Landau levels, resulting in a quantized in-plane dispersion, lower effective dimensionality, and a system that is more unstable to electronic correlations. Previous experiments in the pentatellurides have revealed many exotic high-field phenomena including an interaction driven instability [1] and a field induced Lifshitz transition [2]. These materials sit right at the cusp of a strong-to-weak 3D topological phase transition, resulting in a band structure and electronic properties that are extremely sensitive to external tuning parameters such as magnetic field and strain [3]. Consequently, while these systems are promising for the extrinsic control of topological properties, there are many controversies surrounding their intrinsic behavior as the electronic properties depend on the sample growth and preparation conditions [4].

In this work we report on the ultra-quantum limit electronic properties and magnetic field-temperature phase diagram of flux grown, bulk $HfTe_5$ as revealed by magnetotransport measurements in pulsed magnetic fields up to 65 T (Fig. 1). These samples show a purely insulating resistance vs temperature behavior in zero field. We find a strong and non-monotonic angle dependence of the magnetoresistance and several high field features in the ultra-quantum limit. The interpretation of these features will be discussed during the presentation.

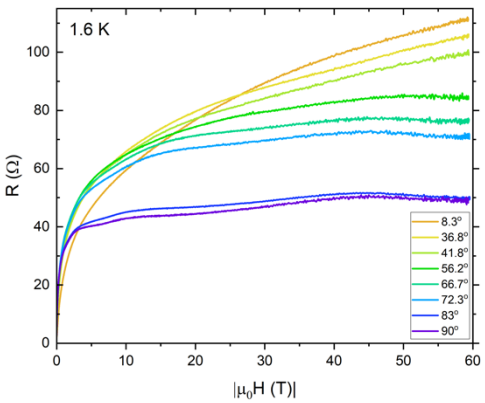

Figure 1: Pulsed field magnetotransport of $HfTe_5$ as a function of in-plane magnetic field angle. H⊥a, I//a.

[1] L. Yanwen et al. Nat. Commun. **7**, 12516 (2016)
[2] S. Galeski et al. Nat. Commun. **13**, 7418 (2022)
[3] J. Mutch et al. Sci. Adv. **5**, eaav9771 (2019)
[4] J. Liu et al. arXiv:2304.09072 (2023)
[+] Author for correspondence: jpalmstrom@lanl.gov

Tuning the Curie Temperature of a 2D Magnet/Topological Insulator Heterostructure to Above Room Temperature by Epitaxial Growth

Wenyi Zhou,[1] Alexander J. Bishop,[1] Xiyue S. Zhang,[2] Katherine Robinson,[1] Igor Lyalin,[1] Ziling Li,[1] Ryan Bailey-Crandell,[1] Thow Min Jerald Cham,[2] Shuyu Cheng,[1] Yunqiu Kelly Luo,[2, 3, 4] Daniel C. Ralph,[2, 3] David A. Muller,[2, 3] and Roland K. Kawakami[1]

[1]The Ohio State University, Department of Physics, Columbus, OH, USA
[2]Cornell University, Department of Physics, Ithaca, NY, USA
[3]Kavli Institute at Cornell, Ithaca, NY, USA
[4]University of Southern California, Department of Physics and Astronomy, Los Angeles, CA, USA

Heterostructures of two-dimensional (2D) van der Waals (vdW) magnets and topological insulators (TI) are of substantial interest as candidate materials for efficient spin-torque switching, quantum anomalous Hall effect, and chiral spin textures. However, since many of the vdW magnets have Curie temperatures below room temperature, we want to understand how materials can be modified to stabilize their magnetic ordering to higher temperatures. In this work, we utilize molecular beam epitaxy to systematically tune the Curie temperature (T_C) in thin film Fe_3GeTe_2/Bi_2Te_3 from bulk-like values (~220 K) to above room temperature by increasing the growth temperature from 300 °C to 375 °C (Figure 1). For samples grown at 375 °C, cross-sectional scanning transmission electron microscopy (STEM) reveals the spontaneous formation of different $Fe_mGe_nTe_2$ compositions (e.g. $Fe_5Ge_2Te_2$ and $Fe_7Ge_6Te_2$) as well as intercalation in the vdW gaps, which are possible origins of the enhanced Curie temperature. This observation paves the way for developing various $Fe_mGe_nTe_2$/TI heterostructures with novel properties.

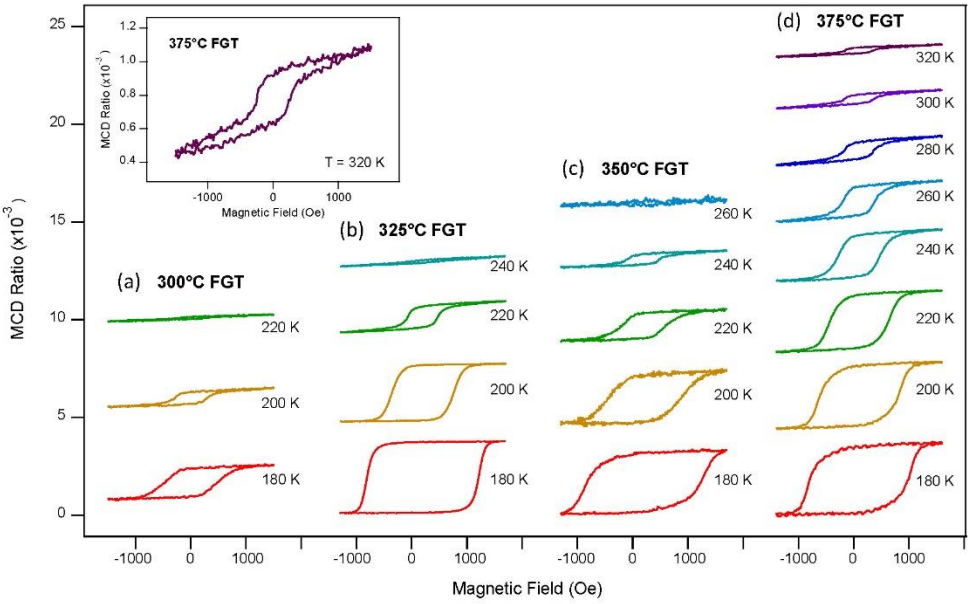

Figure 1. Temperature dependence of MCD loops for FGT samples (~ 4 nm) grown at 300 °C, 325 °C, 350 °C, and 375 °C on Bi_2Te_3.

Supplementary Pages

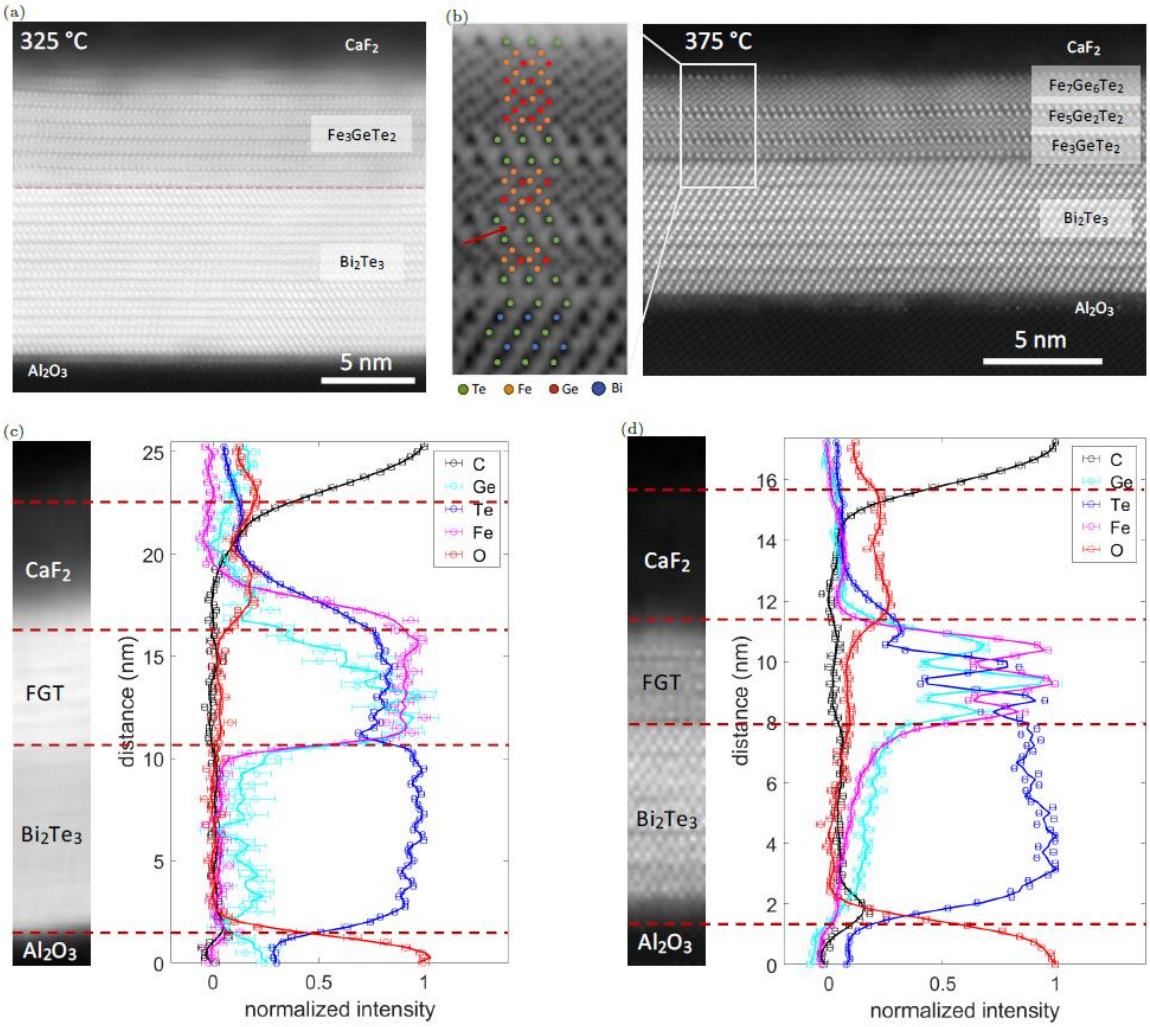

Supplementary Figure. STEM investigations. (a) HAADF STEM image of an FGT(6.4nm)/Bi_2Te_3(10 nm) heterostructure grown at 325 °C (for FGT). (b) HAADF STEM image of an FGT(4 nm)/Bi_2Te_3(8 nm) heterostructure grown at 375 °C (for FGT) and a zoomed in BF STEM image with different atoms marked out in the left. The red arrow indicates the position of an intercalant atom. (c) EELS line profile of the FGT(6.4 nm)/Bi_2Te_3(10 nm) heterostructure grown at 325 °C (for FGT) with the corresponding HAADF image on the left. (d) EELS line profile of the FGT(4 nm)/Bi_2Te_3(8 nm) heterostructure grown at 375 °C (for FGT) with the corresponding HAADF image on the left.

Kagome Antiferromagnetic Mn_3GaN grown on MgO(001) using Molecular Beam Epitaxy

A. Abbas,[1] A. Shreshtha[1], S. Upadhyay[1], T. Erickson[1], K. Sun[2], David C. Ingram[1], and A. R. Smith[1]

[1] Nanoscale and Quantum Phenomena Institute, Department of Physics and Astronomy, Ohio University, Athens, OH 45701

[2] Department of Materials Science and Engineering, The University of Michigan, Ann Arbor, Michigan 48109.

Antiperovskite materials are intermetallic compounds with perovskite crystal structure (space group Pm3m) but with anion and cation positions interchanged in the unit cell [1]. Similar to oxide-perovskite structure, antiperovskite materials have a variety of physical properties including antiferromagnetism, superconductivity and giant magnetoresistance [2]. There have been very few studies of antiperovskite structure Mn_3GaN in general although it was seen in molecular beam epitaxial growth as a second-phase precipitate when growing MnGaN [3]. Here we discuss the molecular beam epitaxial growth and surface study of Mn_3GaN. In our work, Mn_3GaN is deposited at 250 ± 10 °C onto magnesium oxide (001) substrates with a Mn: Ga: N flux ratio of 3:1:1. The sample surface is continuously monitored throughout the growth using reflection high energy electron diffraction. During the growth, the RHEED pattern was observed to be highly streaky, indicating an atomically smooth surface. The calculated *in-plane* lattice constant based on RHEED is 3.89 ± 0.06 Å. This value is close to the theoretical lattice constant *a* of Mn_3GaN (3.898 Å) [3]. X-ray diffraction confirms the majority 002 peak, and the value calculated is 3.84 ± 0.06 Å which also agrees well with the theoretical value (3.898 Å) [3] and with the experimental reported *c* value (3.881 Å) [2]. Since we did not observe significant second-phase peaks, the phase purity of the sample is quite high. Furthermore, cross-sectional STEM was done to understand the interface and the surface of the film. The plan is to also present *in-situ* scanning tunneling microscopy results for the surfaces of these MBE-grown Mn_3GaN layers.

This work is supported by the U.S. Department of Energy, Office of Basic Energy Sciences, Division of Materials Sciences and Engineering under Award No. DE-FG02-06ER46317.

[1] S. V. Krivovichev, Minerals with antiperovskite structure: A review. Z. Kristallogr. 223, 109–113 (2008).

[2] KH. Kim, KJ. Lee, HS. Kang, FC. Yu, JA. Kim, DJ. Kim, KH. Baik, SH. Yoo, CG. Kim, YS. Kim, "Molecular beam epitaxial growth of GaN and GaMnN using a single precursor," Physica Status Solidi (b) 241(7), 1458 (2004).

[3] E. F. Bertaut, D. Fruchart, J. P. Bouchaud, and R. Fruchart, (1968). Diffraction Neutronique de Mn3GaN. Solid State Commun. 6, 251–256 (1968).

Supplementary Information

Figure 1(a)&(b) left and right panel shows the MgO RHEED patterns along [100] and [110] directions before growth. The half order streaks were initially non observable but later became visible as seen in Fig. 1(c). Streaky patterns show that the grown film is flat and epitaxial.

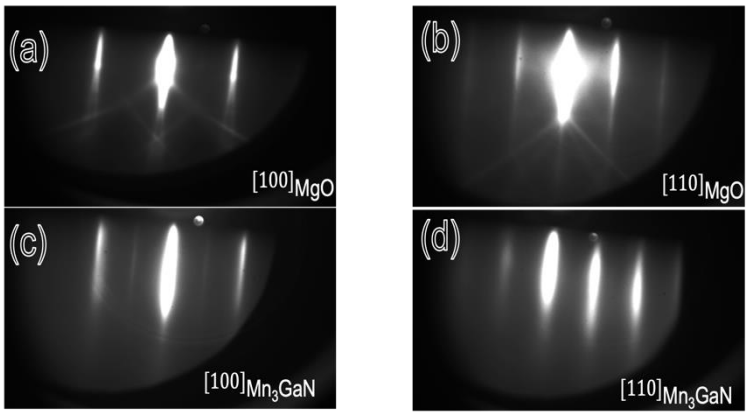

Figure 1. RHEED pattern evolution of Mn_3GaN growth. (a),(b) Representative images showing $[100]_{MgO}$ and $[110]_{MgO}$ azimuths before growth at 250 °C; (c), (d) after 25 minutes of growth showing strong 1st-order streaks and weak 2nd-order streaks along $[100]_{Mn_3GaN}$.

Figure 2 shows the lattice imaging of the Mn_3GaN film. Here we see a clear cubic lattice corresponding to *a*-plane and matching an *a*-plane model. HAADF stem image further confirms the epitaxially smooth and flat surface(bright colored layer).

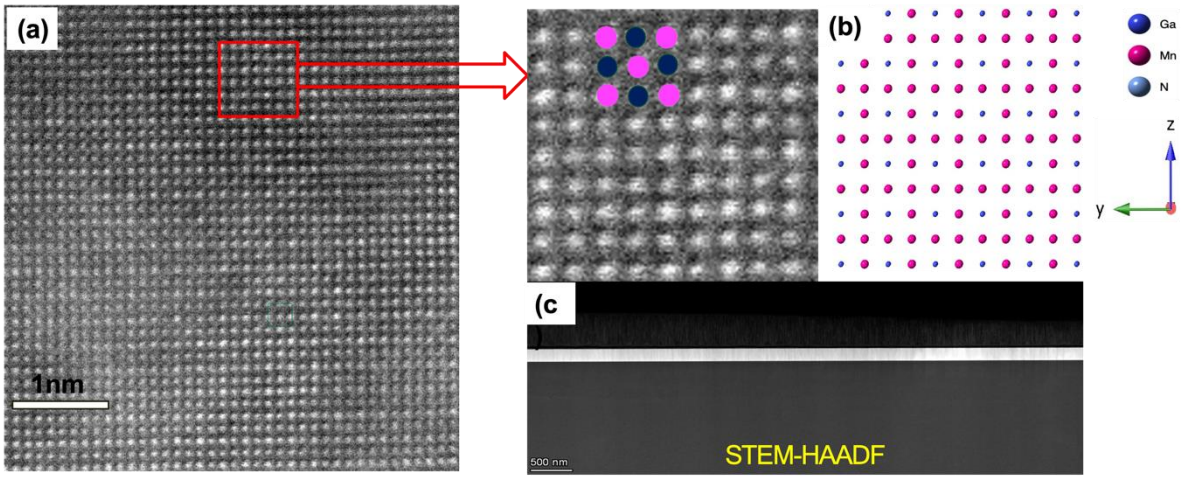

Figure 2. (a) HAADF image of Mn_3GaN Lattice confirming cubic structure. ;(b) STEM model corresponding to the lattice image matching with Mg (purple) and Ga (blue) atoms; (c) Low magnification HAADF-STEM image of the Mn_3GaN film on MgO (001)

Investigation of smooth epitaxial growth of Mn_3Sn films on *c*-plane GaN using molecular beam epitaxy

Sneha Upadhyay [$], ***Hannah Hall*** [$], ***Cherie D'Mello*** [$], ***Juan Carlos Moreno Hernandez*** [#], ***Tyler Erickson*** [$], ***Kai Sun****, ***Gregorio Hernandez Cocoletzi*** [#], ***Noboru Takeuchi*** [%], ***Arthur R. Smith*** [$,+]

[$] *Nanoscale & Quantum Phenomena Institute, Department of Physics and Astronomy, Ohio University, Athens, OH 45701*

** Michigan Center for Materials Characterization, Department of Materials Science and Engineering, The University of Michigan, Ann Arbor, MI 48109*

[#] *Universidad Autónoma de Puebla, Instituto de Física, Apartado Postal J-48, Puebla 72570, Mexico.*

[%] *Centro de Nanociencias y Nanotecnología, Universidad Nacional Autónoma de México, Apartado Postal 14, Código Postal, Ensenada, Baja California 22800, México.*

Recently, Chen *et al.* studied the all-antiferromagnetic tunnel junction consisting of Mn_3Sn / MgO/ Mn_3Sn (011$\underline{1}$), where they observed a tunnel magnetoresistance (TMR) effect at a ratio of 2% at room temperature. [1] Furthermore, Bangar *et al.* reported the epitaxial growth of *c*-plane Mn_3Sn on the Al_2O_3 substrate using a Ru seed layer. They demonstrated a technique of engineering intrinsic spin Hall conductivity in Mn_3Sn by adjusting the Mn composition slightly for functional spintronic devices.[2] These works indicate great potential for kagome antiferromagnetic material, and it is essential to investigate the growth of Mn_3Sn on various substrates. In our previous work, we demonstrated the deposition of Mn_3Sn (0001) on Al_2O_3 (0001) at 524 ± 5°C, which resulted in a 3D island growth. We observed dome-like structures, which may be related to the significant lattice mismatch with sapphire (19%).[3] Subsequently, we began to explore new substrates, and recently, we tried the growth on the MBE-grown N-polar GaN (000$\underline{1}$). The growth was monitored *in-situ* using reflection high energy electron diffraction and measured *ex-situ* using X-ray diffraction, Rutherford backscattering, and atomic force microscopy. The sample grew at 524 ± 5°C for 71 mins, resulting in an epitaxially smooth growth of Mn_3Sn on GaN (000$\underline{1}$). The *in-plane* lattice constants indicate a strain of -2.13 %, while the XRD indicates a 0001 orientation with a strain of -0.53% and an 11$\underline{2}$0 orientation with a strain of + 2.73%. Furthermore, the effect of varying growth temperature and Mn: Sn flux ratio on film orientation and crystallinity will be discussed in detail. We are also planning to begin scanning tunneling microscope experiments.

The authors acknowledge support from the U.S. Department of Energy, Office of Basic Energy Sciences, Division of Materials Sciences and Engineering under Award No. DE-FG02-06ER46317. We acknowledge the financial support of the Nanoscale & Quantum Phenomena Institute.

[1] X. Chen *et al.*, "Octupole–driven magnetoresistance in an antiferromagnetic tunnel junction." Nature **613**, 490 (2023).

[2] H. Bangar *et al.*, "Large Spin Hall Conductivity in Epitaxial thin films of Kagome Antiferromagnet Mn_3Sn at room temperature", Adv. Quantum Technol. **6**, 2200115 (2023).

[3] S. Upadhyay *et al.*, "Exploring the interfacial structure and Crystallinity for Direct Growth of Mn_3Sn (0001) on Sapphire (0001) by Molecular Beam Epitaxy", *Surfaces and Interfaces (accepted).*

[+] Author for correspondence: smitha2@ohio.edu

Supplementary Pages (Optional)

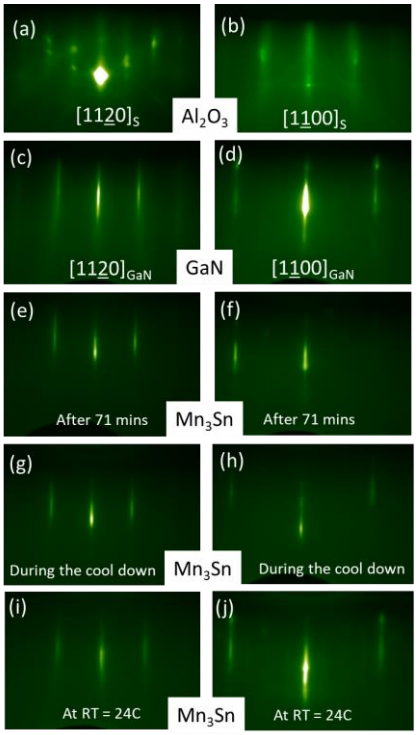

Figure 1: RHEED patterns of GaN (000$\bar{1}$) and growth of Mn_3Sn at 524 ± 5°C. (a-b) annealed Al_2O_3; (c-d) GaN at room temperature (e-f) after 71 mins of Mn_3Sn growth (g-h) Mn_3Sn during the cool down (i-j) Mn_3Sn next day at room temperature.

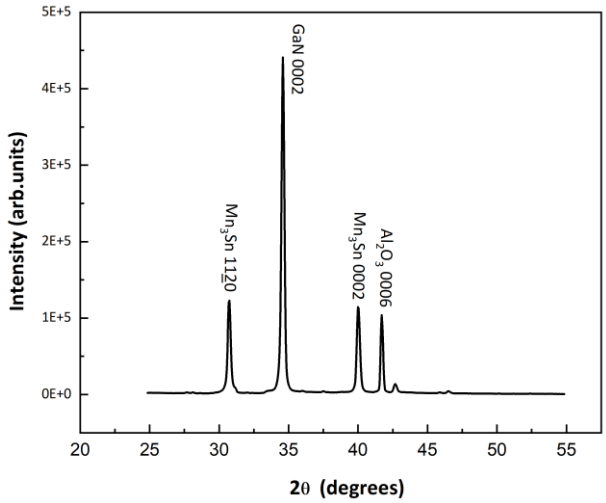

Figure 2: X-ray diffraction of Mn_3Sn/GaN (000$\bar{1}$) / Al_2O_3 (0001) at 524 ± 5°C.

Symmetry constraints on topological invariants

Jing Zhang

Department of Physics and Institute of Advanced Studies, Tsinghua University, Beijing 100084, PRC and Blackett Laboratory, Department of Physics, Imperial College London, Prince Consort Road, London SW7 2BW, UK

Abstract

Classification of topologically trivial/non-trivial crystalline insulators are based on the homology of Berry connection on the Bloch (vector) bundle with the Brillouin zone as the base manifold. Specifically, the trivial phase correspond to zero generalized Berry phase defined as

$$\phi_B = -i \ln \det \left[W(\mathbf{k}_0, C) \right] = -i \sum_n \oint_{\mathbf{k}_0}^{\mathbf{k}_0} \langle \psi_n(\mathbf{k}) \mid \nabla_{\mathbf{k}} \mid \psi_n(\mathbf{k}) \rangle \cdot \mathrm{d}\mathbf{k} \tag{1}$$

where W is the Wilson matrix, $|\psi_n(\mathbf{k})\rangle$ are the energy eigenstate of band n and path C is any closed path in the BZ. Whilst the transformation properties of $|\psi_n(\mathbf{k})\rangle$ may be well defined at given $\mathbf{k}$, it is generally a function of $\mathbf{k}$ and makes symmetry analysis of ϕ_B (path integral in BZ does not form a representation of the space group) difficult. There are symmetry analysis such as symmetry indicator method but they lack the group theoretical justification analogous to selection rules or Wigner-Eckart theorem. In this contribution, it is shown that ϕ_B can be evaluated using the band representation basis under the tight binding model and Stokes theorem.

$$i\phi_B = \sum_n \oint_{\mathbf{k}_0}^{\mathbf{k}_0} \langle \psi_n(\mathbf{k}) \mid \nabla_{\mathbf{k}} \mid \psi_n(\mathbf{k}) \rangle \cdot \mathrm{d}\mathbf{k} = \sum_j \oint_{\mathbf{k}_0}^{\mathbf{k}_0} \langle \phi_j(\mathbf{k}) \mid \nabla_{\mathbf{k}} \mid \phi_j(\mathbf{k}) \rangle \cdot \mathrm{d}\mathbf{k}. \tag{2}$$

where $|\phi_j(\mathbf{k})\rangle$ are the tight binding basis or elementary band representations with Slater-Koster choice of phase. The transformation properties of these EBRs contains no explicit $\mathbf{k}$ dependence and right hand side of Eq.(2) form a representation of the space group (The operation of space group takes the closed path to others in the BZ belonging to a closed set. These set of Berry phases along different paths within the set form the representation). Then symmetry argument may be applied with standard techniques such as selection rules and projection operators. As a closed path in the BZ is frequently not contained in the representation domain, it is important to consider the full group method, often neglected in preference to analysis within the representation domain of the BZ.

The base manifold of BZ are 2-torus (T^2, 2 dimensional lattice, layer group) or 3-torus (T^3, 3-dimensional lattice, space group). It is not simply connected

and one needs to inquivalent un-contractable closed path, as in homotopy analysis involving the fundamental group. The operation of symmetry group naturally takes closed path between such inequivalent set. Symmetry analysis shows the ϕ_B is generally not forbidden by symmetry of layer/space group. However, presence of some symmetry (e.g. inversion) may leads to specific selection rules that forces the Berry phase to be zero.

For a set of physically connected bands with symmetry at high symmetry points identical to direct sum of the EBRs, they have the same transformation properties as the set of EBRs and may be represented as such with appropriate interactions. The same symmetry analysis then may be applied. For close path containing the Γ point, what forms a representation of the group is not necessarily restricted to the whole close path, but half of a close path given that Γ point is invariant. Graphene is used as an example to illustrate both the trivial (sp_2 bands) and non-trivial (p_z band with spin).

The general conclusions are that not all ocuppied EBRs are symmetry forbidden from having non-zero Berry phase and occurrence of trivial phase are the exceptions. The symmetry indicator method at identifying trivial phase may include non-trivial phases.

Epitaxial Kagome Thin Films as a Platform for Topological Flat Bands and Dirac Cones

Shuyu Cheng,[1] M. Nrisimhamurty,[1] Tong Zhou,[2] Núria Bagués,[3,4] Wenyi Zhou,[1] Alexander J. Bishop,[1] Igor Lyalin,[1] Chris Jozwiak,[5] Aaron Bostwick,[5] Eli Rotenberg,[5] David W. McComb,[3,4] Igor Žutić,[2] and Roland K. Kawakami[1]

[1]The Ohio State University, Department of Physics, Columbus, OH, USA

[2]University at Buffalo, Department of Physics, Buffalo, NY, USA

[3]The Ohio State University, Department of Materials Science and Engineering, Columbus, OH, USA

[4]The Ohio State University, Center for Electron Microscopy and Analysis, Columbus, OH, USA

[5]Lawrence Berkeley National Laboratory, Advanced Light Source, Berkeley, CA, USA

Metals consisting of kagome lattices have interesting band structures consisting of topological flat bands and Dirac cones. Systems with flat bands are ideal for studying strongly correlated electronic states and related phenomena due to the smaller bandwidth W compared to the Coulomb repulsion U. Kagome metals such as CoSn have been recognized as promising candidates due to the proximity between the flat bands and the Fermi level. A key next step will be to realize epitaxial kagome thin films with flat bands to enable tuning of the flat bands across the Fermi level via electrostatic gating or strain. Here we report the band structures of epitaxial CoSn thin films grown directly on insulating substrates [1]. Flat bands are observed using synchrotron-based angle-resolved photoemission spectroscopy (ARPES). The band structure is consistent with density functional theory (DFT) calculations, and the transport properties are quantitatively explained by the band structure and semiclassical transport theory. We are also developing kagome metals that have the Dirac cones near the Fermi level, which are interesting for investigating the intrinsic anomalous Hall effect and to potentially realize the quantum anomalous Hall effect at elevated temperatures.

[1] Cheng *et al.,* Nano Letters, 23(15), 7107-7113 (2023).

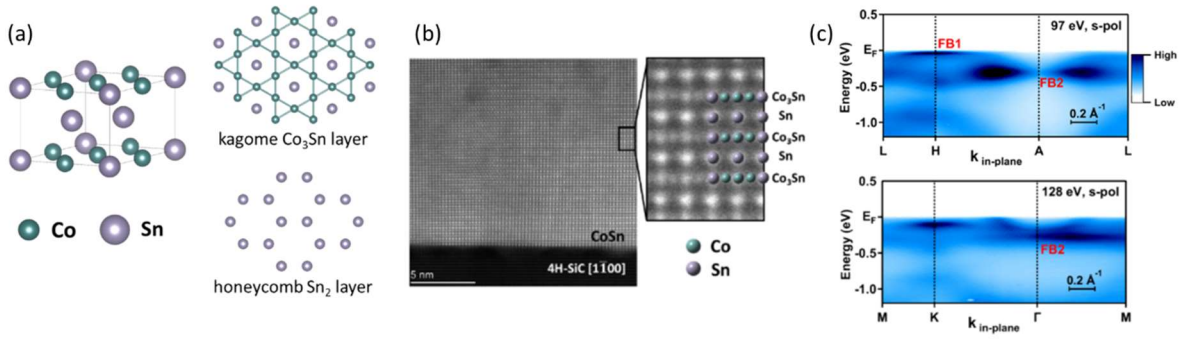

Figure 1. (a) Atomic lattice structure of kagome metal CoSn. (b) Cross-sectional of scanning transmission electron microscopy (STEM) image of CoSn. (c) Angle-resolved photoemission spectroscopy (ARPES) measurements flat bands (FB1, FB2) measured at $k_z = \pi$ (top) and $k_z = 0$ (bottom).

Supplementary Pages

We have nearly completed a study on the epitaxial thin films of kagome metals $TbMn_6Sn_6$ and $ErMn_6Sn_6$. These are members of the RMn_6Sn_6 (R = rare earth) family that has recently been studied in bulk crystals, but to our knowledge, there are no previous reports of thin film growth of these materials.

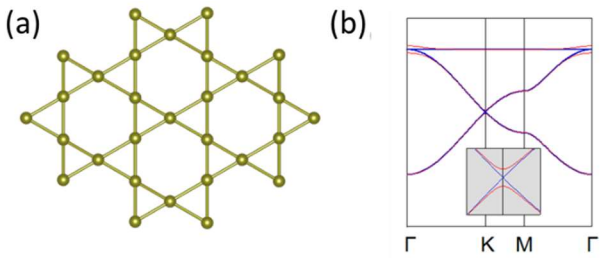

Figure S1. *(a) A schematic drawing of a 2D kagome lattice. (b) Band structure of the 2D kagome lattice calculated by tight-binding model. Red (blue) is with (without) spin-orbit coupling.*

Kagome lattices have garnered substantial interest because their band structure consists of topological flat bands and Dirac cones (Fig. S1). The RMn_6Sn_6 compounds are particularly interesting because the Mn kagome planes occupy their own atomic layers (Fig. S2a), in contrast to other kagome metals such as CoSn which have Sn atomic within the Mn kagome plane. The isolated nature of the Mn kagome planes in RMn_6Sn_6 have less hybridization and energy overlap with other bands in the material. This allows the topological flat bands or Dirac cones to be more isolated in energy, which is important for realizing the quantum anomalous Hall effect (QAHE).

The RHEED patterns (Fig. S2b), XRD and AFM (Fig. S3) are all good. Magnetization measurements show interesting properties (Fig. S4). The $ErMn_6Sn_6$ has an in-plane easy axis for all temperatures. The $TbMn_6Sn_6$ shows strong perpendicular magnetic anisotropy (PMA) at low temperatures and the magnetization transitions to in-plane near room temperature. These are consistent with bulk crystal samples. The perpendicular magnetization of $TbMn_6Sb_6$ is a necessary condition for QAHE, so we are encouraged by these early results.

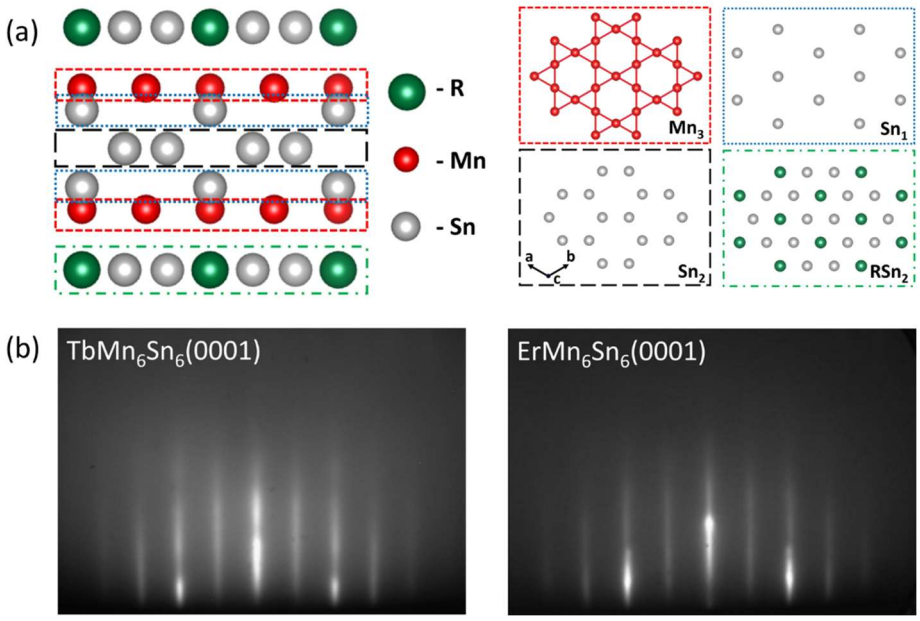

Figure S2. *(a) Atomic lattice of RMn_6Sn_6. (b) RHEED patterns of $TbMn_6Sn_6$ and $ErMn_6Sn_6$.*

Efficient Control of 2D Magnets

Cheng Gong
Department of Electrical and Computer Engineering and Quantum Technology Center,
University of Maryland, College Park
Email: gongc@umd.edu

The emergent two-dimensional (2D) layered magnets [1,2] provide ideal platforms to enable the atomically thin magneto-optical and magnetoelectric devices. Though many have envisioned that 2D magnets should allow efficient control of magnetism by a variety of external stimuli, true breakthroughs are still lacking, with limited proof-of-concept demonstrations reported thus far. There appear to be fundamental obstacles for efficient control, e.g., through electrical and optical means. In this talk I will analyze the challenges and present our theoretical and experimental progress on efficient electrical [3-7] and optical control [8,9] of 2D magnets. Specifically, the results show that the voltage of a few volts can effectively change the magnetic anisotropy of 2D magnets and the laser shinning of tens of uW/um^2 can effectively affect the domain behaviors of 2D magnets. These efficient controls of 2D magnets potentially open up new avenues towards low-power spintronics and photonics.

1. C. Gong et al. *Nature* 546, 265-269 (2017).
2. C. Gong, X. Zhang. *Science* 363, eaav4450 (2019).
3. C. Gong, et al. *Nature Communications* 10, 2657 (2019).
4. S.-J. Gong, et al. *PNAS* 115, 8511 (2018).
5. E.-W. Du, et al. *Nano Letters* 20, 7230 (2020).
6. S. Liang, et al. *Nature Electronics* 6, 199-205 (2023).
7. Q. Wang, et al. *Matter* 5, 4425-4436 (2022).
8. Y. Gong, et al. *npj 2D Materials and Applications* 6, 9 (2022).
9. T. Xie, et al. under review (2023).

Surface-Bulk Difference in van der Waals Magnets

L. Zhao[1,+]

[1] *Department of Physics, University of Michigan, Ann Arbor, MI, USA*

The successful isolation of monolayer to few-layer magnetic atomic crystals from van der Waals (vdW) magnets have opened a new pathway of researching two-dimensional (2D) magnetism [1,2,3]. Over the past half a decade, the vdW and 2D magnet library has been greatly expanded, and new magnetic phenomena have been discovered in the 2D limit. Yet, one key question has been brought up: what is the distinction amongst bulk, surface and 2D magnetism for a vdW magnet? This question is well motivated by the observations of 2D behaviors in 3D vdW magnets, as well as the contrasts between 2D layers and 3D bulk, for systems such as CrI_3, CrSBr, $NiPS_3$, etc.

In this talk, we will show the surface-bulk difference in two archetype vdW magnets, CrI_3 [4] and CrSBr [5]. In CrI_3, it has been thought that the 3D bulk hosts the ferromagnetic (FM) state below T_c = 61K whereas the 2D films realizes the layered antiferromagnetic (AFM) order below T_N = 45K. We will show from our optical magneto-Raman spectroscopy measurements that even in a 3D bulk CrI_3, we capture clear signatures of layered AFM, in addition to the known bulk FM. We attribute the layered AFM signature here to the surface magnetism, which is the same as that of the 2D layers but distinct from that deep in the 3D bulk (Figure 1a). In CrSBr, it has the same layered AFM order in both 3D bulk and 2D layers, but surprisingly with a higher critical temperature in the 2D case. We will show with our nonlinear optical measurements that multiple characteristic temperature scales appear in the 3D bulk CrSBr, including a surface ($T_{surface}$) and a bulk (T_{bulk}) onset temperature between which the surface one is unexpectedly higher than the bulk one (Figure 1b). Our results on these two systems demonstrate that the surface of vdW magnets can well be distinct from their bulk.

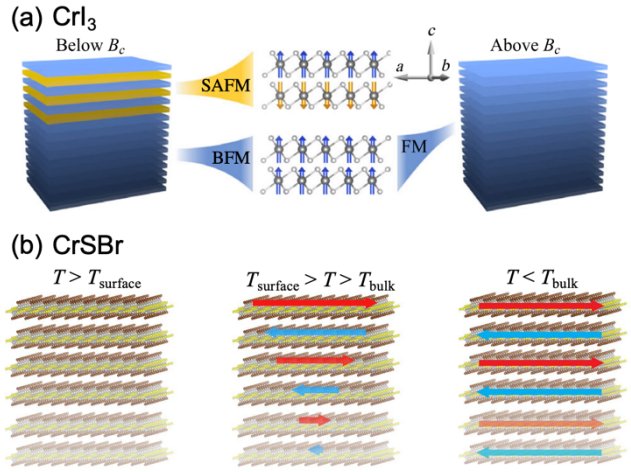

Figure 1 (a) Diagram to show the surface layered antiferromagnetism (SAFM) and bulk ferromagnetism (BFM) in the 3D bulk CrI_3; (b) Diagram to show the separation of surface and bulk magnetic critical temperatures in the 3D bulk CrSBr.

[1] Cheng *et al* Nature 546, 265 (2017)
[2] Huang *et al* Nature 546, 270 (2017)
[3] Wang *et al* ACS Nano, 16, 6960 (2022)
[4] Li *et al* Phys. Rev. X, 10, 011075 (2020)
[5] Guo *et al* arXiv 2309.01047 (2023)

[+] Author for correspondence: lyzhao@umich.edu

Surface investigation of hexagonal non-collinear $D0_{19}$-Mn_3Ga thin film on GaN(0001) substrate

A. Shrestha, A. Abbas, D. C. Ingram, and A. R. Smith[+]
Nanoscale and Quantum Phenomena Institute, Department of Physics and Astronomy
Ohio University, Athens, OH 45701

In recent years, Mn_3Ga has garnered significant attention due to its exotic physical properties and potential applications in spintronic devices [1,2]. One of the most intriguing, yet less explored, phases is the hexagonal antiferromagnetic phase of Mn_3Ga ($D0_{19}$), which exhibits anomalous Hall effect and topological Hall effect in distinct temperature ranges [2]. In this presentation, we will delve into the growth and surface studies of a thin film of $D0_{19}$-Mn_3Ga on a Ga polar- GaN (0001) substrate.

The experiments are carried out in an ultra-high vacuum chamber equipped with a molecular beam epitaxy system and a room-temperature scanning tunneling microscope. Initially, the GaN epilayer is deposited on a GaN (0001) substrate at 700 ºC under gallium-rich conditions, followed by the growth of $D0_{19}$-Mn_3Ga at 250 ºC under manganese-rich conditions. Reflection high-energy electron diffraction is used during growth to monitor the sample, and the *in-plane* lattice constant is evaluated. Various *in-situ* techniques confirm that the grown sample exhibits epitaxial growth. Furthermore, scanning tunneling microscopy image shows the hexagonal atomic arrangements with an average *in-plane* atomic spacing of 5.37 ± 0.05 Å. However, the atomic spacing varies in the local region. The 1 x 1 surface structure of hexagonal $D0_{19}$-Mn_3Ga (a = 5.40 Å [2]) is shown in Fig. 1. Moreover, multiple flat terraces and steps with height of 2.20 Å are observed. The measured step height corresponds to the c/2 value of $D0_{19}$-Mn_3Ga (c = 4.39 Å [2]). The *ex-situ* X-ray diffraction clearly shows the Mn_3Ga 0002 peak, and the calculated d-spacing matched well with the step heights measured by scanning tunneling microscope. These measurements are consistent with the theoretically reported c-value of $D0_{19}$-Mn_3Ga. The concentration of manganese and gallium in the sample is confirmed to be 3.2:1.0 by Rutherford backscattering. Various *in-situ* and *ex-situ* measurements confirm the $D0_{19}$-Mn_3Ga growth. Further work is planned to investigate the non-collinear antiferromagnetism using spin polarized scanning tunneling microscope.

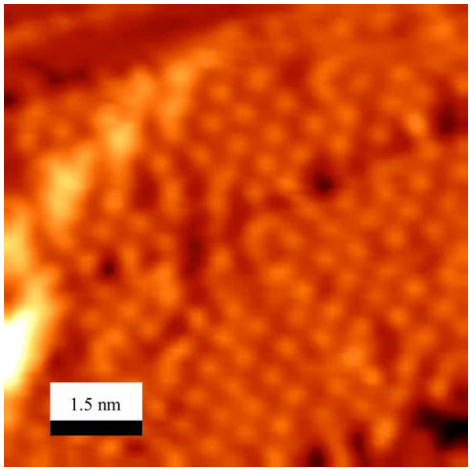

Figure 1: Atomic resolution STM image of $D0_{19}$-Mn_3Ga surface

This work is supported by the U.S. Department of Energy, Office of Basic Energy Sciences, Division of Materials Sciences and Engineering under Award No. DE-FG02-06ER46317.

[1] L. Song, B. Ding, Appl. Phys. Lett. **119**, 152405 (2021).
[2] Z. H. Liu, Scientific Reports **7**, 515 (2017).

[+] Author for correspondence: smitha2@ohio.edu

Supplementary information

The sample was grown using molecular beam epitaxy and monitored *in-situ* using reflection high energy electron diffraction (RHEED). The RHEED patterns of sample and substrate along both directions are shown in Fig. 1. The upper panel represents the GaN(0001) substrate just before the sample growth, while the lower panel represents the Mn_3Ga sample. The grown sample shows a 1 x 1 surface structure on directions. Based on the RHEED patterns, the *in-plane* lattice constant of sample is calculated, which agreed well with the model.

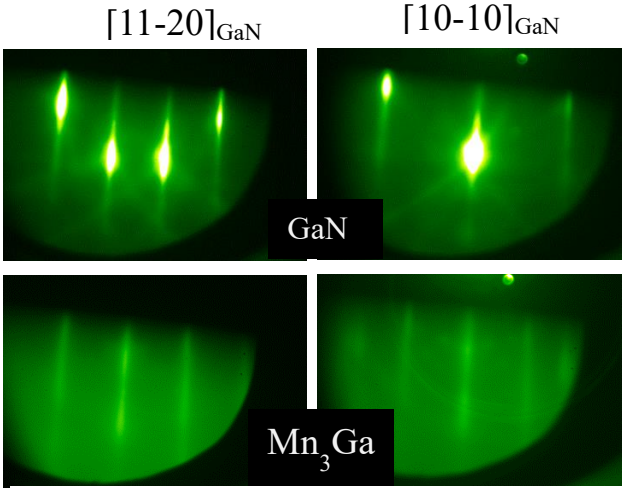

Figure 1: (a) RHEED pattern of GaN substrate (b) RHEED pattern of Mn_3Ga

The STM image in Fig. 2 displays the sample with multiple Mn_3Ga bilayers. The surface appears atomically smooth, featuring multiple terraces and steps. The line profile along line AB gives the height of each step. From the line profile, we identified multiple steps each measuring 2.20 Å in height. The observed height corresponds to a single bilayer height of $D0_{19}$-Mn_3Ga, equivalent to the *c/2* value. XRD measurements also exhibit a similar spacing. Both experimental findings align with the theoretical model.

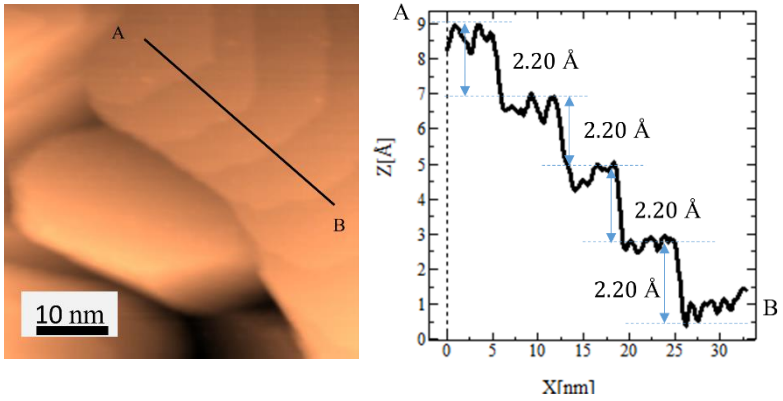

Figure 2: Multiple bi-layer stacking of Mn_3Ga surface.

The Atomic resolution STM image in Fig. 3 reveals mainly three distinct regions: a hexagonal region (HR), a rectangular region (LR), and a stripe region (SR). The HR region corresponds to the hexagonal $D0_{19}$-Mn_3Ga, exhibiting a 1 x 1 surface structure. The observed surface structure aligns well with the RHEED observation. The measured lattice spacing for this region is 5.37 ± 0.05 Å, consistent with the theoretically reported results. In the SR region, wide rows like structures are evident, as depicted in the figure. Meanwhile, the RR region shows the rectangular lattice with dimension of 6.65 ± 0.05 Å x 5.75 ± 0.05 Å. We are actively investigating the origin of such rectangular lattice within our $D0_{19}$-Mn_3Ga sample. Other interesting surface features will be discussed in the meeting.

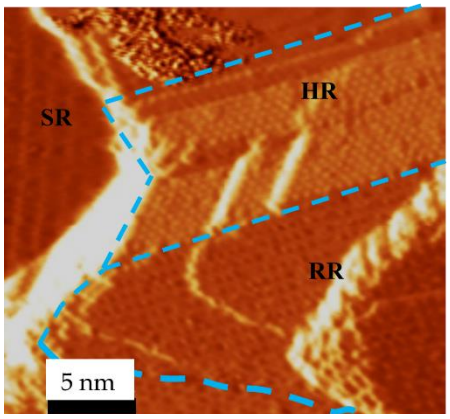

Figure 3: Atomic resolution STM image showing various surface features.

Enhancement of microwave to optical spin-based quantum transduction via a magnon mode

Tharnier O. Puel[1], Adam T. Turflinger[2], Sebastian P. Horvath[2], Jeff D. Thompson[2], Michael E. Flatté[1,3]

[1] *Department of Physics and Astronomy, University of Iowa, IA 52242, USA*
[2] *Department of Electrical Engineering, Princeton University, NJ 08544, USA*
[3] *Department of Applied Physics, Eindhoven University of Technology, Eindhoven, The Netherlands*

The highly localized 4f electrons of rare-earth-doped materials provide a simple atom-like level structure with a spin-photon interface, telecom-wavelength optical transitions, potential for long spin and optical coherence times, and the ability to realize high-density doping. Proposals for microwave to optical quantum transduction using rare-earth ions[PRL113,203601(2014)] rely on spin-flip transitions from microwaves that couple to optical inter-4f transitions. An example is the Er^{3+} ion's transition $|J = 15/2\rangle$ to $|J = 13/2\rangle$ at telecom wavelength. The oscillator strengths ($\boldsymbol{g_b}$) of the microwave excitations of the Er^{3+} are particularly weak leading to poor transduction efficiencies. We describe an approach to dramatically enhance the microwave coupling without diminishing the optical oscillator strength ($\boldsymbol{g_a}$) for Er^{3+} ions. The microwave excitation is coupled to a magnon ($\boldsymbol{g_m}$) of a magnetic material, e.g., yttrium iron garnet (YIG). The Er^{3+} ions are embedded in an insulator and live close to the interface with the magnet. The iron lattice of the YIG will strongly couple to the Er^{3+}. We predict that the microwave-magnon coupling allows higher transduction rates that dramatically exceeds the previous set up.

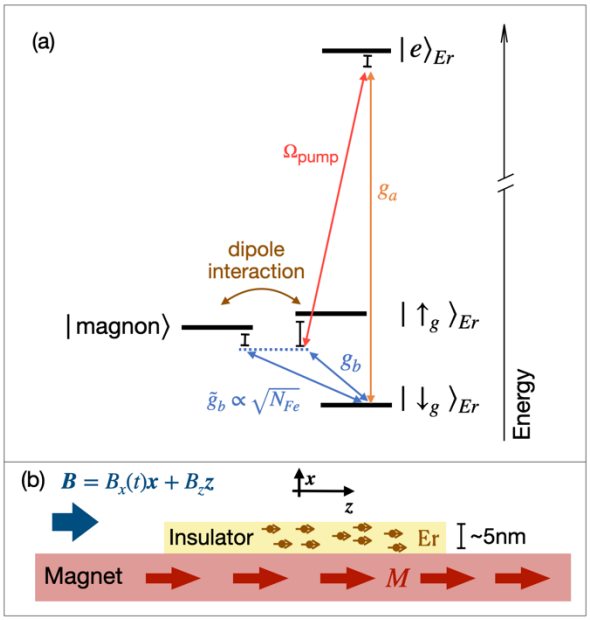

Figure 1. (a) Erbium level structure and its dipole interaction with a magnon mode. Coupling strengths are indicated next to optical ($\boldsymbol{g_a}, \boldsymbol{\Omega_{pump}}$) and microwave transitions ($\boldsymbol{g_b}, \boldsymbol{g_m}$). (b) Erbium ions implanted in an insulator that shares interface with a magnet. The microwave excitation $\boldsymbol{B_x(t)}$ drives the magnon mode that induces erbium spin transitions.

This work is supported by the U. S. Department of Energy, Office of Science: theoretical analysis of magnon mode enhancement of microwave-to-optical transduction by BES Award Number DE-SC0023393, magnon-erbium spin coupling by BES Award Number DE-SC0019250, and material processing and spectroscopy work that supports efficiency estimates by the NQISRC Co-design Center for Quantum Advantage (C2QA) under contract number DE-SC0012704.

[+] Author for correspondence: tharnier-puel@uiowa.edu

Magnetic Modulation and Large Magnetoresistance in Cr_5Te_8

M. Vaninger[1], S. P. Kelley[2], F. Ye[3], X. Zhang[4,5], T.W. Heitmann[1,6], A. Mazza[7], Yew San Hor[8], Ali Sarikhani[8], G. Bian[1], and P.F. Miceli[1]

[1]Department of Physics and Astronomy, University of Missouri, Columbia, MO
[2]Department of Chemistry, University of Missouri, Columbia, MO
[3]Spallation Neutron Source, Oak Ridge National Lab, Oak Ridge, TN
[4]Jiangsu Provincial Key Laboratory of Advanced Photonics and Electronic Materials, School of Electron Science and Engineering, Nanjing University, Nanjing China
[5]Shenzhen Institute for Quantum Science and Engineering, Southern University of Science and Technology, Guangdong, China
[6]University of Missouri Research Reactor (MURR), University of Missouri
[7]MST-16, Los Alamos National Lab, Los Alamos, NM
[8]Department of Physics, Missouri University of Science & Technology, Rolla, MO

Because of the ability to manipulate their structure and properties, metallic 2D van der Waals materials that exhibit ferromagnetism (FM) are of considerable potential interest for spintronics applications. Cr_5Te_8 is such a system whose structure consists of layers of $CrTe_2$ having additional Cr intercalated between the layers. $CrTe_2$ itself is known to be a strong ferromagnet up to room temperature [1]. Cr_5Te_8 is FM below T_{c1}=155K with perpendicular magnetic anisotropy and it exhibits a large (10%) negative magneto-resistance effect above T_{c1} over a narrow temperature range [2].

We have performed neutron diffraction measurements to explore the magnetic behavior in a temperature range above T_{c1} and as a function of applied magnetic field. A modulated antiferromagnetic phase is observed, which has a wavevector perpendicular to the van der Waals layers and a period that is triple the unit cell length. The modulated spin structure is canted with a significant component in the van der Waals layers. The modulation is robust with field applied in-plane but it is quickly destroyed with a field applied perpendicular to the layers. Our magnetic phase diagram shows that the transition from FM to the modulated phase at T_{c1} is strongly first-order with a true FM transition occurring at a higher temperature, T_c=180K. We show that the large magnetoresistance observed in transport arises from the in-plane components of the magnetic moments. Since the spin modulation is controlled at relatively low magnetic field and the intercalated Cr can be tuned, 2D systems such as these have potential for spintronic applications.

Support: NSF-DMR; the University of Missouri Research Reactor. Spallation Neutron Source at Oak Ridge National Lab is supported by the US Department of Energy.

[1] Room-temperature intrinsic ferromagnetism in epitaxial CrTe2 ultrathin films X. Zhang *et al.*, *Nature Communications* **12**:2492 (2021)
[2] Self-Intercalation Tunable Interlayer Exchange Coupling in a Synthetic Van der Waals Antiferromagnet X. Zhang *et al.*, *Advanced Functional Materials* 2202977 (2022)

Supplementary Pages (Optional)

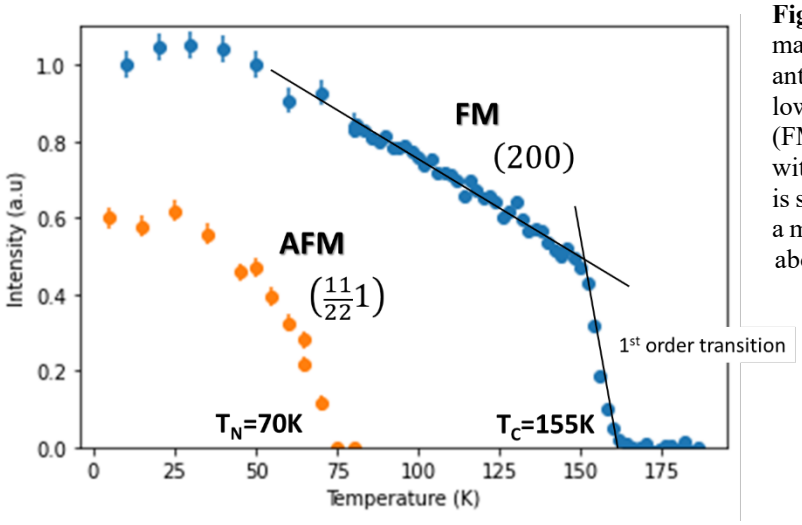

Fig. 1. Neutron Diffraction finds two magnetic phases in Cr_5Te_8, an antiferromagnetic (AFM) phase at low temperature and a ferromagnetic (FM) phase at higher temperature with T_{c1}=155K. The latter transition is strongly first order as it gives rise to a magnetically modulated AFM phase above T_{c1}.

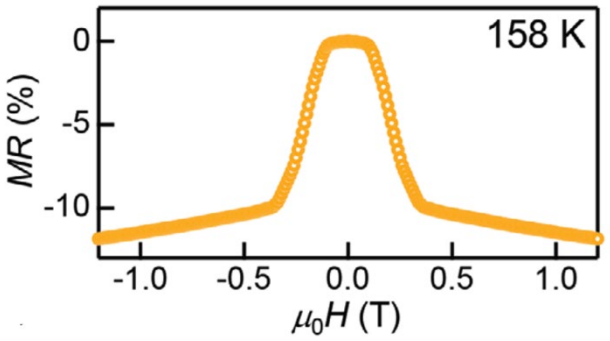

Fig. 2(a). A large negative magnetoresistance is observed in Cr_5Te_8. X. Q. Zhang et al., Adv. Funct. Mater. 2202977 (2022).

Fig. 2(b). The large magneto resistance exists above the FM transition temperature over a narrow (~30K) temperature range.

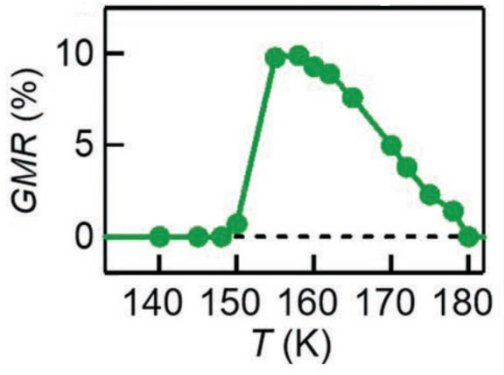

Development of Surface Chemistry on-Top of Organic Semiconductor Thin Films to Improve Optoelectronic Devices

J. W. Ciszek[+]
Loyola University Chicago

Organic devices (OLED, OFETs, OSCs) are commonly configured such that a metal contact must be deposited on top of the organic semiconductor. These interfaces often suffer from numerous flaws including poor adhesion, metal penetration, poor surface wetting (discontinuous films), and significant charge injection barriers. We feel that the ability to selectively change the surface of the organic layer via chemistry would allow for improved interactions with the deposited metal and, in-turn, improve device performance. Vast literature shows monolayers (deposited on top of gold, silicon, etc.) can address many of these issues when the system is reversed (organic on metal), but the methodology for installing them is inapplicable to organic thin-films. This points to an obvious need for controllable surface chemistry on top of the organic semiconductor.

We have developed click-like" Diels-Alder chemistry that allows prototypical OFET films (tetracene, pentacene, rubrene) to be appended with a variety of small molecules to form an interfacial layer only ~1 nm thick. The reacted surface is highly tailorable with dozens of combinations explored for a variety of application. This basic approach is presented in detail. This work then summarizes many of the expected and unexpected deviations which occur due to the very unusual nature of the organic surface, namely its high anisotropy, recessed reaction loci, and weakly bound molecular units. Concluding the fundamental components, we highlight some of our recent work in generating analogous chemistry on OLED electron transport layers, specifically TPBi.

This work concludes by highlighting many interfacial components the chemistry aims to improve, focusing primarily on the morphological and mechanical structure of applied metal top contact. Specifically, we examine how the various functional groups improve surface wetting of the metal, film continuity, adhesion in flexible contacts, metal penetration, and sheet resistance.

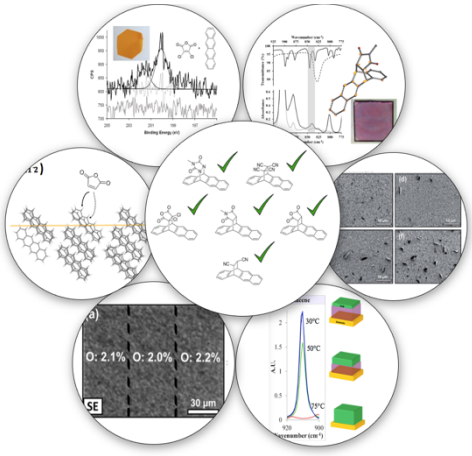

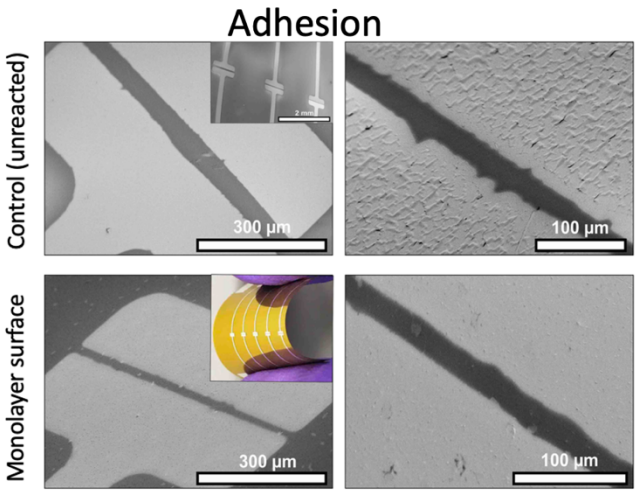

[+] Author for correspondence: jciszek@luc.edu

Supplementary Pages

First, I just want to make sure the problems we aim to solve are clear. An additional image showing the prominence of the metal on organic interface (green in figure) is usually helpful in that regards.

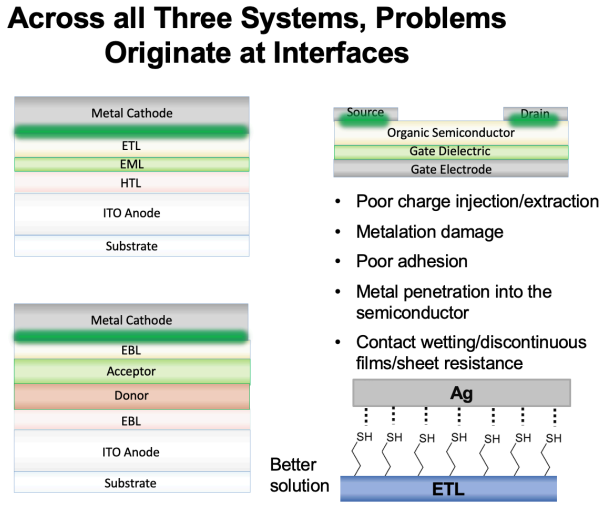

Overall, I try to highlight some of the more interesting aspects of the chemistry. This is, afterall, a very different approach to improving this interface. As the same time I understand that this audience is more interested in the application. With the latter in mind, there is an emphasis on the range of molecules and thin-films, monolayer characteristics, the application processes and limitations. An example figure on the novelty is shown below. Here a crystal of tetracene has completely different reactivity (as shown by the Cl 2p XPS signal) on the two faces, which can be justified based on the molecular packing at the surface of the crystal

Highlighting some of the materials from the application side, reaction cause dramatically changes to the metal wetting and lesser changes to the degree of penetration. Film continuity unsurprisingly improves and sheet resistance drops appreciably.

Most of the images have been removed due to the restrictive file size…..

Characterizing Nanopattern Formation of Polymer Thin Films on Silicon Substrates with Ion Beam Sputtering+

Jocelyn Zhang[1,4], Grace Pettis[2,3], Benli Jiang[1], Neil Baker[3], Eda Guney[5], Gözde Ozaydin Ince[5], Karl F. Ludwig Jr[1,3]

[1]Division of Materials Science and Engineering, Boston University, MA, [2]Oregon State University, OR, [3]Department of Physics, Boston University, MA, [4]Del Norte High School, San Diego, CA, [5]Faculty of Engineering and Natural Sciences, Sabanci University, Turkey

Surface nano-patterns formed by ion beam sputtering (IBS) have been reported by many research groups with most focus on semiconductor and metal materials [1]. However, limited study has been conducted on polymer nanopatterning introduced by IBS [2]. This study aims to understand polymer film wrinkling in relation to ion beams and humidity conditions, which could potentially introduce effective methods of tuning chemical and physical characteristics of polymer film surfaces. Poly(4-Vinylpyridine) (4-VP) and Polystyrene (PS) polymer thin films on silicon substrates were sputtered with Ar^+ ions under ultra-high vacuum (UHV) and then placed in either humid or dry conditions. The results show that wrinkling patterns are formed in 4-VP film after sputtering at 2 keV and consecutive humidification, but no wrinkling patterns are observed in PS under the same condition. The wrinkling amplitude of 4-VP films increases over time under humidity. Areas of lower ion flux have less order and higher amplitude wrinkling in 4-VP. Increasing film thickness increases wrinkle wavelength and decreases the order in the wrinkles. It is also found that the surface contact angle with water increased on both 4-VP and PS after ion beam sputtering, presumably due to increased roughness.

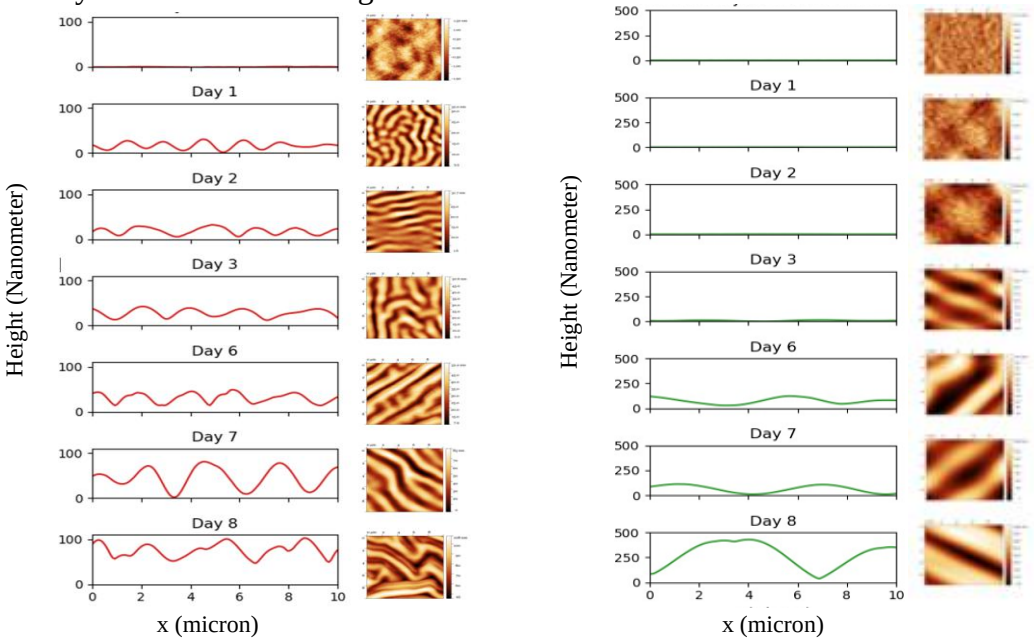

(a) 100nm Thick 4-VP Film (b) 250nm Thick 4-VP Film

Figure 1. AFM topographs showing evolution of sputtered 4-VP film wrinkling under humidity.

[1] R. Cuerno, and J.-S. Kim, 2020, J. 2020, Appl. Phys. 128, 180902

[2] Goyal M, et al, 2016, J. Appl. Phys. 119, 115303

Supplementary Information

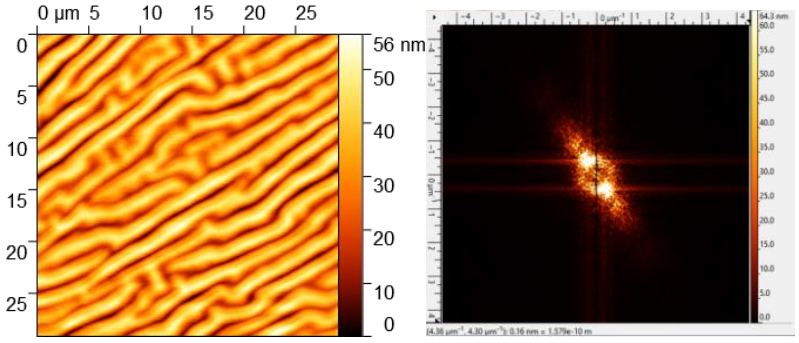

(a) AFM image (left) and 2-D FFT image (right) from 100nm thick 4-VP film.

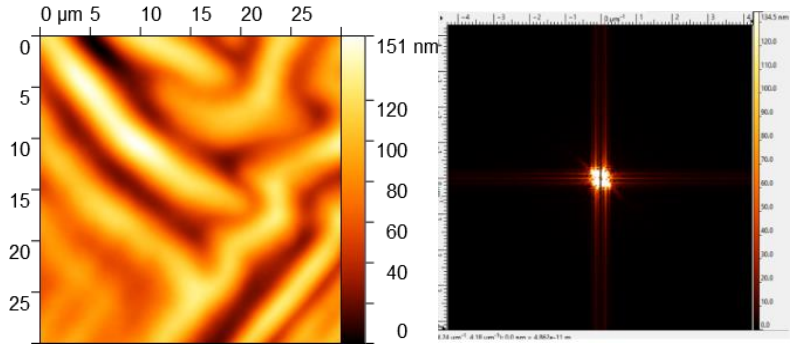

(b) AFM image (left) and 2-D FFT image (right) from 250nm thick 4-VP film.

Fig. 2 Comparison of AFM topographs and 2-D Fast Fourier Transform (FFT) from 4-VP films after day 7 under humidity

+ The project was partly supported by NSF-2117509 and NSF-REU 2244795

Functionalizing Organic Semiconductors with Dipole Monolayers

Matthew C. Williams, Feifei Li, Jordan A. MacQueen, Demetra Z. Adrahtas, Jacob W. Ciszek*

 # Department of Chemistry and Biochemistry, Loyola University Chicago, 1032 West Sheridan Road, Chicago, Illinois 60660, USA.

This work seeks to improve OFETs performance via the addition of a chemisorbed monolayer on top of the organic material to address various issues such as contact resistance and charge trapping. The monolayer is made possible via site-specific Diel-Alder chemistry which only reacts with the semiconductor. By installing specific functional groups to the surface, the aforementioned issues can be eliminated, resulting in improved charge injection and/or charge transport in organic material.

We focused on the addition of monolayers which contain significant electronic charge separation (or molecular dipole) within their structure. This feature can act as a potential step, shift the mean energy in gaps, and/or align energy levels between materials. We first utilize the chemistry to selectively append dipole-containing molecules to trap states at grain boundaries for polycrystalline OFETs in order to shift the mean energy within the grain boundary and improve device performance. Grain boundaries are unavoidable flaws inherent to the materials, and the ability to address trap states would be a powerful way to address these flaws post-fabrication. This performance improvement is exemplified in conductance measurements with two orders of magnitude increases, improved threshold voltages, and doubling of mobility.

Additionally, we can optimize the surface potential of thin films by systematically varying similar dipole-containing monolayers. A linear relationship between dipole strength and surface potential shift is seen, as predicted by the Helmholtz equation. The achieved potential adjustments are attributed to the monolayer and result in a high degree of tunability of surface potential. With the capability to shift potential up to ~800mV, reducing electron charge injection barriers is hypothetically feasible. The challenges arising in conductance measurements are discussed.

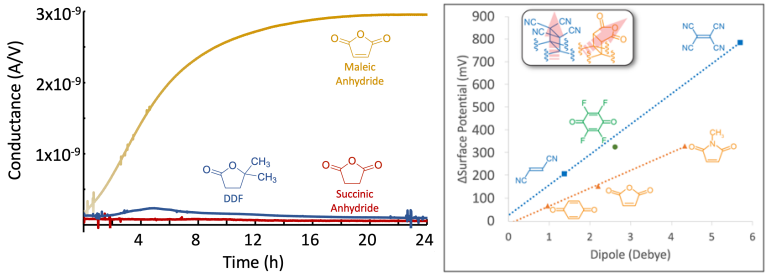

Figure 1. (Left) Conductance of pentacene reacted with maleic anhydride for 8 h as a function of time measured at 0.2 V. The controls are succinic anhydride (red) and DDF (blue). The relationship between dipole strength and the resulting surface potential is characterized by the bond dipole angle (right).

Supplemental Information

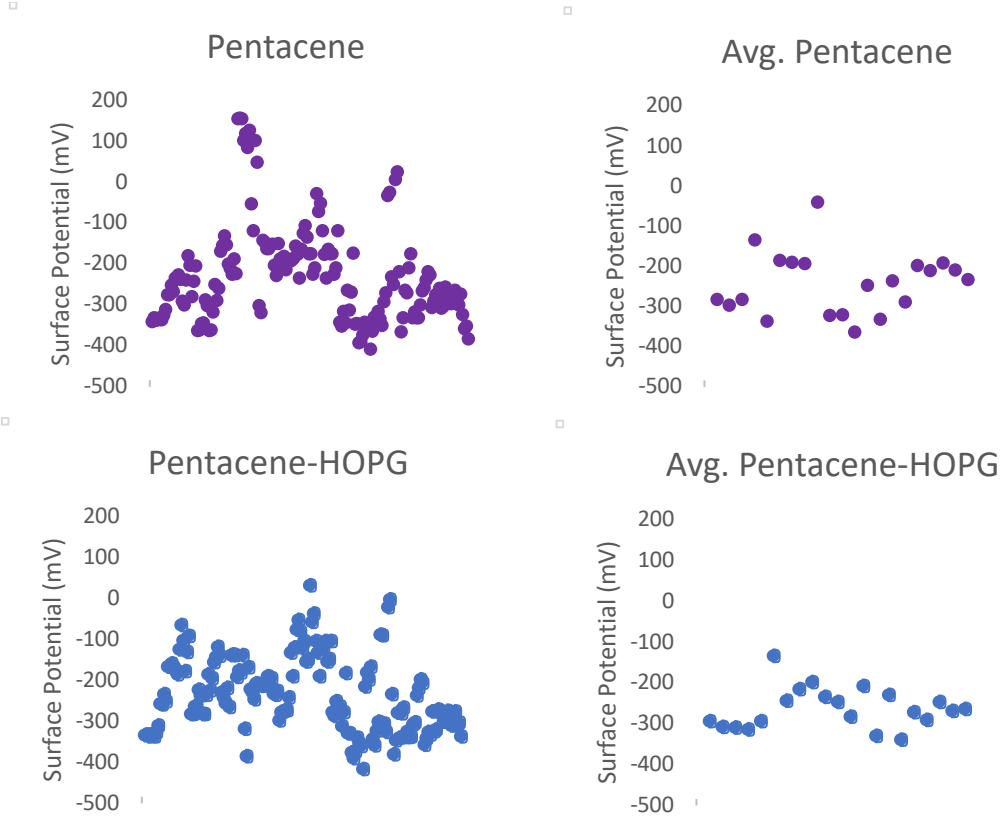

Figure S1. (a) Individual pentacene surface potential measurements and (b) surface potentials averaged by individual organic depositions. (c) Individual pentacene surface potential measurements once referenced to highly oriented pyrolytic graphite and (d) surface potentials averaged by individual organic depositions referenced to highly oriented pyrolytic graphite.

Rare Earth Doped Oxide Thin Films on Silicon for Chip Scale Quantum Emitters and Memories

G. Grant[1], C. Ji[1], I. Masiulionis[1], S. Seth[1], J. Zhang[2], S. Chattaraj[2], J. G. Wen[2], M. K. Singh[1,2], A. Dibos[3], D. D. Awschalom[1,3], S. Guha[1,3,+]

[1] *Pritzker School of Molecular Engineering, University of Chicago, 5640 S Ellis Ave, Chicago, IL 60637*

[2] *memQ, 5214 S Lake Park Ave, Chicago, IL 60615, IL*

[3] *Argonne National Laboratory, 9700 S Cass Ave, Lemont, IL 60439*

Quantum memories are an enabling technology for long distance repeater based quantum communications via optical fibers. Embedded within a host dielectric, the Er ion, with its 1.5 μm 4f-4f optical transition and its expected long spin coherence times, presents a convenient solid-state spin-optical interface that is telecom wavelength compatible for such quantum memory applications. Furthermore, it is desirable that such memories be scalable and compatible with silicon electronics for large scale deployment. Consequently, we have been exploring the properties of Er doped (few to ~100 ppm) dielectric oxide thin films grown on silicon substrates through detailed microstructural, growth and optical studies. Those oxides are also judiciously chosen to have low nuclear spin noise in the host to foster long Er electron spin coherence for memory applications. In these studies, using Er doped TiO_2, Y_2O_3, and CeO_2 as epitaxial and polycrystalline thin film hosts, and careful correlations of electron microscopy and X-ray diffraction based microstructural studies with optical properties, we find that while extended defect densities do not appear to have a significant effect upon the inhomogeneous linewidths, the Er doping levels, proximity of surfaces, the substrate interface, and film thickness have strong effects upon the optical properties including spectral diffusion and optical lifetime besides inhomogeneous linewidth, all critical for memory applications. We will discuss these results and the models of interaction that arise from these results. For the case of epitaxial CeO_2 on Si(111) we measure a narrow homogeneouslinewidth of 440 kHz with an optical coherence time of 0.72 μs at 3.6 K when studying the Z_1-Y_1 optical transition near 1530 nm at ~3.5K, along with an inhomogeneous linewidth of 10 GHz, an optical excited state lifetime of 3.5 ms. Using Er doped TiO_2 films on silicon grown via both molecular beam deposition as well as atomic layer deposition (where we had to develop mechanisms of ppm level doping of Er), we further show that such structures can be processed into good quality factor Si nanophotonic cavity devices and demonstrate a large Purcell enhancement (~ 300) of their optical lifetime leading to higher emission rates. These results indicate the significant promise of Er doped thin films as silicon compatible qubit devices for optical quantum memory and emitter applications. We will discuss these results with a focus on the materials science engineering aspects of this work.

[+] Author for correspondence: sguha@anl.gov

Suplementary Pages (Optional)

More optional text and figures may be submitted on up to two supplemental pages; however, please note that these pages will not be included in the online technical program book. Therefore please do not reference any text or figures from these pages on page one.

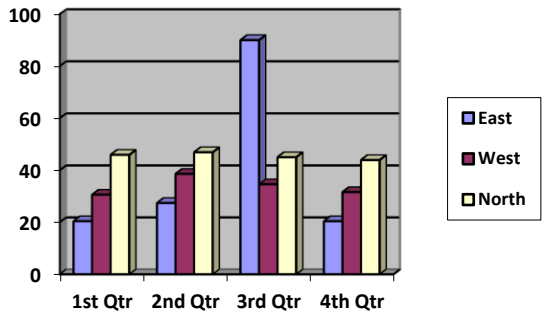

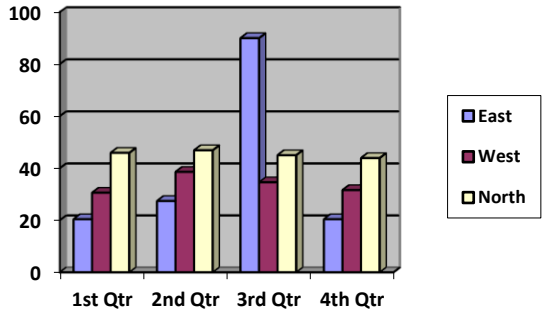

Erbium sites in Silicon for Quantum Information Processing

Sven Rogge*
Centre of Excellence for Quantum Computation and Communication Technology
School of Physics, University of New South Wales, Sydney, NSW 2052, Australia

Rare-earth ions incorporated in several solid-state hosts were shown to exhibit low homogeneous broadening and long spin coherence at cryogenic temperatures making them a promising candidate for quantum applications, such as optical quantum memories, optical-microwave transductions, and quantum communication. However, long electron spin coherence has not been demonstrated in Si, a leading material platform for electronic and photonic applications. Here, we present the first demonstration of Er sites in semiconductor (Si) with a millisecond electron spin coherence time, optical homogeneous linewidths below 100 kHz, spin and optical inhomogeneous broadening approaching 100 kHz and 100 MHz, correspondingly. Er properties were measured using photoluminescence excitation spectroscopy within a nuclear spin-free silicon crystal (<0.01% ^{29}Si) doped at 10^{16} cm^{-3} Er level. Er homogeneous linewidth and spin coherence were addressed using optical comb-based spectral hole burning and optically detected magnetic resonance. To enhance Er emission collection efficiency, samples were directly positioned on top of dedicatedly fabricated superconducting single photon detectors and resonantly excited using fiber optics. Measurements in naturally abundant Si revealed that the Er electron spin coupling to ^{29}Si nuclear spins significantly shortens Er spin coherence times. Long spin coherence time and narrow optical linewidth show that Er in ^{28}Si is an excellent candidate for future quantum information and communication applications.

* Author for correspondence: s.rogge@unsw.edu.au

Emergent Phenomena at Ferroelectric/van der Waals Heterointerfaces

Xia Hong[1]

[1] *Department of Physics and Astronomy & Nebraska Center for Materials and Nanoscience, University of Nebraska-Lincoln, Lincoln, NE, USA*

The heterointerfaces between ferroelectrics and two-dimensional (2D) van der Waals materials present a versatile platform for achieving novel interfacial coupling, nonvolatile field effect control, and nanoscale programmable functionalities. In this talk, I will discuss a range of emergent phenomena in ferroelectric/vdW heterostructures mediated by interfacial coupling of charge, lattice, and polar symmetry. By combining polarization doping with nanoscale domain patterning in a ferroelectric polymer P(VDF-TrFE) top-gate, we create directional conducting paths in an insulating 2D channel, which reveals highly anisotropic conductivity in monolayer (1L) to 4-layer 1T'-ReS_2 between the directions along and perpendicular to the Re-chain (Fig. 1a) [1]. The interface-epitaxy between P(VDF-TrFE) and ReS_2 leads to large scale P(VDF-TrFE) thin films composed of highly ordered, close-packed, 10 and 35 nm wide crystalline nanowires (Fig. 1b) [2]. We observe enhanced polar alignment, piezoelectricity, and Curie temperature in thin $CuInP_2S_6$ (CIPS) flakes prepared on ferroelectric oxide $PbZr_{0.2}Ti_{0.8}O_3$ (PZT) (Fig. 1c), which can be attributed to the interfacial strain imposed by PZT [3]. An unconventional filtering effect of second harmonic generation (SHG) signal is enabled by the polar coupling of 1L MoS_2 with either the polar domain or the chiral dipole rotation at the domain wall surface in PZT thin films (Fig. 1d) or free-standing membranes (Fig. 1e) [4,5]. Our study showcases the rich research opportunities offered by integrating ferroelectrics with 2D materials.

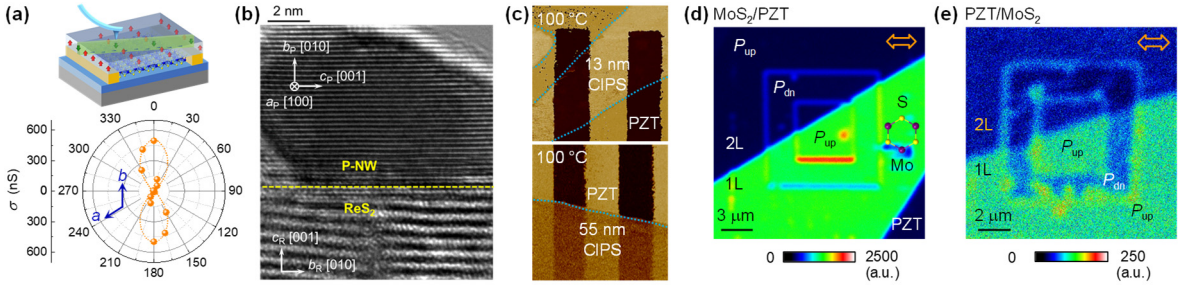

Figure 1 (a) Directional conducting nanowires defined by P(VDF-TrFE) top-gate reveals strong transport anisotropy in 4-layer ReS_2 [1]. (b) HRTEM image of epitaxial interface between P(VDF-TrFE) nanowire and ReS_2 [2]. (c) PFM images show T_C of 13 nm (55 nm) CIPS on PZT is above (below) 100 °C [3]. (d-e) SHG mapping of 1L MoS_2 on PZT thin film (d) and PZT membrane on 1L MoS_2 (e) [5], with PZT patterned into polarization up (P_{up}) and down (P_{dn}) domains.

[1] D. Li *et al.*, Phys. Rev. Lett. **127**,136803 (2021).
[2] D. Li *et al.*, Adv. Mater. **33**, 2100214 (2021).
[3] K. Wang *et al.*, ACS Nano (2023). DOI: 10.1021/acsnano.3c03567
[4] D. Li *et al.*, Nat. Commun. **11**, 1422 (2020).
[5] D. Li *et al.*, Adv. Mater. **35**, 2208825 (2023).

+ Author for correspondence: xia.hong@unl.edu

Impact of High-Power Impulse Magnetron Sputtering Pulse Width on the Nucleation, Crystallization, Microstructure, and Ferroelectric Properties of Hafnium Oxide Thin Films

Samantha T. Jaszewski[1, *], Shelby S. Fields[2], Ching-Chang Chung[3], Jacob L. Jones[3], Keithen G. Orson[2], Petra Reinke[2], and Jon F. Ihlefeld[2,4]

[1] Sandia National Laboratories, Albuquerque, New Mexico 87123, USA
[2]Department of Materials Science and Engineering, University of Virginia, Charlottesville, Virginia 22904, USA
[3]Department of Materials Science and Engineering, North Carolina State University, Raleigh, North Carolina 27695, USA
[4]Charles L. Brown Department of Electrical and Computer Engineering, University of Virginia, Charlottesville, Virginia 22904, USA

The impact of the high-power impulse magnetron sputtering (HiPIMS) pulse width on the crystallization, microstructure, and ferroelectric properties of undoped HfO_2 films is reported. HfO_2 films were sputtered from a Hf target in an Ar/O_2 atmosphere, varying the instantaneous power density by changing the HiPIMS pulse width with fixed time averaged power and pulse frequency. The pulse width is shown to affect the ion-to-neutral ratio in the depositing species with the shortest pulse durations leading to the highest ion fraction, as shown in Figure 1. *In-situ* X-ray diffraction measurements during crystallization demonstrate that the HiPIMS pulse width impacts nucleation and phase formation, with an intermediate pulse width of 110 µs stabilizing the ferroelectric phase over the widest temperature range. Although the pulse width impacts the grain size with the lowest pulse width resulting in the largest grain size (Figure 2), grain size does not strongly correlate with phase content or ferroelectric behavior in these films. These results suggest that precise control over the energetics of the depositing species may be beneficial for stabilizing the ferroelectric phase in this material.

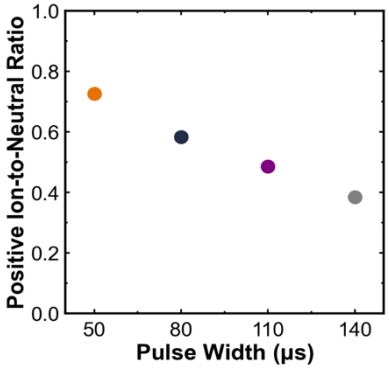

Figure 1: Positive ion-to-neutral ratio calculated from the deposition rates of positive ions + neutrals to neutrals alone.

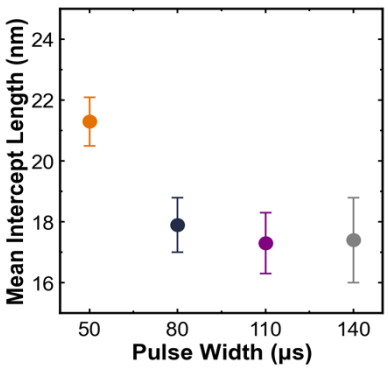

Figure 2: Average lateral grain size calculated using the line-intercept method on the AFM images with error bars representing 95% confidence intervals.

[+] Author for correspondence: stj6ze@virginia.edu

Fabrication and Gamma Radiation Effects on Endurance of Ferroelectric Hafnium Zirconium Oxide Capacitors

M. David Henry[1], Megan Lenox[2], Andre Hillsman[4], Samantha T. Jaszewski[1], Giovanni Esteves[1], Jacob Jones[4], Jon F. Ihlefeld[2, 3]

1 MESA Fabrication Facility, Sandia National Laboratories, Albuquerque, NM 87185, USA

2 Department of Materials Science and Engineering, University of Virginia, Charlottesville, VA 22904, USA

3 Charles L. Brown Department of Electrical and Computer Engineering, University of Virginia, Charlottesville, VA 22904, USA

4Department of Material Science and Engineering, North Carolina State University, Raleigh, NC 27606, USA

Ferroelectric hafnium zirconium oxide (HZO) is attracting significant interest in the semiconductor microelectronics industry with attributes including coercive voltages compatible with CMOS, retention of memory states after power down and reasonable polarizations achieved with films 8 to 15 nm thick. An immediate application of the HZO capacitors include non-volatile memory (NVM) with insertions in the back end of line (BEOL) fabrication. Although devices such as ferroelectric capacitors are most applicable for FeRAM integrations, subtle details in their fabrication including the electrodes used and thickness which can have impact in the device performance metrics.

This work investigates electrode configurations, ferroelectric thickness and anneals utilized in BEOL processes including W and TiN for effects on endurance and polarization. Insertion of thin linear dielectrics, 1 nm of alumina on the bottom electrode, is also investigated to determine properties impactful to FeRAM circuit design. To determine the stability of the film, device polarization and endurance was measured after 5 MRad of Co^{60} gamma cell irradiation over differing voltage rails and cycling frequencies. This work extends the knowledge base of ferroelectric HZO with radiation effects for non volatile memory applications in CMOS.

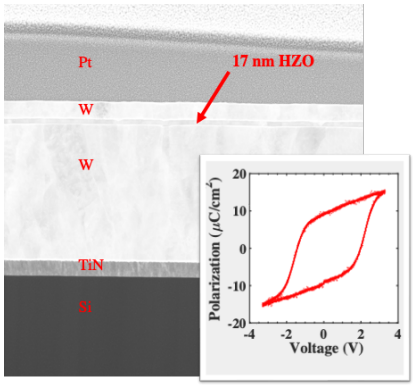

Figure 1. STEM of 17 nm HZO with W electrodes. Inset: Polarization loops of MFM capacitors.

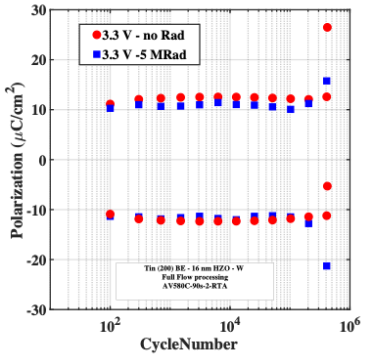

Figure 2. Endurance of 17 nm HZO with TiN and W electrodes before and after 5 MRad gamma radiation.

+ Author for correspondence: mdhenry@sandia.gov

This work was supported by the Laboratory Directed Research and Development program at Sandia National Laboratories, a multimission laboratory managed and operated by National Technology and Engineering Solutions of Sandia LLC, a wholly owned subsidiary of Honeywell International Inc. for the U.S. Department of Energy's National Nuclear Security Administration under contract DE-NA0003525.

Design of Memristive Devices Towards Neuromorphic Computing

Sundar Kunwar,[1] Pinku Roy,[1] Nicholas Cucciniello,[1] Quanxi Jia,[2] Haiyan Wang,[3] Judith L. MacManus-Driscoll,[4] and Aiping Chen,[1,+]

[1] *Center for Integrated Nanotechnologies (CINT), Los Alamos National Laboratory, Los Alamos, NM 87545, USA*
[2] *Department of Materials Design and Innovation, University at Buffalo - The State University of New York, Buffalo, NY 14260, USA*
[3]*School of Materials Engineering, Department Electrical and Computer Engineering, Purdue University, West Lafayette, IN 47907, USA*
[4] *Department of Materials Science & Metallurgy, University of Cambridge, 27 Charles Babbage Road, Cambridge, CB3 0FS, UK*

Current digital computing based on Von Neumann architecture suffers from several key bottleneck including von Neumann bottleneck, Moore's law, and the breakdown of Dennard scaling. Developing new computing platforms provide solutions towards Beyond Moore's computing. Recently, emergent devices such as memristive switching devices have been used to emulate some brain functions including synaptic behavior and neuronal behavior and therefore they have been proposed for developing low-power neuromorphic computing. Oxide-based memristive devices with excellent scalability have the potential to revolutionize not only the field of information storage but also neuromorphic computing.

In this talk, I will first discuss some basics of the brain, brain-inspired neuromorphic computing and artificial intelligence. In the second part of my talk, I will then discuss the roles of defects and interfaces on switching behavior in different types of memristive devices and their impacts on neuromorphic computing. Material systems have profound effects on switching behavior. For example, ferroelectric and non-ferroelectric systems show completely different switching behavior [1-2]. Defects also dominate the switching behavior. Figure 1 compared switching behavior in a variety of materials with different type of defects. Among different types of switching, filament-type switching and interface-type switching are two most distinct switching modes. I will focus on a specific interface-type switching we observed in Au/Nb:$SrTiO_3$ system [3]. It shows the switching is controlled by protons in the environment. We also explored the applications of such systems for neuromorphic computing applications [4].

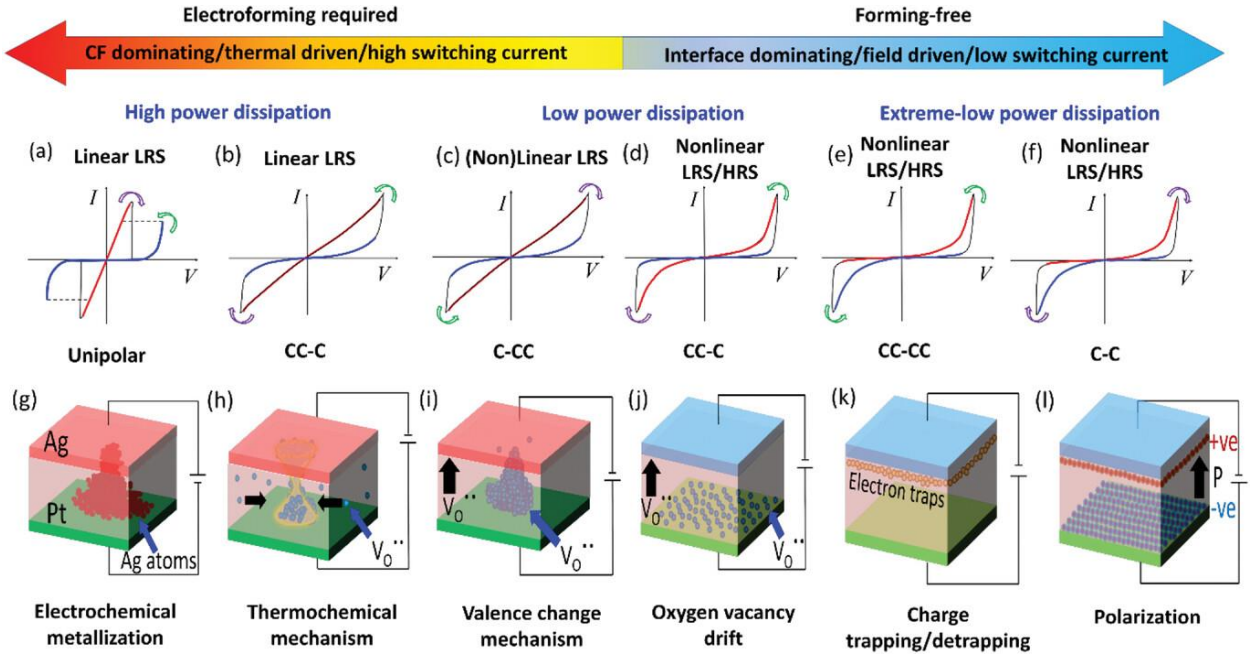

Figure 1. Schematic illustration of different types of resistive switching mechanisms observed in memristors using oxide materials as RS layers. From left (a) to right (f) shows filament-type and interface-type switching with different types of *I*–*V* characteristics along with the possible switching mechanisms (g-l).

[1] P. Roy, S. Kunwar, D. Zhang, D. Chen, Z. Corey, B. X. Rutherford, H. Wang, J. L. MacManus-Driscoll, Q. Jia, A. Chen, Adv. Electron. Mater., **8**, 2101392, (2022).
[2] A. P. Chen, W. R. Zhang, L. R. Dedon, D. Chen, F. Khatkhatay, J. L. MacManus-Driscoll, H. Y. Wang, D. Yarotski, J. Chen, X. S. Gao, L. W. Martin, A. Roelofs, Q. X. Jia, Adv. Funct. Mater., **30**, 2000664, (2020).
[3] S. Kunwar, C. B. Somodi, R. A. Lalk, B. X. Rutherford, Z. Corey, P. Roy, D. Zhang, M. Hellenbrand, M. Xiao, J. L. MacManus-Driscoll, Q. X. Jia, H. Y. Wang, J. J. Yang, W. Y. Nie, A. P. Chen, Adv. Electron. Mater., **9**, 2200816, (2023).
[4] S. Kunwar, Z. Jernigan, Z. Hughes, C. Somodi, M. D. Saccone, F. Caravelli, P. Roy, D. Zhang, H. Y. Wang, Q. X. Jia, J. L. MacManus-Driscoll, G. Kenyon, A. Sornborger, W. Y. Nie, A. P. Chen, Adv. Intell. Syst., **5**, 2300035, (2023).

[+] Author for correspondence: Aiping Chen, apchen@lanl.gov

Neuromorphic Memristors with TiO_2 and a-IGZO Bilayer Structure

Jae-Yun Lee, Zhao han Lin, Xiao-Lin Wang, Shi-Shi Kai, Beom Gu Lee, and Sung-Jin Kim[+]

E8-1, College of Electrical and Computer Engineering, Chungbuk National University, Cheongju 28644, South Korea

In recent years, ReRAM devices have gained significant attention in neuromorphic applications and hardware-based artificial intelligence [1–2]. Specifically, the resistive memory devices exhibit ultrafast read and write speeds, high retention time [3], low voltage operation and low power consumption, emerging an attractive research target from the perspective of the modern low-cost portable devices [4].

Our proposed device performance and physical properties of the fabricated ReRAM devices were assessed at various annealing temperatures. The analysis from XPS results confirms that the device operation was mostly driven by the density of oxygen vacancies in the TiO_2 and a-IGZO bilayer structure. The optimal density of oxygen vacancies in the a-IGZO causes the drift of O^{2-} ions to and from the TiO_2 layer that induced a significant variation in the resistivity of the device, providing switching behavior.

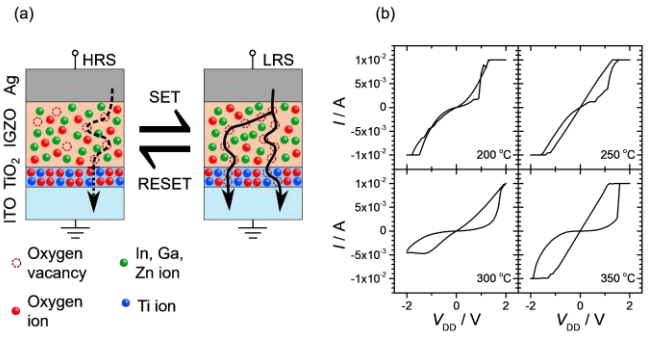

Figure 1(a) Schematic illustration of the mechanism of the conduction in the HRS and LRS (b) schematic drawing of the TiO_2 -IGZO ReRAM device with the I-V characteristics.

[1] P. Yao, H. Wu, B. Gao, J. Tang, Q. Zhang, W. Zhang, J.J. Yang, H. Qian, Fully hardware-implemented memristor convolutional neural network, *Nature* **577** (2020).

[2] S.P. Adhikari, C. Yang, H. Kim, L.O. Chua, Memristor bridge synapse-based neural network and its learning, *IEEE Trans. Neural Netw. Learn. Syst*. **23** (2012).

[3] S. Siegel, C. Baeumer, A. Gutsche, M. von Witzleben, R. Waser, S. Menzel, R. Dittmann, Trade-Off Between Data Retention and Switching Speed in Resistive Switching ReRAM Devices, *Adv. Electron. Mater.* **7** (2021).

[4] N.K. Upadhyay, W. Sun, P. Lin, S. Joshi, R. Midya, X. Zhang, Z. Wang, H. Jiang, J.H. Yoon, M. Rao, M. Chi, Q. Xia, J.J. Yang, A memristor with low switching current and voltage for 1S1R integration and array operation, *Adv. Electron. Mater.* **6** (5) (2020).

[+] Author for correspondence: ksj@cbnu.ac.kr

Origin of large electro-optic response in ferroelectrics

A. A. Demkov,[1] I. Kim,[1] T. Paolettta,[1] and S. Apte[1]
[1] *Department of Physics, The University of Texas at Austin, Austin, TX 78712, USA*

Integrated silicon photonics experiences a revolution [1]. The key element of this technology is an optical modulator (OM) playing a role similar to that of a usual transistor. OMs based on a phase shifter using a linear electro-optic (EO) effect are an attractive option for building ultra-compact, fast and low power OMs [2]. Linear EO effect can be only observed in non-centrosymmetric materials, such as ferroelectrics, which started a search for ferroelectrics that can be integrated with Si and maintain a strong EO effect in thin films [3]. Ab initio calculations became an indispensable tool in this search [4].

We will discuss our recent progress in understanding the microscopic mechanism behind the EO response in three ferroelectrics successfully integrated on Si: $BaTiO_3$ (BTO), $LiNbO_3$ (LN) and $Sr_xBa_{1-x}Nb_2O_6$ (SBN). There are three parts to the EO effect in a ferroelectric, they are ionic, piezo and electronic contributions [5,6]. In different materials, different components of the EO tensor are dominated by different contributions. This has implications for the device design, depending on the temperature and frequency range. For example, optical quantum computing occurs at cryotemperatures (when optical phonons are frozen out), and thus has rely on the electronic and piezo contributions. On the other hand, at high RF frequencies, only the ionic and electronic contributions survive. On the fundamental level, our results support the notion that P4mm BTO is a dynamic average of lower symmetry Cm structures (Fig. 1). We also discover that in SBN, surprisingly the major contribution to the EO effect comes from high frequency optical phonons (Fig. 2). And in LN, ferroelectricity and the EO response are essentially decoupled.

The work is supported by the AFOSR under Award No FA9550-18-1-0053.

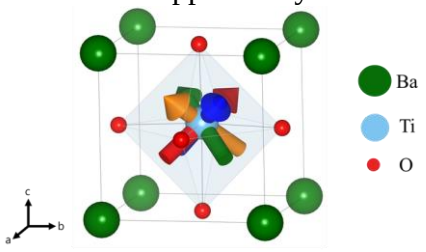

Figure 1. Ball and stick model of [111]-displacement type monoclinic *Cm* BTO, averaged in the tetragonal *P4mm* BTO.

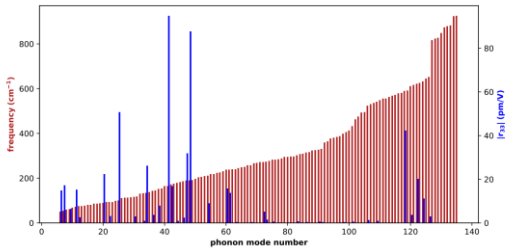

Figure 2. Phonon mode-decomposed electro-optic tensor component r_{33} in $Sr_xBa_{1-x}Nb_2O_6$. Plotted along with the mode frequencies.

[1] G. T. Reed, G. Mashanovich, F. Y. Gardes, and D. J. Thomson, Nat. Photon. **4**, 518 (2010).
[2] A. Rahim, A. Hermans, B. Wohlfeil, et al., Adv. Photonics **3**, 024003 (2021).
[3] A. A. Demkov, C. Bajaj, J. G. Ekerdt, C. J. Palmström, and S. J. B. Yoo, J. Appl. Phys. **130**, 070907 (2021); A. A. Demkov and A. B. Posadas, MRS Bulletin **47**, 485 (2022).
[4] A. K. Hamze, M. Reynaud, J. Geler-Kremer, and A. A. Demkov, Npj Comput. Mater. **6**, 130 (2020).
[5] T. Paoletta and A. A. Demkov, Phys. Rev. B **103**, 014303 (2021).
[6] I. Kim, T. Paoletta and A. A. Demkov, Phys. Rev. B **108**, 115201 520 (2023).

[+] Author for correspondence: demkov@physics.utexas.edu

Direct visualization of electronic transport in a quantum anomalous Hall insulator

G. M. Ferguson[1], Run Xiao[2], Anthony R. Richardella[2], David Low[1], Nitin Samarth[2] & Katja C. Nowack[1,3,+]

[1]Laboratory of Atomic and Solid-State Physics, Cornell University, Ithaca, NY, USA
[2]Department of Physics and Materials Research Institute, The Pennsylvania State University, University Park, PA, USA
[3]Kavli Institute at Cornell for Nanoscale Science, Cornell University, Ithaca, NY, USA

A quantum anomalous Hall (QAH) insulator is characterized by quantized Hall and vanishing longitudinal resistances at zero magnetic field that are protected against local perturbations and independent of sample details. This insensitivity makes the microscopic details of the local current distribution inaccessible to global transport measurements. Accordingly, the current distributions that give rise to the transport quantization are unknown. Here, I will discuss how we use magnetic imaging to directly visualize the transport current in the QAH regime [1]. As we tune through the QAH plateau by electrostatic gating, we clearly identify a regime in which the sample transports current primarily in the bulk rather than along the edges. Furthermore, we observe a local response of the equilibrium magnetization to electrostatic gating, whose spatial structure is strongly correlated with the observed current density. Combined, these measurements are consistent with the current flowing through incompressible regions whose spatial structure can change throughout the QAH regime.
At sufficiently high currents in the QAH regime and generally outside the QAH regime, we observe a weak response of the magnetization to the applied current. We show that this response can be explained by current-induced heating of the electrons. Effectively this allows us to image local dissipation in the QAH regime. As an example, I will show images of hot-spots localized in the corners of the electrical contacts through which the transport current enters our devices.

[1] Ferguson, G.M. *et al.* Direct visualization of electronic transport in a quantum anomalous Hall insulator. *Nat. Mater.* 22, 1100–1105 (2023).

Acknowledgments: Work at Cornell University was primarily supported by the U.S. Department of Energy, Office of Basic Energy Sciences, Division of Materials Sciences and Engineering, under award DE-SC0015947. Sample synthesis and fabrication at Penn State was supported by the Penn State 2DCC-MIP under NSF Grant Nos. DMR-1539916 and DMR-2039351.

[+] Author for correspondence: kcn34@cornell.edu

Suplementary Pages (Optional)

More optional text and figures may be submitted on up to two supplemental pages; however, please note that these pages will not be included in the online technical program book. Therefore please do not reference any text or figures from these pages on page one.

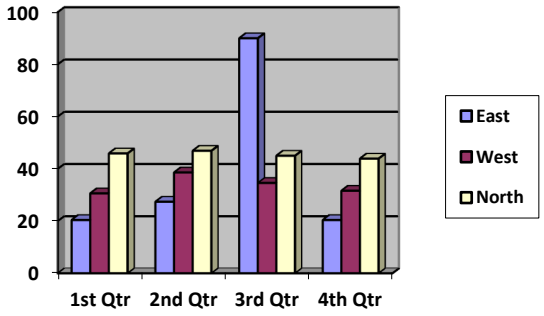

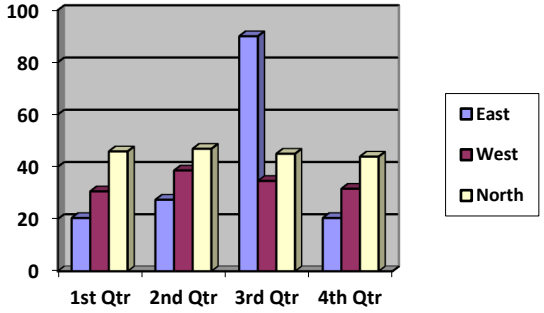

Magneto-Optical Detection of the Orbital Hall Effect in Chromium

I. Lyalin,[1] S. Alikhah,[2] M. Berritta,[2,3] P. M. Oppeneer,[2] and R. K. Kawakami[1*]

[1] *Department of Physics, The Ohio State University, Columbus, Ohio 43210, United States*
[2] *Department of Physics and Astronomy, Uppsala University, P. O. Box 516, SE-75120 Uppsala, Sweden*
[3] *Department of Physics and Astronomy, University of Exeter, Stocker Road, Exeter EX4 4QL, United Kingdom*

The Hall effect was discovered by a PhD student Edwin Hall and his advisor Henry Rowland in 1879. Since then, the family of Hall effects has grown considerably. The anomalous Hall effect, integer and fractional quantum Hall effects, spin Hall effect, quantum anomalous Hall effect are fundamental physics phenomena of great importance. The orbital Hall effect (OHE) with giant orbital Hall conductivities has recently been theoretically predicted [1-4], however its direct observation is a challenge. Here, we report the magneto-optical detection of current-induced orbital accumulation at the surface of a light 3d transition metal, Cr. The orbital polarization is in-plane, transverse to the current direction, and scales linearly with current density, fully consistent with the orbital Hall effect. Comparing the thickness-dependent magneto-optical measurements with *ab initio* calculations, we estimate an orbital diffusion length in Cr of 6.6±0.6 nm. Along with Choi *et al.* study of the OHE in Ti [5], our work [6] provides strong evidence for the OHE. The detection of the orbital Hall effect in light metals can have important consequences for future spintronics applications that could utilize orbital currents rather than spin currents.

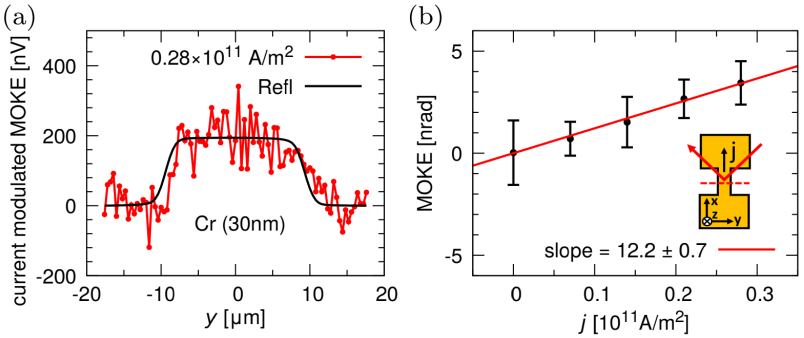

Figure 1. Magneto-optical Kerr rotation induced by the orbital Hall effect. (a) MOKE line scan across a 20 μm wide, 30 nm thick Cr wire. (b) MOKE signal as a function of current density.

[1] T. Tanaka et al., Phys. Rev. B 77, 165117 (2008).
[2] H. Kontani et al., Phys. Rev. Lett. 102, 016601 (2009).
[3] D. Go, D. Jo, C. Kim, and H.-W. Lee, Phys. Rev. Lett. 121, 086602 (2018).
[4] D. Jo, D. Go, and H.-W. Lee, Phys. Rev. B 98, 214405 (2018).
[5] Y.-G. Choi et al., Nature 619, 52 (2023).
[6] I. Lyalin et al., arXiv:2306.10673 [cond-mat] (2023) (accepted to Phys. Rev. Lett).

* Author for correspondence: kawakami.15@osu.edu

Supplementary Information:

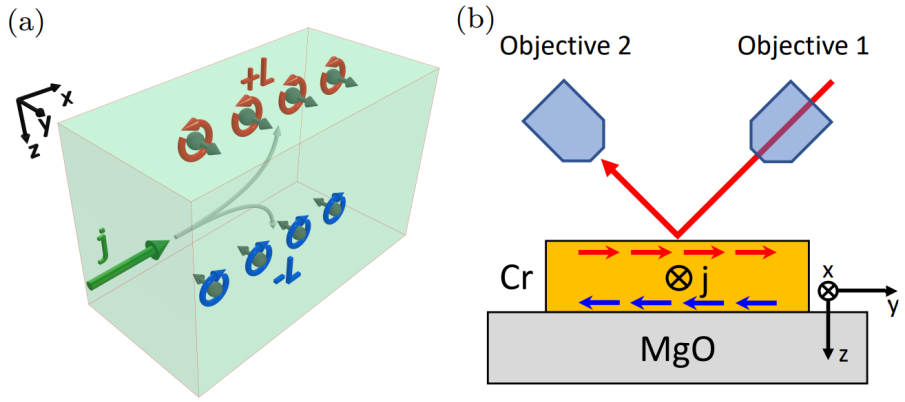

Figure 2. (a) Schematics of the orbital Hall effect. The charge current j generates a transverse orbital current, leading to orbital accumulation on the sample's surfaces. (b) Measurement setup utilizing the longitudinal MOKE to detect the in-plane orbital accumulation.

Temperature dependent study of Na_xSi_{136} type II Si clathrate spin dynamics

J. P. Briggs,[1] Y. Liu[1], S. Saiter[2], A. Faricy[2], C. Burns[2], P.C. Taylor[2], M. Singh[2], R. T. Collins[2], C. A. Koh[1]

Departments of Chemical and Biological Engineering[1] and Physics[2], Colorado School of Mines, 1500 Illinois Street Golden CO 80401

We report the temperature dependence of relaxation time (T_1) and phase memory (T_M) of Na dopants in type II Si clathrate films utilizing electron paramagnetic resonance (EPR). There is a rich history directed at understanding defect properties in conventional diamond Si motivated by its dominant position in the microelectronics industry. Type II Si clathrates represent an alternative crystal structure to diamond Si. This cage-like inclusion compound is made up of a Si lattice with interstitial "guests" situated inside the cages. Our recent advances have allowed the synthesis of Na guest, type II Si clathrate films with low enough Na concentration for the Na to be considered a dopant and the spin dynamics of isolated Na donors to be investigated.[1]

EPR gives insight into the electron spin dynamics of the Na donors and their placement and interactions within the Si cages. The naturally occurring Na isotope, ^{23}Na, has nuclear spin 3/2 with the EPR spectrum exhibiting four hyperfine lines associated with the interaction of the electron and nuclear spins. Hyperfine features associated with Na atoms in neighboring cages, clustered Na, and interactions with ^{29}Si isotopes on the cage, are also observed.[2] Pulsed-EPR spectra exhibit clear spin echo signals with T_1 times in the hundreds of microseconds at temperatures near 7 K, and T_M times above a microsecond. The effects of various parameters (i.e. temperature, magnetic field center, Na concentration) on the relaxation time and phase memory are reported. The relaxation time exhibits thermally activated behavior from 6-14K suggesting an Orbach relaxation pathway. Strong similarities and important differences between the spin dynamics of Na in clathrate and P in diamond Si will be discussed along with Na's potential to function as a qubit in quantum applications. This work was supported by National Science Foundation award #2114569.

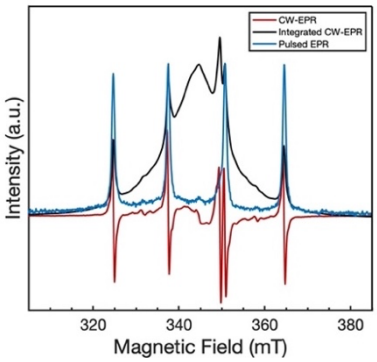

Figure 1 EPR spectra of Na doped type II Si clathrate.

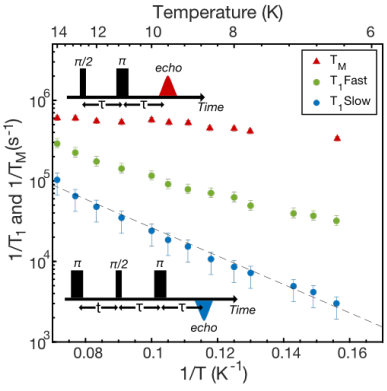

Figure 2 Na_xSi_{136} type II clathrate T_1 and T_M times.

[1] Y. Liu et al., Appl. Phys. Rev., **8,** 4(2021).
[2] W. K. Schenken et al., Phys. Rev. B, **101**, 24(2020).

+ Author for correspondence: jbriggs@mines.edu

Supplementary Information

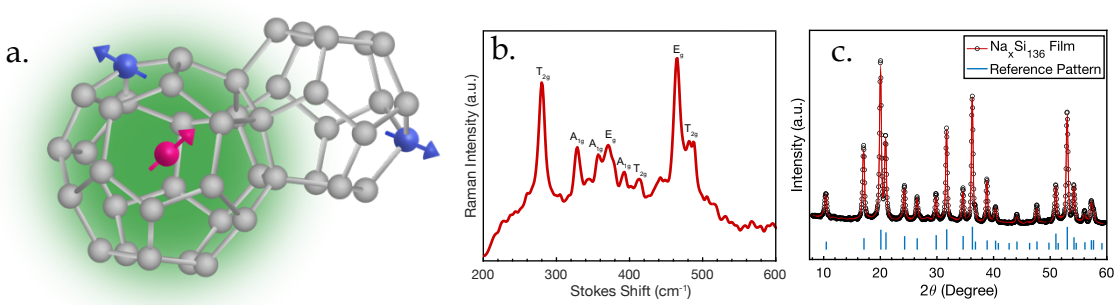

Figure 3 (a) Type II Si clathrate with spin 3/2 Na donor nucleus (pink) and donor electron (green) inside large Si cage (grey) with spin 1/2 ^{29}Si (blue). (b) Raman spectrum of Na_xSi_{136} film (c) XRD of Na film Na_xSi_{136} with reference pattern

Silicon clathrates represent an alternative crystalline form of silicon with a direct or nearly direct bandgap. The material has a much higher absorption coefficient, a larger bandgap, and more efficient light emission properties than diamond silicon.[1] As a result it is being actively explored for potential applications in solar energy conversion and optoelectronics. Typical synthesis pathways, however, introduce Na guests into the clathrate cages. Na contributes electrons and the materials have metallic properties. We have focused on reducing the Na concentration to the point where the Na can be viewed as a donor atom and the clathrate as a semiconductor.[1] This creates a situation where Na in the clathrate plays a role analogous to P in diamond Si (Si:P). Much like Si:P, the spin properties of Na in Si clathrate could have interesting application as qubits but in an optically active, larger bandgap material.[2] This is the first study to explore spin relaxation time and phase memory in the type II silicon clathrate system. The paramters examined in this study are key initial indicators for a materials potential for application in quantum systems. While the spins decay more rapidly than Si:P, doping levels are much higher and the material is much more defective. This suggests decay times can be increased and during this talk we will discuss approaches for acheiving this.

To synthesize sodium doped type II Si clathrate films, a two-step procedure adapted from powder synthesis has been developed.[1] First, bulk sodium metal is evaporated from a Ta crucible and diffused into a silicon wafer under an inert argon atmosphere to form NaSi. The wafer is then annealed under vacuum to thermally decompose the film into clathrate. The clathrate films are then characterized through a variety of techniques including Raman spectroscopy, x-ray diffraction (XRD), and scanning electron microscopy. Inversion recovery measurements of Na_xSi_{136} ($0<x<24$) type II clathrate films were performed from 6.4-25K. Each inversion recovery experiment was performed with the field centered around the highest field hyperfine line around 364 mT at 9.81 GHz,which is the right most peak in *Fig. 1*. The inversion recovery transients from 6.4-14K can be seen in *Fig. 2* before (inset with linear intensity scale) and after (main panel with log scale) inverting and subtracting the ground state magnetization taken from the end of the transient where the electrons have returned to the ground state and the signal plateaus. The time for this to occur increases with decreasing temperature indicating that temperature in this region play affect the relaxation times of type II Si clathrates. This is consistent with other silicon materials.[3]

Spin-orbit coupling in InGaAs random and digital alloy quantum wells

Jason T. Dong[1], Yilmaz Gul[2], Aaron N. Engel[1], Connor P. Dempsey[3], Teun A.J. van Schijndel[3], Michael Pepper[2], Christopher J. Palmstrøm[1,3]

[1]Materials Department, University of California, Santa Barbara, CA 93106

[2]London Centre for Nanotechnology, University College London, 17-19 Gordon Street, London WC1H 0AH, United Kingdom

[3]Deparment of Electrical and Computer Engineering, University of California, Santa Barbara, CA 93106

InGaAs two dimensional electron gases (2DEGs) have high spin-orbit coupling, making them potentially useful for spintronics [1] and topological quantum computing applications [2,3]. With increasing In concentration, InGaAs quantum wells will have lower effective masses, higher spin-orbit coupling, and higher g-factors than GaAs quantum wells [4]. Digital alloying, or growing the ternary as a superlattice,is an alternative to growing ternary III-V as a random alloy. However, the effect of digital alloying on the spin-orbit coupling in semiconductor quantum wells is not understood. Digital alloy quantum wells can potentially enhance the Rashba spin-orbit coupling by forming asymmetric interfaces with the barrier layers. Here, we use molecular beam epitaxy and magnetotransport to the role of random and digital alloying of the spin-orbit coupling of InGaAs quantum wells.

We report the growth of high electron mobility $In_{0.81}Ga_{0.19}As$ quantum wells grown as a random and a digital alloy. From low temperature magnetotransport (2 K), the electron mobility of the random alloy quantum well is in excess of 450,000 cm^2/Vs and the electron mobility of the digital alloy quantum well is in excess of 540,000 cm^2/Vs. The spin-orbit coupling of the quantum wells is extracted from fits to the weak localization in the magnetotransport data and will be presented. We will also discuss the role of interfaces on the differences in the spin-orbit coupling observed in the random and digital alloy quantum wells.

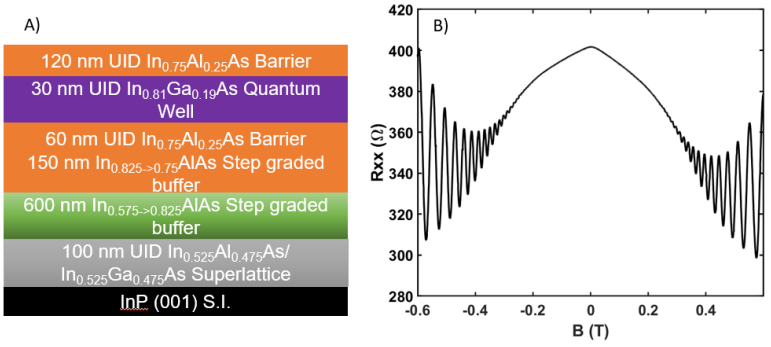

Figure 1: (A) Layer schematic of the InGaAs quantum wells. (B) Weak localization data of the InGaAs random alloy quantum well.

References

[1] *Appl. Phys. Lett.* **56**, 665 (1990)

[2] *Phys. Rev. Lett.* **105**, 077001 (2010)

[3] *Phys. Rev. Lett.* **105**, 177002 (2010)

[4] *Electron. Lett.* **37**(7), 464 (2001)

Supplementary Pages

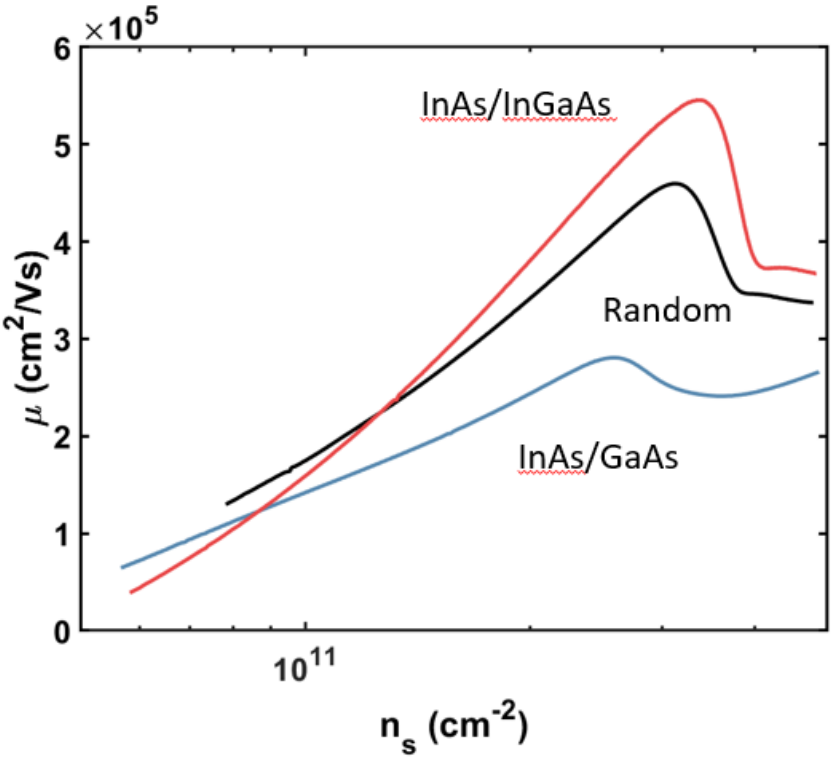

Figure S1: Mobility for different carrier densities for the random alloy and digital alloy quantum wells.

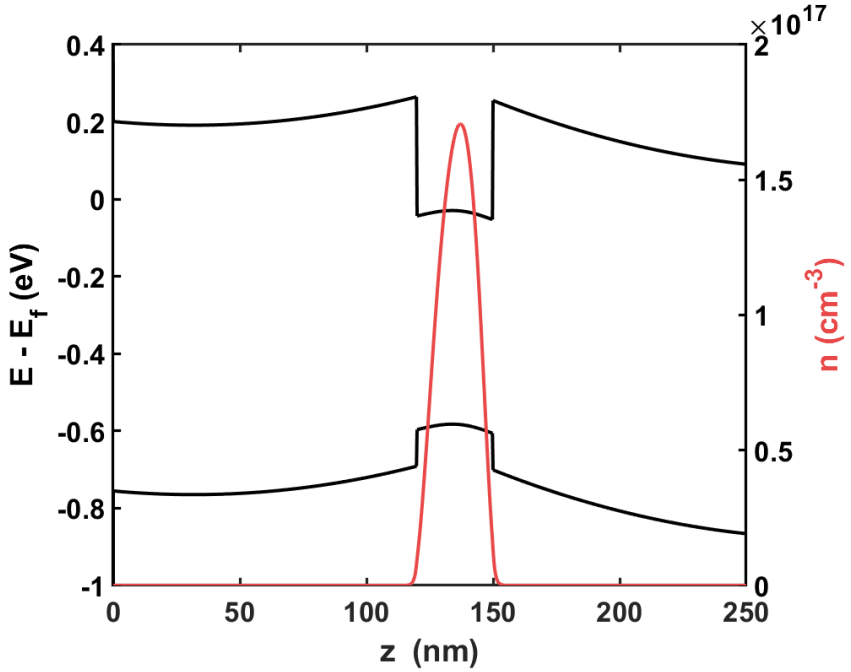

Figure S2: Self consistent Schrödinger-Poisson calculations of the band structure of the InGaAs quantum wells.

Screw Dislocations-Based Spin Valves

F. Haines,[1,2] E. J. Renteria,[1] M. L. Debasu,[1] F. Cavallo,[1,2,3]
[1]*Center for High Technology Materials, University of New Mexico, Albuquerque, NM 87106*
[2]*Nanoscience Microsystems and Engineering Graduate Program, University of New Mexico, Albuquerque, NM 87131*
[3]*Department of Electrical and Computer Engineering, University of New Mexico, Albuquerque, NM 87131*

We fabricated and characterized a vertical spin valve (VSV) based on single-crystalline Si nanomembranes (NMs) engineered with 2D arrays of screw dislocations (SDs) throughout their thickness. The device includes a bottom soft ferromagnetic contact (NiFe), Si NMs, and a top hard ferromagnetic contact (Co). Based on previously reported theoretical calculations, we expect that the operation of the VSV relies on the coherent transport of spin-polarization through SDs [1]. The first step in the fabrication of the VSV is patterning a 220 nm-thick Si NM into a 2D array of pixels with lateral sizes in the range of 200-400 μm. At this stage of the process, the NM is bonded to a SiO_2-coated bulk Si substrate. Si pixels are released in place by selective etching of the SiO_2 layer. An adhesive stamp removes the pixels from the original substrate and transfers them onto a second array of patterned pixels at a controlled twist angle, Ψ. The twisted NM pairs are then annealed at 1000-1200 °C in N_2 atmosphere to grow the SDs. Annealed NMs are finally transferred to a bulk substrate coated with NiFe. A dielectric barrier and a Co/Au top contact are fabricated using conventional top-down processes. The coercivity of the ferromagnetic films used for the contacts is extracted from measured magnetization curves on a Quantum Design Magnetic Properties Measurement System 3 (QD-MPMS3). Magneto-transport measurements characterize the resistance of the VSV at different magnitudes of magnetic induction (B). We observe a change in resistance at B corresponding to the measured coercivity of NiFe. The estimated magnetoresistance ratio, $MR(\%) = \frac{R_{AP}-R_P}{R_P}$ is -0.38 % at 300 K. No change in resistance was measured for VSVs based on Si NM that did not include SDs, suggesting that the line defects are responsible for the probed MR at 300K.

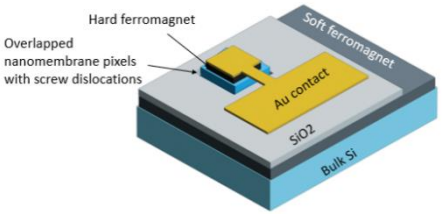

Figure 1. Schematic illustration of a vertical spin valve based on Si NMs embedding an array of screw dislocations.VSV Structure.

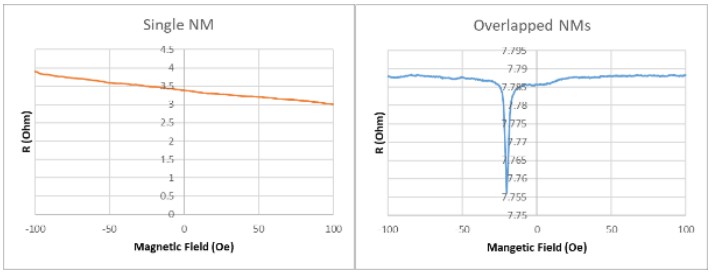

Figure 2. Magnetoresistance vs. magnetic induction for a VSV based on a Si NM that does not have screw dislocations (left panel) and for an annealed Si twisted bicrystal (right panel).

[1] L. Hu, H. Huang, Z. Wang, W. Jiang, X. Ni, Y. Zhou, V. Zielasek, M. G. Lagally, B. Huang and F. Liu, *Phys. Rev. Lett.*, 2018, **121**, 66401.

+ Author for correspondence: fhaines@unm.edu

Supplementary Pages

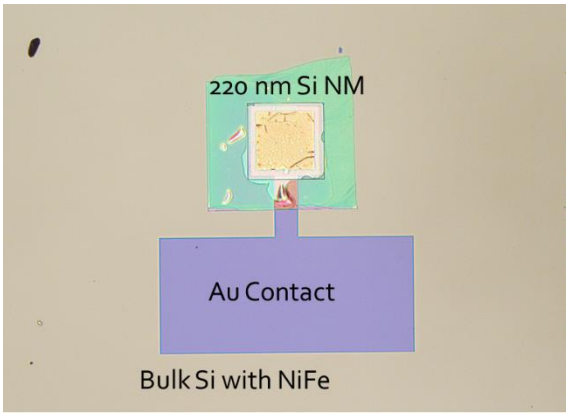

Supplementary Figure 1. Optical image of a fabricated VSV.

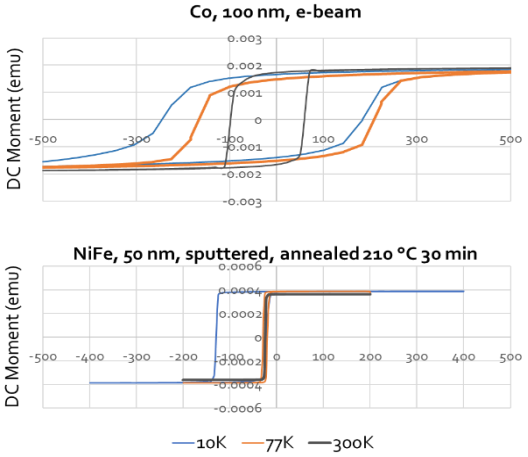

Supplementary Figure 2. Cobalt (hard) ferromagnetic layer and NiFe (soft) layer hysteresis

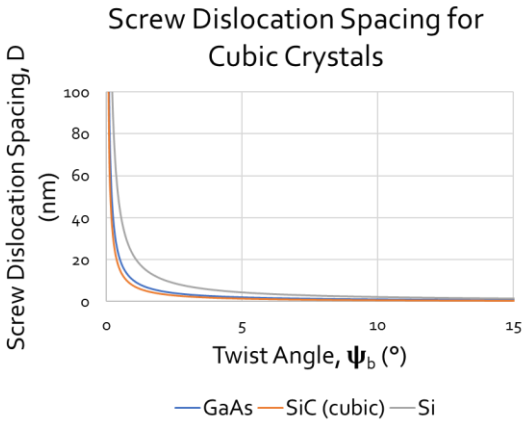

Supplementary Figure 3. Screw dislocation spacing vs. twist angle between two cubic crystals.

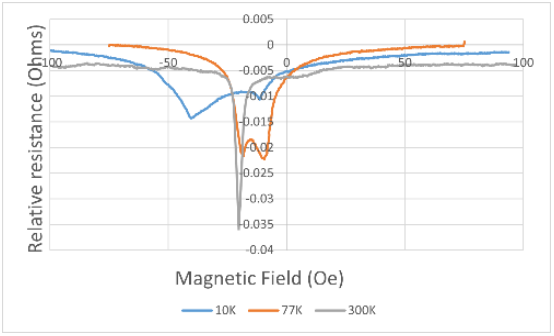

Supplementary Figure 4. Magnetoresistance vs. magnetic induction for annealed Si twisted bicrystals at different temperatures

ACKNOWLEDGEMENT. Work at the University of New Mexico was supported by the NSF CAREER award No. 2144944. This work was performed, in part, at the Center for Integrated Nanotechnologies, an Office of Science User Facility operated for the US Department of Energy (DOE) Office of Science by Los Alamos National Laboratory (Contract 89233218CNA000001) and Sandia National Laboratories (Contract DE-NA-0003525).

Imaging the Properties of Atoms and Fields at the Picometer Scale inside Materials and Devices

David A. Muller

School of Applied and Engineering Physics, and Kavli Institute for Nanoscale Science
Cornell University

Electron microscopes use electrons with wavelengths of a few picometers, and are potentially capable of imaging individual atoms in solids at a resolution ultimately set by the intrinsic size of an atom. Even with the rapid advances in aberration-corrector technology, both residual aberrations in the electron lenses and multiple scattering of the incident beam inside the sample, the best resolution possible was an order of magnitude worse than this limit. However, with recent advances in detector technology [1] and ptychographic algorithms to unscramble multiple scattering, the resolution of the electron microscope is now limited only by the dose to the sample, and thermal vibrations of the atoms themselves [2]. At high doses, these approaches have allowed us to image the detailed vibrational envelopes of individual atom columns as well as locating individual interstitial atoms that would be hidden by scattering of the probe with conventional imaging modes. The three-dimensional nature of the reconstruction means surface relaxations can be distinguished from the bulk structure, and interface roughness and step edges inside devices can be resolved – including gate-all-around transistors and Josephson junctions. Even the location of all atoms in thin amorphous films now seems within reach. These approaches have also allowed us to image the internal structures of both magnetic and ferroelectric vortices, skyrmions and merons, including their singular points that are critical for accurately describing the topological properties of these field textures.

[1] M. W. Tate, P. Purohit, D. Chamberlain, K. X. Nguyen, R. Hovden, C. S. Chang, P. Deb, E. Turgut, J. T. Heron, D. G. Schlom, D. C. Ralph, G. D. Fuchs, K. S. Shanks, H. T. Philipp, D. A. Muller, and S. M. Gruner. "High Dynamic Range Pixel Array Detector for Scanning Transmission Electron Microscopy" *Microscopy and Microanalysis* **22**, (2016): 237–249.
[2] Z. Chen, Y. Jiang, Y.-T. Shao, M. E. Holtz, M. Odstrčil, M. Guizar-Sicairos, I. Hanke, S. Ganschow, D. G. Schlom, and D. A. Muller. "Electron Ptychography Achieves Atomic-Resolution Limits Set by Lattice Vibrations" *Science* **372**, (2021): 826–831

Cryogenic growth and *in-situ* fabrication of superconducting Tantalum devices

Teun A. J. van Schijndel[1], Anthony P. McFadden[3], Aaron N. Engel[2], Jason T. Dong[2], Shirshendu Chatterjee[1], Raymond Simmonds[3], Chris J. Palmstrøm[1,2].

[1] *Electrical & Computer Engineering Department, University of California Santa Barbara, Santa Barbara, California 93106*

[2] *Materials Department, University of California Santa Barbara, Santa Barbara, California 93106*

[3] *National Institute of Standards and Technology, Boulder, Colorado 80305*

Superconducting devices are crucial in various fields of quantum information technology, including superconducting qubits and topological quantum computing. The vast majority of either of these qubit technologies use Aluminum as the superconducting component. Al is generally grown at low temperatures to achieve smooth thin films. This allows for easy integration of Al-based devices with material systems such as sapphire, Si, Ge, or III-V materials due to minimal interfacial reactions. Also, Al is often used for Josephson Junctions (JJ) that require *in-situ* oxidation to form AlO_x barriers. While Al is the most common superconductor, other superconductors show promising results as well. In particular, Tantalum-based superconducting qubits on sapphire show low loss and long coherence times.[1,2] One of the contributing factors to the enhancement of qubit performance is their higher chemical resistance during device fabrication. However, only a few substrates can be used to stabilize the required α-Ta phase with a BCC lattice structure. Due to its resilience to high temperatures, low-loss sapphire can withstand the growth of Ta at elevated temperatures necessary for the realization of desirable superconducting properties. Growth of Ta on Silicon or III-V substrates remains a challenge.

In this work, we explore the MBE growth and *in-situ* fabrication of superconducting tantalum films. The growth at ultralow temperatures below 10K shows the stabilization of the required superconducting phase of Tantalum (α-Ta). Moreover, Figure 1 shows that α-Ta can be stabilized at low temperatures regardless of the substrate choice. In each case, a superconducting transition temperature of above 4K is observed. Furthermore, this deposition technique can be combined with *in-situ* shadow masks, which allows for patterns with at least 1 μm precision. This can be used to realize $Ta/Ta_2O_5/Ta$ JJ's by using the native oxide, which is something that has never been shown before, or by depositing other dielectrics *in-situ* such as Silicon or Germanium. Our work demonstrates the growth of high-quality superconducting devices, which enables the exploration of different superconductors and dielectric combinations for use in quantum information technology.

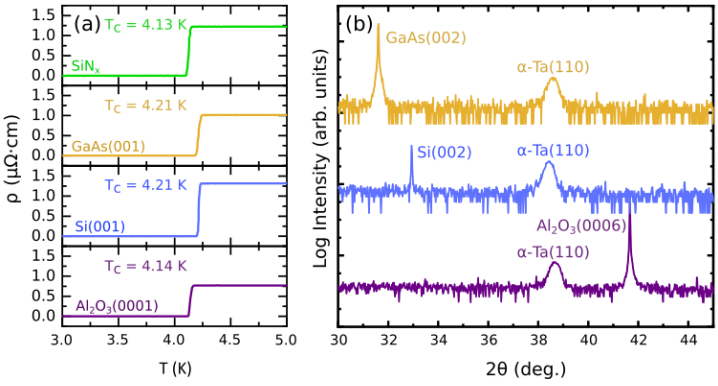

Figure 1. Electrical and structural characterization of Tantalum grown at different substrates. (a) Resistivity as a function of temperature measured in 4-probe in a line geometry for the substrates SiN_x, GaAs(001), Si(001), and Al_2O_3(0001). (b) XRD Spectra for crystalline substrates, in which α-Ta(110) peak is visible regardless of substrate.

[1] Nat Commun 12, 1779 (2021).
[2] npj Quantum Inf 8, 3 (2022).

Author for correspondence: teunvanschijndel@ucsb.edu

Multi-technique characterization of GaN-based devices: a powerful tool to probe the in-depth chemistry

K. Gaffar,[1], S. Béchu[1], G. Patriarche[2], M. Bouttemy[1]

[1] *Institut Lavoisier de Versailles, UVSQ, Université Paris-Saclay, CNRS, UMR 8180, 45 avenue des Etats-Unis, 78035 Versailles CEDEX, France*
[2] *C2N, Université Paris-Saclay, CNRS, Palaiseau, France*

Gallium Nitride (GaN) technology has proven to be a contender for power electronic applications and has shown its suitability for GaN-based devices such as High Electron Mobility Transistors (HEMT) for high-frequency applications. However, the miniaturization of the device dimensions, such as gate length, requires a thorough mastering of device fabrication process with the help of suitable analytical techniques. In particular, systematic electrical characterization has shown that the interface states have a significant impact on the electrical performance and long-term reliability of GaN HEMT devices. This work ambitions to develop a robust methodology to perform advanced chemical characterization of GaN transistors and better understand how the chemistry of the constitutive layers and interfaces properties impact the electrical response. In addition to STEM/EDX analysis on cross sections, conventionally used to access quantitative information and epitaxy quality, an innovative methodology combining X-ray photoemission spectroscopy (XPS) and Auger Electron Spectroscopy (AES) is developed. Indeed, these techniques not only provide access to elemental compositions but also to key information on chemical environments, especially modifications induced by each technological step during device fabrication. In particular, (nano)-Auger spectroscopy, with its high spatial resolution (12 nm), is a very promising tool to access buried interfaces directly on cross-section, bringing complementary information to STEM/EDX such as oxidation states or contaminant presence. If the added value of this multi-technique approach is obvious, the direct implementation and interpretation of XPS and Auger analyses is not straightforward. In fact, access to the ultimate composition of any GaN-based structure is conditioned by the fitting procedure to ensure a reliable nitrogen content determination. We propose here a reliable methodology to decompose gallium $L_2M_{4.5}M_{4.5}$ transition and nitrogen N 1s photopeak overlap for precise quantification. We will show how these preliminary results obtained by XPS and STEM/EDX analysis are crucial for an accurate interpretation of Auger spectrum acquired on the same materials with the nano-probe for chemical state identification and to refine the quantification. The correlation between structural observations, chemical information and electrical performances measured on a HEMT transistor will be illustrated on a concrete case.

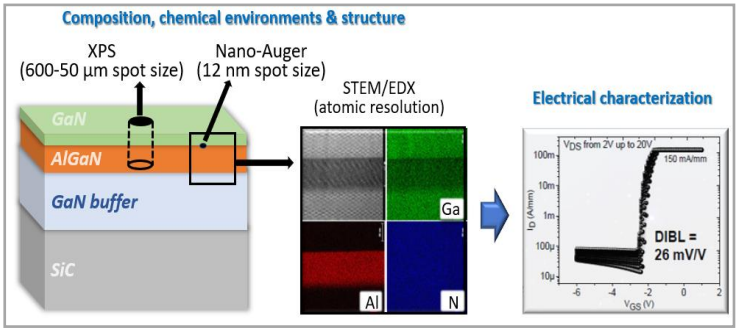

Figure 1: Overview of the multi-technique methodology employed for GaN devices characterization

+ Author for correspondence: gaffarkirene@outlook.fr

Supplementary Pages (Optional)

Gallium Nitride (GaN) technology has made drastic progress in the development of GaN-based HEMT devices over the past 10 years [1]. However, these electrical devices still require a thorough optimization of several phenomena such as high trapping effects which degrade the dynamic performance of GaN components. Although the understanding of these phenomena is not fully mastered, studies have shown that the interface states have a significant impact on the electrical characteristics of GaN HEMT devices [2]. To address this issue, we propose an innovative methodology combining STEM/EDX, XPS and nano-Auger to accurately characterize the composition at critical locations in the transistor structure, among them interfaces.

A first study combining the X-Auger electrons spectroscopy (X-AES) transitions simultaneously obtained with the X-ray photoemission spectroscopy (XPS) photopeaks using an Al-Kα source has been carried out. In HEMT transistor cases, several issues are identified: the depth probed by the XPS (≈ 10 nm) can be higher than the structures' multilayers thicknesses [3] and, in addition, Ga $L_2M_{4.5}M_{4.5}$ transition and nitrogen N 1s photopeak overlap. The use of a Mg source may not resolve the issue as another Auger line will be superimposed to the nitrogen photopeak. Thus, access to the ultimate composition of the HEMT structure may become a difficult process leading to erroneous information. The fitting method developed in this study for XPS data allows the modeling of Ga $L_2M_{4.5}M_{4.5}$ (~ 395 eV) and Ga $L_3M_{4.5}M_{4.5}$ (~ 420 eV) X-AES transitions including N 1s photopeak (~ 398 eV) using oxidized/deoxidized gallium-based references (III-V binary alloys) in order to determine the gallium and nitrogen contributions in GaN based-materials. This new and original approach consists of using the higher energy Auger line (Ga $L_3M_{4.5}M_{4.5}$) to help us find and fix the right fitting parameters on the lower energy transition where the overlap between nitrogen and gallium occurs. As experimental conditions during sample cleaning process could be limited while transferring them with possible exposure to air and results in oxidized surfaces, gallium oxide chemical environment has also been considered. With the aim of reaching buried interfaces, modifications induced by sputtering while depth profiling have been studied for developing a strong and universal methodology for processing XPS data of GaN components. The fitting parameters such as the background, peak positions, area ratio, Full Width at Half Maximum of gallium Auger transitions have been determined for each reference sample. The following figure (2) illustrates the methodology development: Ga_2O_3 sample is used to fix the gallium oxide envelope (a) to separate the oxide contribution from the Ga alloy environment (b), itself used as a base to model the GaN – surface spectra (c). While sputtered with an Ar+ monoatomic ion beam, both Auger transitions from the sputtered GaN sample present a new shape, different from the one on the surface requiring additional contributions (d). Once the sputtering effect is stabilized, the new shape parameters are determined and the fitting method is applied to an AlGaN sample (e) to control

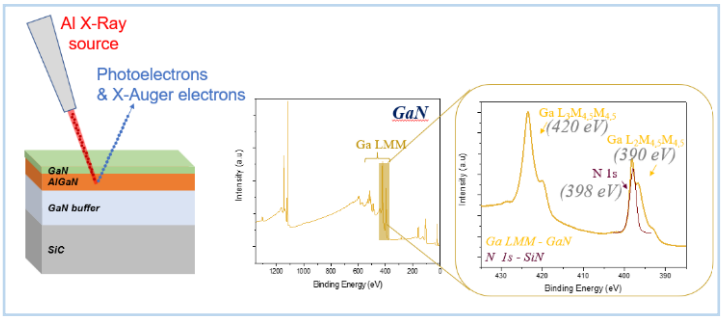

Figure 1: Overlap of N1s/Ga $L_3M_{4.5}M_{4.5}$ region using XPS Al K source

Mo-SiN_x granular metal high-pass filters

L. Biedermann, M. McGarry, S. Gilbert, W. Bachman, M. Meyerson, L. Yates, P. Sharma, J. Flicker, P. Kotula, and M.P. Siegal
Sandia National Laboratories, 1515 Eubank Blvd SE, Albuquerque, NM 87185

Granular metals (GMs) comprise a 3D network of metal nanoparticles embedded in a dielectric matrix. Over the past ~50 years, GM investigations have spanned fundamental physics to unique applications, including Au-SiO_2 GMs used as insulating contacts in vidicons, video cameras used in NASA's Apollo and Voyager missions [1]. As a controlled platform for electron transport studies, GMs exhibit tunneling transport (*e.g.* variable-range hopping, Poole-Frenkel conduction in Ni-SiO_2 GMs) and frequency-dependent conductivity $\sigma(\omega)$ in Pt-SiO_2 and Pd-ZrO_2 GMs [2-4]. These prior GM investigations focused almost exclusively on metal-oxide GMs. Our goal—to develop nanosecond-responsive high-pass filters for electrical grid applications—has advanced development of Mo-SiN_x GMs that exploit these conductivity mechanisms.

High-dielectric strength SiN_x is an attractive matrix for GMs, enabling Mo-SiN_x and Co-SiN_x GMs [5]. However, initial Mo-SiN_x GMs showed weak $\sigma(\omega)$; thermally-excited resistive transport through defective SiN_x overwhelmed the desired transport mechanisms. Fortunately, sputtering Mo-SiN_x in a partial N_2 environment ameliorates these SiN_x matrix defects. X-ray photoemission spectroscopy (XPS) analysis shows deleterious $MoSi_2$ is further reduced by annealing in H_2/N_2 forming gas (Fig. 1a). Improvements in SiN_x insulator quality resulted in the desired many decades reduction in σ_{DC} (Fig. 1b). This evaluation of nanostructure and chemical structure has enabled optimization of high-frequency and high electric (E) field transport (Fig. 1c, d), key properties of high-pass filters for electric grid applications [6].

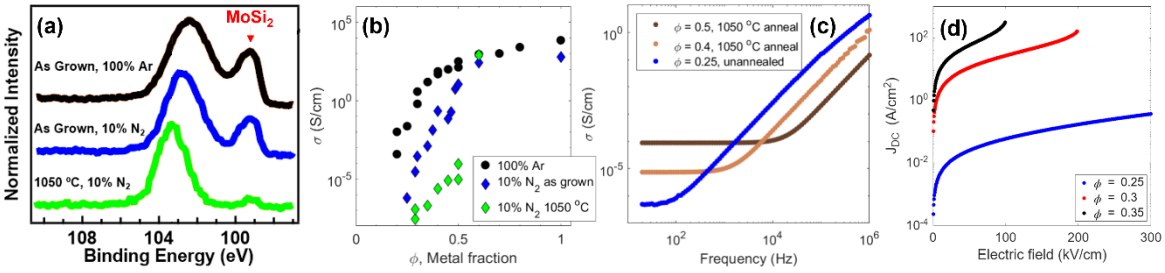

Figure 1: In (a), the Si 2p XPS spectra for Mo-SiN_x. In (b), σ_{DC} versus Mo fraction, φ. In (c), frequency response $\sigma(\omega)$. In (d), current density, J, increases with E-field and φ; Ohmic, Poole-Frenkel, and Fowler-Nordheim transport are observed.

This work was supported by the Laboratory Directed Research and Development program at Sandia National Laboratories (SNL). SNL is managed and operated by NTESS under DOE NNSA contract DE-NA0003525. SAND2023-09502A.

[1] C. Wronkski, B. Abeles, and A. Rose, *Appl. Phys. Lett.* **27**, 91 (1975).
[2] P. Sheng, B. Abeles, and Y. Arie, *Phys. Rev. Lett.* **31**, 44-47 (1973).
[3] N. Moyo and K. Leaver, *J. Phys. D: Appl. Phys.* **13**, 1511 (1980).
[4] H. Bakkali *et al.,* Sci Rep **6**, 29676 (2016)
[5] S. Gilbert *et al.*, *Nanotechnology* **34**, 415706 (2023).
[6] M. McGarry, L. Biedermann, *et al.,* "Electric response of Mo-SiN_x granular metals." (in preparation).

+ Author for correspondence: lbieder@sandia.gov

Restructuring Cracks in Rutile TiO_2 with Radiolysis-Driven Rolling of Octahedral Units

Silu Guo[1*], Hwanhui Yun[1,2], Sreejith Nair[1], Bharat Jalan[1] and K. Andre Mkhoyan[1*]

[1] *Chemical Engineering and Materials Science, University of Minnesota, Twin Cities, Minneapolis, MN 55455, USA*
[2] *Korea Research Institute of Chemical Technology, Daejeon 34114, Korea*

[*]Authors for correspondence: guo00208@umn.edu; mkhoyan@umn.edu

When energetic electrons interact with crystals in transmission electron microscope (TEM), a combination of "knock-on" and radiolysis effects takes place [1]. Radiolysis, in particular, is known to either amorphize or crystalize materials and limit the accuracy of the measurements [2]. However, the precise atomistic mechanisms of these transformations are still under debate. Here, we use scanning TEM (STEM) imaging and electron energy loss spectroscopy (EELS) to study the bond-breakage, atomic movements and crystallization mechanisms in rutile-TiO_2 driven by radiolysis [3].

Thin-film rutile IrO_2 was grown on top of rutile TiO_2, introducing nano-meter width cracks due to an anisotropic epitaxial strain (Figure 1a). To assess the impact of electron beam exposure on the structural healing process of the atomically sharp cracks in rutile-TiO_2, high angle annular dark-field STEM (HAADF-STEM) time-lapse images of the cracks were obtained (Figure 1b). With the accumulation of electron doses, the crack undergoes a self-healing restructuring process. Based on these observations and quantitative EELS analysis, we propose a "2-step rolling" model for the TiO_6 octahedral building blocks located at the crack's edge of rutile-TiO_2 as a possible mechanism for radiolysis-driven atomic migration (Figure 1c and d). With radiolytic bond breakage (Figure 1c), the TiO_6 octahedral units from the edge of the crack can roll and occupy new sites and, in the process, move materials from both sides of the crack into the gap (Figure 1d) [3].

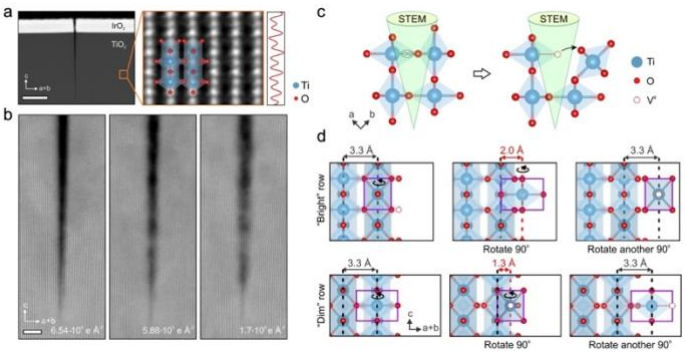

Figure 1. a, A rutile IrO_2/TiO_2 sample with an atomically sharp crack. **b,** A set of HAADF-STEM images showing the self-healing crystallization in the center of the crack with increase of electron doses. Scale bar is 3 nm. **c,** Radiolysis-driven Ti-O bond breakage between two octahedra units in rutile TiO_2. **d,** A "2-step rolling" model for octahedral motion from the "bright" and "dim" row configurations.

[1] L. Reimer and H. Kohl, *Transmission Electron Microscopy: Physics of Image Formation* (Springer, Berlin, 2008), 5th edn.
[2] L. W. Hobbs, *Introduction to Analytical Electron Microscopy*, edited by J. J. Hren, J. I. Goldstein, and D. C. Joy (Scanning Microscopy International, Chicago, 1979), p. 437
[3] S. Guo, H. Yun, S. Nair, B. Jalan and K. A. Mkhoyan (arXiv: 2304.03482)

Supplementary Information

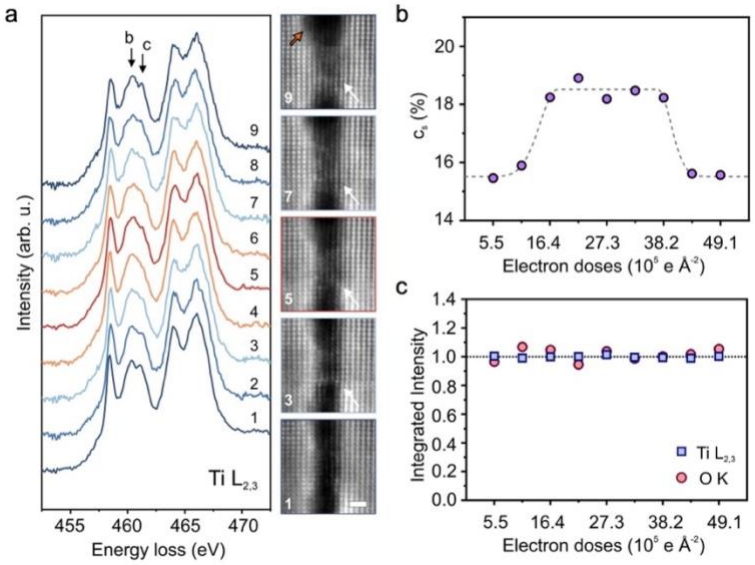

Supplementary Figure 1. a, A set of EELS Ti-$L_{2,3}$-edges as function of electron beam doses from a crack region in rutile TiO_2. Five HAADF-STEM images are acquired in parallel with these EELS measurements showing bridging. Scale bar is 1 nm. The peaks "b" and "c" with most changes are at 460.3 and 461.1 eV, correspondingly. **b,** Concentrations of surface Ti atoms in the exposed crack area (c_s) as a function of electron dose determined from Ti $L_{2,3}$-edge spectra in **a**. **c,** The changes in the number of Ti and O atoms as a function of electron dose in beam-exposed crack area in **a** are evaluated using integrated intensities of Ti $L_{2,3}$- and O K-edge EELS spectra [3].

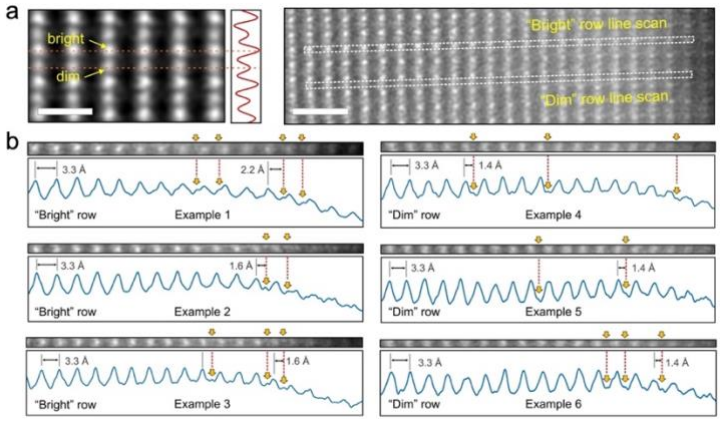

Supplementary Figure 2. a, Atomic-resolution HAADF-STEM image of [110] rutile TiO_2. Orange dashed lines show the rows of "bright" and "dim" atomic columns. Scale bar is 0.5 nm. On the right, a magnified image from the crack bridging region with dashed rectangle strips indicating where the "Bright" row and "Dim" row line scans are taken. Scale bar is 1 nm. **b,** Six examples of one-atom-width strips of HAADF-STEM images and the corresponding intensity line scans. They show the locations of Ti atoms at interstitial sites with specific 2.2 Å, 1.6 Å and 1.4 Å spacings from the main columns [3].

Growth and angle-resolved photoemission of strain- and thickness- tuned epitaxial α-Sn thin films

A.N. Engel[1], H.S. Inbar[1], P.J. Corbae[2], C.P. Dempsey[2], S. Nishihaya[2], Y.-H. Chang[1], J. T. Dong[1], A.V. Fedorov[3], M. Hashimoto[4], D. Lu[4], C. J. Palmstrøm[1,2]

[1]*Materials Department, University of California Santa Barbara, CA, USA*

[2]*Dept. of Elec. and Comp. Eng., University of California Santa Barbara, CA, USA*

[3]*Advanced Light Source, Lawrence Berkeley National Lab, CA, USA*

[4]*Stanford Synchrotron Radiation Lightsource, SLAC National Accelerator Lab, CA, USA*

α-Sn, the diamond structure allotrope of Sn, is a zero-gap semiconductor with band inversion. Calculations suggest that epitaxial tensile strain induces a 3D topological insulator (TI) phase, while epitaxial compressive strain induces a 3D Dirac semimetal (DSM) phase [1,2]. When this DSM phase is confined in a thin film, it has been suggested to form a quasi-3D TI phase [3]. Transitions to other phases instead, such as 2D TI, have been suggested as well [4].

We first explore the topological phase of ultrathin unintentionally doped α-Sn thin films. Using spin- and angle-resolved photoemission spectroscopy (ARPES), we study compressively strained α-Sn films on InSb(001). We find clear evidence of the confinement-induced quasi-3D TI phase in compressively strained α-Sn. We also find that the spin-polarization of the topological surface states differs markedly from reports in the literature where the films are intentionally doped with Te [5], indicating this intentional doping (a frequently used procedure) could have a significant effect on the electronic structure of α-Sn.

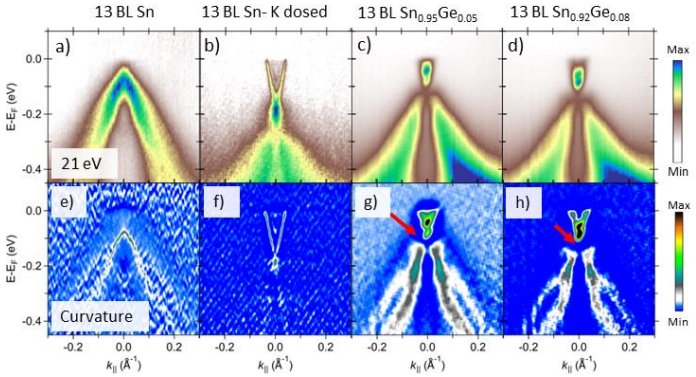

Figure 1. Topological phase transition upon Ge alloying as observed in ARPES (hν=21 eV) spectra for 13 bilayers a) Pristine α-Sn (-0.15% strain) b) Potassium dosed (electron doping) of the same film c) 5% Ge alloying (+0.5%) d) 8% Ge alloying (+0.9%). A small gap opens at the surface Dirac node with Ge alloying, indicating a topological phase transition. The size of this gap increases with Ge content e)-h) Curvature of a)-d) to enhance band features.

With the previous behavior benchmarked, we then alloy the α-Sn films with Ge to decrease the bulk lattice constant and switch from compressive to tensile strain when grown on InSb(001). Morphology changes as a function of Ge alloying were studied with *in-situ* scanning tunneling microscopy, and strain was confirmed through X-ray diffraction. Finally, the presence of a topological phase transition induced by tensile strain *away* from the expected 3D TI phase is found in ARPES (Fig. 1). Our results pave the way for a better understanding of the effect of strain and confinement on α-Sn's band structure.

[1] Phys Rev B **97**, 195139 (2018).
[2] Phys Rev B **90**, 125312 (2014).
[3] Phys Rev Lett **111**, 216401 (2013).
[4] Advanced Materials **33**, 2104645 (2021).
[5] Phys Rev B **97**, 75101 (2018).

Author for correspondence: aengel@ucsb.edu

Supplementary Information

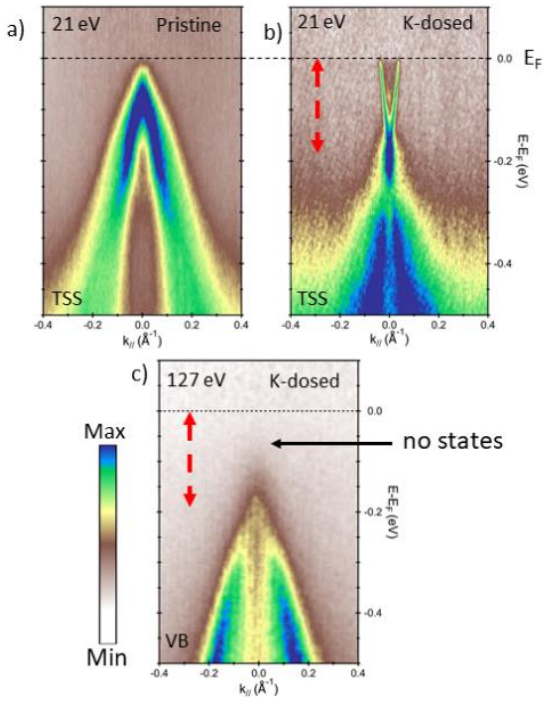

Figure 2. Determination of the 3D topological insulator-like state in 13 BL α-Sn. ARPES measurement at 21 eV before a) and after b) potassium dosing the surface. Potassium dosing effectively electron dopes the surface, allowing to see further above the surface Dirac node. The surface Dirac node is preserved. c) ARPES measurement at 127 eV photon energy after potassium dosing the surface. At this photon energy the bulk states at the bulk Γ are observed. There is clear evidence of the valence band, but no conduction band below the Fermi level. This indicates at least a 200 meV bulk band gap. This film is thus 3D topological insulator-like.

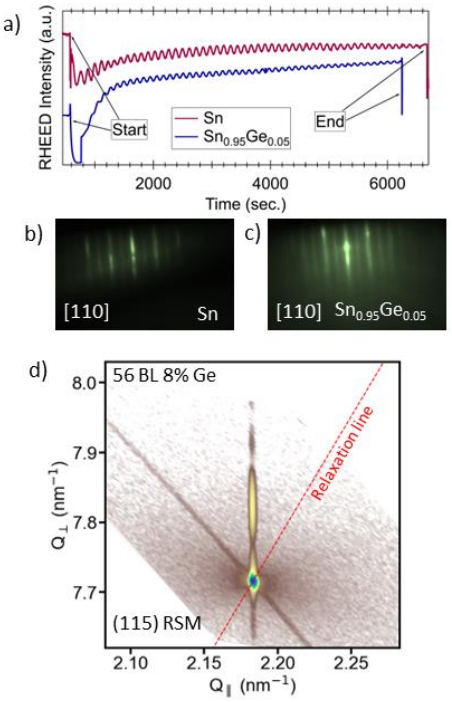

Figure 3. Growth of α-SnGe thin films. a) RHEED oscillations showing preservation of layer by layer growth mechanism when the Sn films are alloyed with Ge. b) RHEED pattern of (2x1)/(1x2) in 50 BL α-Sn. c) The same as b) in 50 BL α-SnGe. d) High resolution XRD reciprocal space map around the InSb(115) peak showing the α-SnGe is fully strained. Pendellosung fringes in the (00l) direction are clear, indicative of high quality interfaces.

Characterization of Buffer Layers for Remote Plasma-Enhanced Chemical Vapor Deposition of Germanium-Tin Epitaxial Layers

S. Zollner,[1] C. A. Armenta,[1] B. Rogers,[2] G. J. Grzybowski,[3,4] B. Claflin[4]
[1]Dept. of Physics, New Mexico State University, Las Cruces, NM, USA
[2]Dept. of Chemical and Biomolecular Eng., Vanderbilt University, Nashville, TN, USA
[3]KBR, 3275 Pentagon Boulevard, Beavercreek, OH 45431, USA
[4]Air Force Research Laboratory, Sensors Directorate, WPAFB, OH 45433, USA

Germanium-tin alloys are of interest for infrared light detectors to increase capabilities in image and data capture and transmission, because they can have a direct band gap with more than about 7% tin. Remote plasma-enhanced chemical vapor deposition (RPECVD) is attractive for growth of Ge-Sn alloys because it enables low-temperature epitaxy on Si using common precursors GeH_4 and $SnCl_4$. The growth of such epilayers can be optimized with an initial high-temperature buffer layer. This work focuses on the characterization of this buffer layer using atomic force microscopy, ellipsometry, thin-film powder x-ray diffraction, and x-ray photoelectron spectroscopy (XPS) for different growth conditions.

Thin Ge and Ge-Sn buffer layers with 10-20 nm thickness were deposited on Si (100) substrates for one minute at temperatures from 360°C to 500°C with varying SnCl4 precursor flows mixed with GeH4 and helium. Ellipsometry spectra for all films show critical point structures in the E_1, $E_1+\Delta_1$, and E_2 region of Ge, indicating that all layers are crystalline. A layer grown at 360°C without $SnCl_4$ can be described reasonably well as an 11 nm thick layer of crystalline germanium with 2 nm of roughness. Adding $SnCl_4$ to the gas flow significantly reduces the height of the ε_2 maximum at E_2, indicating that the layer is rough. In addition, a new broad peak appears near 1.3 eV, which is attributed to plasmonic effects arising from metallic β-tin inclusions. The plasmon peak disappears in the layers grown at 490°C with the same $SnCl_4$ flow. We conclude that depositing the buffer layer with $SnCl_4$ at low temperatures leads to β-Sn precipitates, where plasmon oscillations can be excited, but are not present for high-temperature growth.

The tin contents in the layers were also estimated by x-ray photoelectron spectroscopy. While XPS measures the total amount of tin in the layers, the presence of substitutional tin in $Ge_{1-x}Sn_x$ alloy buffers is best determined with x-ray diffraction. The (002) diffraction peak is forbidden in pure Ge, because the contributions from the two Ge atoms in the primitive unit cell cancel. It is absent in our buffers grown without $SnCl_4$ or at high temperature. The (004) XRD peak position in these layers is also very similar to pure Ge. The $Ge_{1-x}Sn_x$ (002) peak does appear in buffers grown at temperatures lower than 460°C. From the position of the (004) XRD peak, we can estimate the tin content to be below 7%, ignoring the effects of residual stress. This tin content determined from XRD shifts is much lower than the total tin content of about 20% estimated by XPS. The excess tin is contained in β-tin precipitates, which lead to the plasmonic ellipsometry peaks mentioned earlier.

In summary, the substitutional tin content in thin $Ge_{1-x}Sn_x$ buffer layers grown directly on Si substrates by RPECVD is modulated by temperature and $SnCl_4$ flow rates. Excess tin is present in β-tin precipitates, which lead to plasmonic resonances in ellipsometry spectra.

Near Zero-Field Magnetoresistance and Defects in GaN pn Junctions

M.J. Elko,[1] A.A. Higgins,[1] D.T. Hassenmayer,[1] P.M. Lenahan,[1]D. Fehr,[2] M.E. Flatté,[2] T.D.Larsen,[3] M. D.Craven[3]

[1]Dept. ESM, Pennsylvania State University, University Park, PA, USA
[2]Dept. of Physics and Astronomy, University of Iowa, Iowa City, IA, USA
[3]NexGen Power Systems, Santa Clara, CA 95934, USA

We report on observation of near zero-field magnetoresistance (NZFMR) in GaN devices, in this case, pn junction diodes. NZFMR is a new technique with great potential in electronic materials physics. [1,2] The NZFMR response is due to recombination centers within the diode depletion regions. A representative NZFMR amplitude versus magnetic field plot is shown in figure 1. Figure 2(a) illustrates the anticipated depletion region 2(b) shows the measured NZFMR amplitude versus junction bias. The agreement between the calculated response of figure 2(a) and the experimental observations of figure 2(b) should be considered reasonably convincing, considering multiple approximations involved. The NZFMR pattern peaked near the built-in voltage is expected from recombination within the depletion region. [3,4] The NZFMR phenomena are somewhat similar to low field magnetoresistance phenomena observed in some organic semiconductors. The NZFMR response can be understood within the framework of the stochastic quantum Liouville expression. [1,2] Preliminary analysis of traces represented by figure 3, based upon this framework, indicates that the NZFMR response is consistent with nitrogen vacancies.

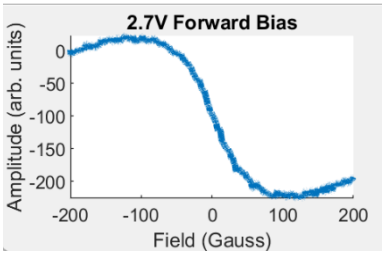

Figure 1. An example of an NZFMR trace in a GaN pn diode.

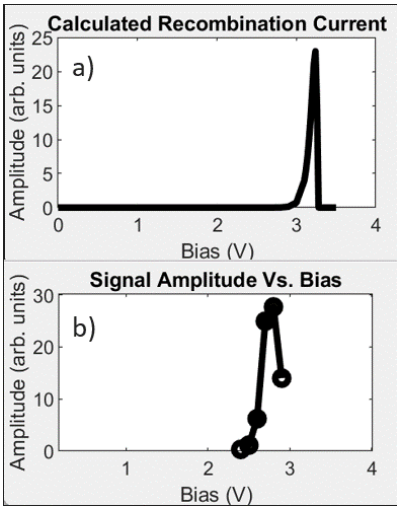

Figure 2. (a) Calculated recombination current in diode. (b) observed NZFMR amplitude with respect to forward bias.

[1] N. J. Harmon, S. R. McMillan, J. P. Ashton, P. M. Lenahan, and M. E. Flatté, IEEE Trans. on Nucl. Sci., pp. 1669, vol. 67, (2020).
[2] E. B. Frantz, N. J. Harmon, D. J. Michalak, E. M. Henry, M. E. Flatté, S. W. King, J. S. Clarke, and P. M. Lenahan, J. Appl. Phys., vol. 130, 234401, (2021).
[3] A.S. Grove, Physics and Technology of Semiconductor Devices, Chapter 6, John Wiley and Sons, New York, London (1967).
[4] C.J. Cochrane and P.M. Lenahan, J. Appl. Phys. 112, 123714 (2012).
We gratefully acknowledge support from AFOSR Grant FA9550-22-1-0308.

Heteroepitaxy of PbSe-SnSe semiconductors on GaAs for infrared optoelectronics

K. Mukherjee
[1]*Department of Materials Science and Engineering, Stanford University*

The IV-VI semiconductor alloy of PbSe-SnSe has rich materials physics and several device applications[1]. This narrow band gap semiconductor system spans a 3D-bonded rocksalt structure on the PbSe-rich side and a closely related Van der Waals bonded 2D/layered-orthorhombic structure on the SnSe-side, and has long been studied for its rare electronic, photonic, and thermal properties. We present results from epitaxial integration of IV-VI semiconductor films with III-V templates using molecular beam epitaxy to understand how we may harness their properties for emerging applications infrared optoelectronics.

With attractively low temperatures for epitaxy below 300 °C, we describe the nucleation and growth of IV-VI materials on III-V substrates and the formation of extended crystal defects that arise due to integration[2]. We find bright band-edge photoluminescence in the mid-infrared (3–4 μm) from PbSe and PbSnSe epitaxial films on ~8% mismatched GaAs at room temperature, despite a threading dislocation density exceeding $10^9/cm^2$. We present measurements of carrier recombination in PbSe and show preliminary results from junction devices of mid-infrared light emitting diodes and photodetectors that highlight the promise of this materials platform.

The IV-VI on III-V template also enables us to probe deeper into the structural phase boundaries and miscibility gaps in PbSnSe, with an aim to harness the high contrast in optical properties across the transition between 3D/rocksalt to 2D/layered bonding. We show that MBE synthesis can stabilize the layered phase deep in the bulk miscibility gap. Close to a composition of $Pb_{0.5}Sn_{0.5}Se$, we find evidence for a displacive or martensitic transformation (without composition change) between the rocksalt and layered phases in our thin films. These results, in agreement with recent reports in high temperature quenched samples[3], point the way to phase change devices.

[1] G. Springholz and G. Bauer, physica status solidi (b), 244, 8, 2752–2767, 2007
[2] B. B. Haidet, E. T. Hughes, and K. Mukherjee, Phys. Rev. Materials, 4, 3, 033402, 2020
[3] T. Katase et al. Science Advances, 7, 12, eabf2725, 2021

[+] Author for correspondence: kunalm@stanford.edu

Investigation of localized electric fields of InAs/GaAs quantum dot interfaces

T. I. Kang,[1] J. S. Kim,[1] S. J. Lee[2]
[1]Department of Physics, Yeungnam University, Gyeongsan 38541, Korea
[2]Division of Convergence Technology, Korea Research Institute of Standards and Science, Daejeon 34113,Kore

In InAs/GaAs QDs, the strain-induced lattice deformation and strain induced dislocation could generate localize electric fields (LEF) due the piezo-electric fields [1]. Therefor the electric field distribution could be more complex at the interface of QDs than for the 2D superlattice (SL). The strain-induced complex electric fields can significantly modify the quantum confinement states. Direct observation of strain-related effect, such as the LEFs caused by strain-induced polarizations and defects, is therefore very important. Photoreflectance spectroscopy (PR) is useful for investigating LEFs of semiconductors [2]. In the case of GaAs, the Franz-Keldysh oscillations (FKOs) that appear above the band gap of GaAs and contain information about the LEFs in GaAs. To investigate InAs/GaAs quantum confinement states PR experimental results were reported [3]. However, experimental observation of LEFs attributed to strain between InAs QD and GaAs has not been the focus of many studies.

In this work, we investigated LEFs between InAs QD and GaAs by PR. FIG.1 shows the InAs/GaAs QDs sample used in this work. FIG. 2 shows the PR spectra of the InAs/GaAs QD samples obtained at low temperature. The low-temperature PR spectrum of the InAs/GaAs QD shows clear FKO transitions above the GaAs band gap energy. This work suggests that the interface electric fields attributed to strain originate from the strain-induced polarization near the InAs QD interface in GaAs metric. We suggested that the FKOs originated from the LEFs predominately caused by the strain-induced polarization at GaAs interface near the InAs QDs. The InAs/GaAs QDs have a broad range of interface electric fields from ~10^4 V/cm to ~2x10^5 V/cm.

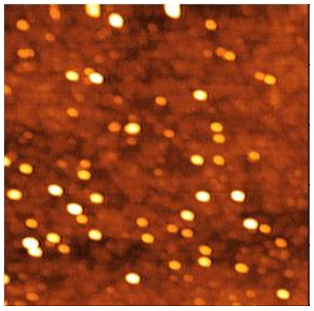

Figure 1. AFM image of InAs/GaAs QD

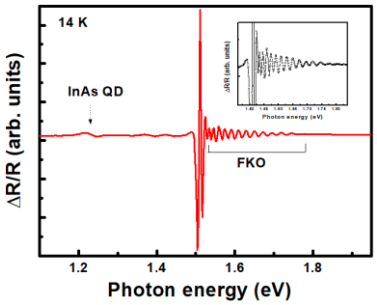

Figure 2. Low temperature PR spectrum of InAs/GaAs QD

[1] C. Pryor, Phys. Rev. B 60, 2869(1999).
[2] C.W. Sohn, I.S. Han, R.P. Smith, J.S. Kim, et al, Korean Phys. Soc. 64, 1031 (2014).
[3] R. Nedzinskas, B. Cechavicius, A. Rimkus, et al, J. Appl. Phys. 117, 144304 (2015).
+ Author for correspondence: jongsukim@ynu.ac.kr

X-STM study of Interlayer Effects on InAs Quantum Dots in InP

E.G.Banfi[1+], E.M. Sala[2], R.S.R. Gajjela[1], J. Heffernan[2], P.M. Koenraad[1]
[1] *Department of Applied Physics, Eindhoven University of Technology , The Netherlands*
[2] *EPSRC National Epitaxy Facility and Department of Electronic and Electrical Engineering, The University of Sheffield, United Kingdom*

Quantum dots (QDs) have been studied in the past two decades in order to optimize their performances in a wide range of applications, from QD lasers, photovoltaics, single photon emitter, memories, and last but not least, quantum communication and information technologies [1-6]. In order to further follow this line of optimization it is relevant to achieve more size and shape uniform QDs. This work targets the optimization process of droplet epitaxy (DE) InAs QDs in InP by the use of interlayers.

In this work we performed, with atomic scale resolution, cross-sectional scanning tunneling microscopy (X-STM) on InAs DE QDs in InP, we also characterized the QDs with atomic force microscopy (AFM) and performed finite element simulations (FES). We measured two samples with different compositions in the interlayer (IL), the region below the QDs. The first sample has an $In_{0.53}Ga_{0.47}As$ IL and consists of two separate QDs layer with different amount of In (referred to as QDL1 and QDL2). The two regions are separated by 100nm of InP in order to reduce the chances of seeding of the QDs formation. The second sample has an IL composed by $In_{0.719}$ $Ga_{0.281}$ $As_{0.608}$ $P_{0.392}$ (Fig. 1) lattice matched to the InP of the host. Our study performed on these samples, highlighted how some previously identified effects (trenches and etch-pit formation [7]) were successfully avoided in these samples. We studied size, shape and composition of all the QDs measured. AFM and X-STM proved that these dots have a rhombic base elongated preferentially along the {110}. We performed FES and we can conclude that in the second sample the QDs purity is 95±5% InAs, while in the other sample the purity is around 90±5%. Results confirmed are not only by the relaxation and lattice constant but also from our X-STM measurements. These results prove that introducing P in the IL region can enhance the purity of the QDs and allow for a stress-free structure.

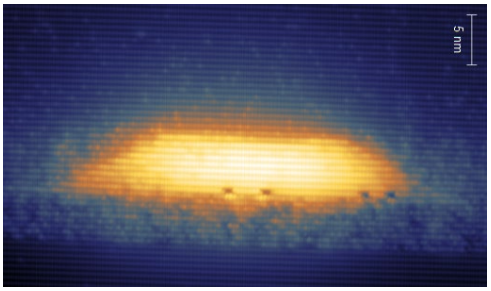

Figure 2 Filled state X-STM image of a QD on the InGaAsP IL sample.

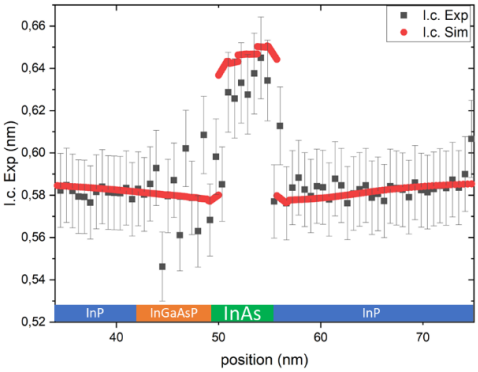

Figure 1 Lattice constant (l.c.) of QD in Fig. 1 both from experiment and from FES. In the InAs region there are three different P concentration, from left to right 10%, 5% and 0% P.

[+] Author for correspondence: e.g.banfi@tue.nl

[1] D. Bimberg *et al,* doi: 10.1109/2944.605656
[2] Phu Lam *et al,* doi: 10.1016/j.solmat.2014.03.046
[3] J. Martín-Sánchez *et al*, doi: 10.1021/nn9001566
[4] E.M. Sala *et al*, doi: 10.1002/pssb.201800182
[5] R.H. Hadfield, doi: 10.1038/nphoton.2009.230
[6] R.M. Stevenson *et al*, doi: 10.1038/nature04446
[7] R.S.R Gajjela *et al,* doi: 10.1021/acsanm.2c01197

Atomic scale analysis of N dopants in InAs

T.J.F. Verstijnen,[1] D. Tjeertes,[1] E.G. Banfi,[1] Q. Zhuang[2] , P.M. Koenraad[1]
[1] *Department of Applied Physics and Science Education, Eindhoven University of Technology, P.O. Box 513, 5600 MB Eindhoven, The Netherlands*
[2] *Physics Department, Lancaster University, Lancaster LA1 4YB, United Kingdom*

The band gap of most III-V semiconductors is strongly reduced with the introduction of only a few percent of N, even if the III-N alloy has a much bigger band gap. N impurities in InAs introduce an impurity state around 1 eV above the conduction band minimum, much deeper in the band than in other III-V materials. Topographic scanning tunneling spectroscopy measurements (STS) and areal spectroscopy measurements performed on N atoms up to two layers below the (110) surface of InAs show a reduction of the resonance energy of the N atom with increasing depth. This is attributed to tip induced band bending, pulling the N states up at positive bias and acting most strongly on surface N atoms. An example of STM images on InAs:N is shown in figure 1. STS measurements obtained on undoped InAs and N-doped InAs show a band gap reduction of <0.1 eV. Spacial imaging of features corresponding to N dopants up to two layers below the surface are also compared to density functional theory simulations and show excellent correspondence. Spectroscopy maps of N atoms up to two layers below the surface provide a high resolution spatial and spectroscopic view of the N atoms. Here the characteristic shape of the N atoms in different layers below the surface is observed as an enhancement of the dI/dV signal compared to the InAs background. At energies above the enhancement a reduction of the dI/dV is observed, which has the same shape and size as the enhancement. This shows that the redistribution of density of states caused by the N impurities is mainly energetic in nature.

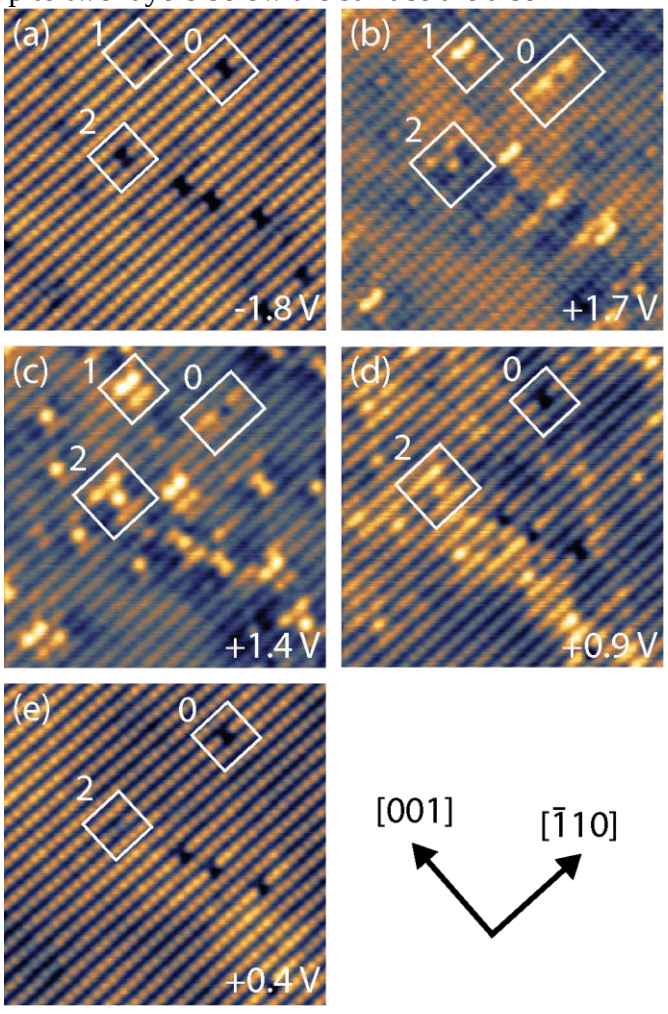

Figure 1 STM images of InAs:N at different voltages. (77K, 50pA)

Direct wafer bonding of GaN on AlN through the optimization of Chemical Mechanical Polishing

K. Pan,[1+] K. Huynh,[1] M. Li,[2] Y. Ge,[2] T. Fisher,[2] Y. Hu,[2] and M. S. Goorsky[1]
[1]Department of Materials Science and Engineering, University of California Los Angeles, Los Angeles, California, 90095, USA
[2]Department of Mechanical and Aerospace Engineering, University of California Los Angeles, Los Angeles, California, 90095, USA

Optimization of surface preparation and interfacial characterization of direct wafer bonded GaN to AlN are presented in this study. In particular, the Ga face of the GaN wafer was bonded to the N face of the AlN wafer. The as received Ga-face of GaN substrates showed <1 nm roughness while the N-face AlN had a starting roughness of ~3 nm RMS. The N-face of the AlN was successfully polished to <1 nm RMS roughness suitable for direct wafer bonding using chemistry based on our previous work with GaN CMP [1]. For bonding, 2" GaN (Unipress) and 2" AlN (Hexatech) were bonded using standard cleaning and immersion in a $(NH_4)_2S$ solution. The samples were rinsed, dried and pressed Ga- to N-face (AlN) under moderate pressure (~50 kPa) and room temperature bonding was initiated. A significant fraction of the surfaces bonded, except for a couple of triangular regions associated with growth sector boundaries in the GaN. Subsequent annealing up to 800 C° was performed to strengthen the bond and to test the structure for high temperature stability. Similar coefficient of thermal expansion between GaN and AlN at high temperatures allows for high temperature annealing without debonding or cracking. The GaN substrate was then grinded and also subject to CMP to < 1um for transmission electron microscopy and time-domain thermal reflectance measurements of the bonded interface.

High resolution transmission electron microscopy shown in Figure 1 reveals complete crystallinity across the interface. However, only a ~1.5 nm interfacial region is observed, which is suspected to be caused by reconfiguration of the interface after a total anneal of 350 °C 22 hours, 600 °C 1 hour, and 800 °C 1 hour. No thicker amorphous or oxide interfacial layer commonly found in other bonding methods (surface activated bonding, plasma treatment, or other interfacial layers) [2-5] are observed in this study. Preliminary thermal boundary conductance measurements via time domain thermal reflectance have been measured and will be reported.

[1] S. Hayashi, et al., J. Electrochem. Soc., 155(2), p.H113 (2007)
[2] M.E. Liao, et al., ECS Trans., 86(5), 55 (2018)
[3] V. Dragoi, et al., ECS Trans., 86(5), 23 (2018)
[4] Y. Xu, et al., Ceram. Int., 45, 6552 (2019).
[5] F. Mu, et al., Appl. Surf. Sci., 416, 1007 (2017)

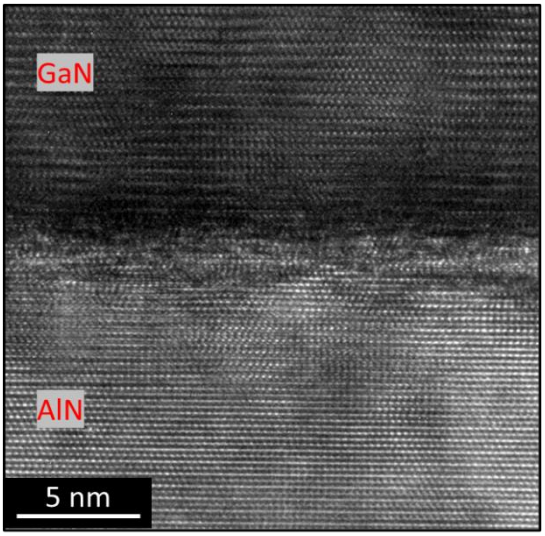

Figure 1 HRTEM of the wafer bonded GaN-AlN interface. ~1.5 nm interface can be observed due to reconfiguration of atoms after high temperature annealing.

[+]Author for correspondence: kaichengpan@g.ucla.edu

Strategies for Analyzing Non-Common-Atom Heterovalent Interfaces: The Case of CdTe-on-InSb

E. Luna[1], A. Trampert[1], J. Lu[2], T. Aoki[3], Y.-H. Zhang[4], M.R. McCartney[5], and D. J. Smith[5]

[1] Paul-Drude-Institut für Festkörperelektronik Leibniz-Institut im Forschungsverbund Berlin e.V., Hausvogteiplatz 5-7, D-10117 Berlin, Germany

[2]School of Engineering for Matter, Transport and Energy, Arizona State University, Tempe, AZ 85287, USA

[3] LeRoy Eyring Center for Solid State Science, Arizona State University, Tempe, AZ 85287, USA

[4] School of Electrical, Computer and Energy Engineering, Arizona State University, Tempe, AZ 85287, USA

[5] Department of Physics, Arizona State University, Tempe, AZ 85287, USA

Semiconductor heterostructures are intrinsic to a wide range of modern-day electronic devices. Knowledge of chemical interfacial profiles in these complex structures is critical to the task of optimizing the device performance. Here, we report on an innovative methodology that enables reliable interface structure analysis of non-common-atom heterovalent interfaces on all relevant length scales from hundred-nm to atomic resolution.

Non-common-atom (NCA) heterovalent interfaces offer potential benefits arising from the valence mismatch but also contain challenges due to the large charge imbalances. Whether a sharp polar interface is formed or, on the contrary, there are mixtures of chemical bonds across the interface leading to a nonpolar graded interface is under intense discussion. Furthermore, very little has so far been done to exploit the opportunities offered by NCA heterovalent interfaces, in part due to challenges determining the structure and properties of these types of interfaces, for example, by using scanning transmission electron microscopy (STEM) techniques. This work presents a comprehensive analysis of the composition profile across the case study NCA heterovalent CdTe/InSb interface, carried out using a combination of (S)TEM imaging and spectroscopic techniques. Techniques such as high-angle annular-dark-field and large-angle bright-field STEM, as well as electron energy-loss spectroscopy, give results from the interface region on the atomic scale. These measurements, however, are inherently difficult to interpret because of the close atomic numbers of the constituent elements. In contrast, use of the 002 dark-field TEM imaging mode emphasizes the interface location by comparing differences in structure factors between the two materials. Based on the 002 dark-field TEM, a methodology was developed for reliable determination of the composition profile across the interface and systematic quantification of the interface width. Since the identities of both cations and anions change across the heterointerface, the respective contributions of different elements need to be inserted separately. The intermixing at each sub-lattice is thus independently and completely determined. Comparisons of experimental and simulated CdTe-on-InSb profiles reveal that the interface is structurally abrupt to within about 1.5 nm defined by the variation between 10 and 90%. The present investigation opens new routes to the systematic investigation of heterovalent interfaces, formed by the combination of other valence-mismatched material system.

[+] Author for correspondence: luna@pdi-berlin.de

Supplementary Pages (Optional)

Coherent, defect-free CdTe/InSb interface probed on different length scales (a) $\mathbf{g}_{002}$ dark-field (DF) TEM micrograph and (b) atomically-resolved aberration-corrected scanning transmission electron microscopy (STEM), resolving projections of individual atomic columns ("dumbbells"). Although aberration-corrected STEM allows polarity determination, the exact CdTe/InSb interface position cannot be determined unambiguously. In contrast, use of the chemically sensitive $\mathbf{g}_{002}$ DFTEM imaging technique emphasizes the interface location as shown in Fig. 1(a) [inset: I_{002}^{exp} intensity line-scan used to evaluate the ratio R_{002}^{exp} ($I_{002}^{CdTe}/I_{002}^{InSb}$)]. Schematic representation of the proposed methodology and, in particular, of the iterative procedure used to determine the composition profiles across the NCA heterovalent CdTe/InSb interface: (c) composition profiles for Cd and Te, each based on sigmoidal functions and independently inserted into the calculation, used as input for the calculation of R_{002} ($I_{002}^{CdTe}/I_{002}^{InSb}$) and (d) comparison made with R_{002}^{exp} until best fit obtained. The method allows investigation of the distribution profile for each element separately. The interface is abrupt to within about 1.5 nm (10–90% criterion).

Multi-Material Deposition for Spatial Atomic Layer Deposition Process

A. Varga,[1] M. Carnoy,[1] M. Plakhotnyuk,[1] I. Kundrata,[1] J. Bachmann.[2]
[1] *ATLANT 3D, Mårkærvej 2B, 2630 Taastrup, Denmark.*
[2] Friedrich-Alexander Universität, *Schloßplatz 4, 91054 Erlangen, Germany.*

Spatial Atomic Layer Deposition (sALD) offers a unique opportunity for localized deposition due to its physical separation and isolation of precursor and co-reagent dosing.[1] While simple in theory, due to well-developed examples of sALD, in practice miniaturization of sALD requires substantial effort into the creation of suitable micro-nozzles.[1] Uniquely, ATLANT 3D has developed proprietary sALD micronozzles, called microreactor Direct Atomic Layer Processing - µDALP™.

The µDALP™ process undergoes the same cyclic ALD process but is only done in a spatially localized area.[2] The microreactor or micronozzle confines the flows of gases used for ALD within a defined µm-scale area on the substrate, to deposit the desired material.

Since sALD and the µDALP™ process are based on physical separation, it is theoretically compatible with any ALD material process however requires development as ALD processes are highly tool dependent.[3] As such, the material capabilities can match traditional ALD and exceed other patterning techniques, such as lithography, which can be costly and time-consuming, especially for rapid prototyping required for innovation.[4,5]

Using a small amount of precursor multiple film materials and thicknesses can be deposited onto a single wafer within only a few hours, compared to days for a traditional ALD process (Fig 1.). Films deposited with ATLANT 3D technology have been shown to produce high-quality, crystalline, atomically precise thin films used to fabricate temperature (Fig 2.) and capacitive sensors with sensitivities that meet or exceed those of devices made using conventional vapor phase deposition techniques . Low-cost rapid prototyping facilitated by ATLANT 3D technology of such devices enables design innovation and optimization not possible with other thin film deposition techniques.

[1] Poodt P., JVSTA., 2012, 30, 010802
[2] Kundrata I., et al., Small Methods., 2022, 6 (5), 2101546
[3] Barry, S. T. Chemistry of Atomic Layer Deposition; De Gruyter
[4] Kundrata I., et al., ALD/ALE 2022 [Int. Conf.], 2022
[5] Plakhotnyuk M, et al., ALD/ALE 2022 [Int. Conf.], 2022

+ Author for correspondence: av@atlant3d.com

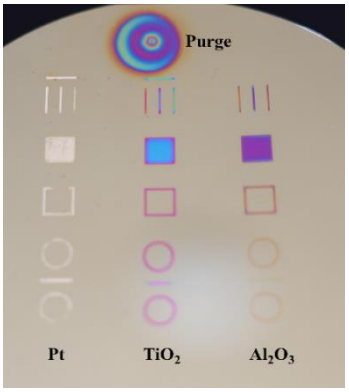

Fig 1. Photograph of 200 mm SiO2 silicon wafer substrate with thin films deposited using µDALP™.

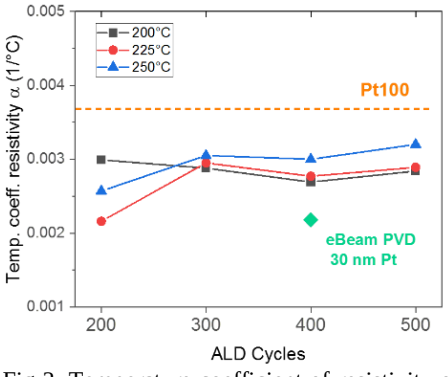

Fig 2. Temperature coefficient of resistivity of µDALP™ devices fabricated at different temperatures. Performance approaches that of a standard macroscopic Pt100 sensor and is superior to a lithography-processed reference.[2]

Surface Transfer - Modulation Doping at a Diamond-Dielectric Interface

Yu Yang,[1] Aditya Deshmukh,[2] Franz A. Koeck,[1] Xingye Wang,[2] and Robert J. Nemanich[1]

[1]*Department of Physics, Arizona State University, Tempe, Arizona 85287-1504, USA*

[2]*School for Engineering of Matter, Transport and Energy, Arizona State University, Tempe, Arizona 85287-6106, USA*

Great strides in diamond wafer technology and diamond epitaxy have inspired new concepts for diamond electronics particularly for power conversion and RF applications. However, the high activation energy of substitutional p- and n-type dopants in diamond has limited the development of field effect transistors (FET). An alternative approach of charge transfer doping at a diamond-dielectric interface, which results in the formation of a hole accumulation layer, is not limited by thermal activation [1]. However, the hole transport shows a mobility that is much lower than predicted. It is widely accepted that the low mobility is due to scattering from the near interface negative charges transferred into the dielectric layer.

Following the concept of modulation doping at heterostructure interfaces [2], we have proposed and demonstrated (Fig. 1) a dielectric layer configuration that results in a nearly ten-fold mobility increase for the accumulated holes at the diamond interface [3]. In this approach MoO_3 is used as the charge transfer dielectric, and Al_2O_3 is employed as the modulation doping spacer layer. The charge transfer is driven by the energy difference between the diamond valence band and the charge transfer states in the MoO_3. The thickness of the spacer layer also affects the hole accumulation layer charge density.

In this study photoemission spectroscopy is employed to measure the band alignment and band bending throughout the multi -layer structure. The relative distribution of the charge near the interface is deduced from the band diagram. Another study developed a modulation doping approach using acceptor molecules (NO_2) to enable the charge transfer from the diamond valence band. They achieved results that were similar to the multi dielectric layer approach.

These experiments and the model of Surface Transfer - Modulation Doping demonstrates a new approach to FET channel doping for diamond field effect transistors. We also discuss options for improving modulation doping in diamond FET's.

This research was supported by a grant from MIT-Lincoln Laboratories and the NSF through Grant Nos. DMR-1710551 and DMR-2003567.

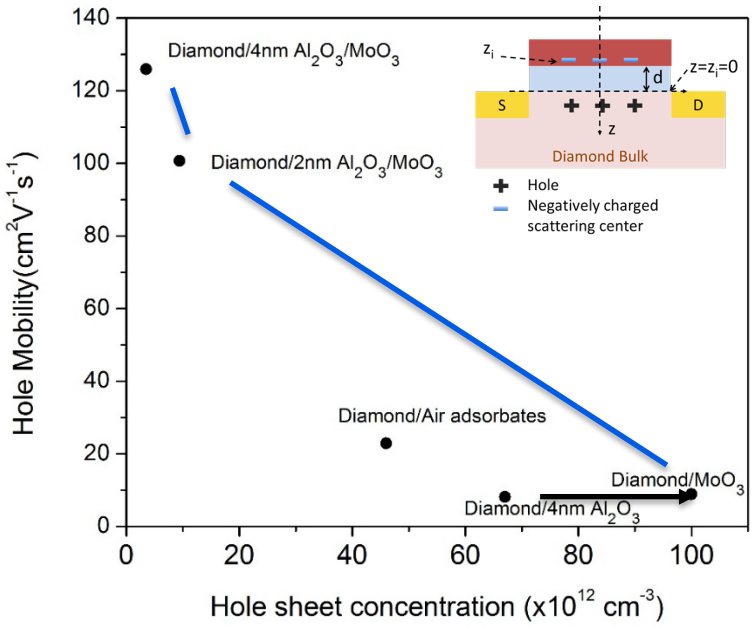

Fig. 1. Mobility vs hole sheet concentration for various charge transfer structures on diamond. The blue lines connect the surface transfer – modulation doping structures with different modulation spacer thicknesses.

[1] K. G. Crawford, I. Maini, D. A. Macdonald, and D. A. J. Moran, "Surface transfer doping of diamond: A review," Prog. Surf. Sci. 96, 100613 (2021).

[2] K. Lee, M. S. Shur, T. J. Drummond, and H. Morkoc, "Low field mobility of 2-d electron gas in modulation doped AlxGa1-xAs/GaAs layers," J. Appl. Phys. 54, 6432 (1983).

[3] Yu Yang, Franz A. Koeck, Xingye Wang, and Robert J. Nemanich "Surface transfer doping of MoO3 on hydrogen terminated diamond with an Al2O3 interfacial layer," Appl. Phys. Lett. 120, 191602 (2022).

[4] Makoto Kasu, Niloy Chandra Saha, Toshiyuki Oishi and Seong-Woo Kim "Fabrication of diamond modulation-doped FETs by NO2 delta doping in an Al2O3 gate layer," Appl. Phys. Express 14, 051004 (2021)

Operation-induced short-term degradation mechanisms of 275-nm-band AlGaN-based deep-ultraviolet light-emitting diodes fabricated on a sapphire substrate

S. F. Chichibu,[1] **K. Okuno**,[2] **M. Oya**,[2] **Y. Saito**,[2] **H. Ishiguro**,[3] **T. Takeuchi**,[3] **K. Shima**[1]
[1] *IMRAM, Tohoku University, Sendai, Miyagi 980-8577, Japan*
[2] *Toyoda Gosei Co. Ltd. Inazawa, Aichi 490-1312, Japan*
[2] *Faculty of Science and Technology, Meijo University, Nagoya, Aichi 468-8502, Japan*

The short-term degradation mechanisms of 275-nm-band AlGaN multiple quantum well (QW) deep-ultraviolet light-emitting diodes fabricated on a (0001) sapphire substrate were investigated under hard operation conditions with the current density of 66 A/cm^2 and the junction temperature of 105 °C. The optical output power (P_o) decreased by about 20 % within the operating time (t_{op}) less than 102 h and then gradually decreased to about 60 % by 484 h, as shown in Fig. 1. For elucidating the cause for the initial degradation (t_{op} < 102 h), complementary electrical, time-resolved photoluminescence (TRPL), and impurity characterizations were carried out making a connection with the energy band profiles.

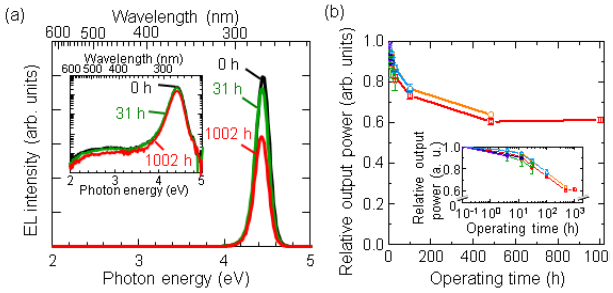

Figure 1 (a) Room-temperature EL spectra of the 275-nm-band $Al_xGa_{1-x}N$ QW LEDs before and after the operation (t_{op} = 0, 31, and 1002 h). (b) Relative optical output power of the LEDs as a function of t_{op}.

The initial degradation was accompanied by the increases in both the forward current (I_F) below the turn-on voltage (V_D) and reverse leakage current (I_R). These results are consistent with those reported previously [1-5]. Because the weak-excitation room-temperature PL lifetime for the near-band-edge emission (τ_{PL}^{NBE}) using the QW-selective TRPL showed only slight change by the operation at least until 1002 h, the initial degradation is attributed essentially to the decrease in carrier injection efficiency ($\eta_{injection}$). From the correlation between the energy band profiles and H concentration profiles before and after the operation, the $\eta_{injection}$ reduction is ascribed to be due to depassivation of initially H-passivated preexisting nonradiative recombination centers (NRCs) in a Mg-doped p-type $Al_{0.85}Ga_{0.15}N$ electron blocking layer (EBL) caused by certain breaking of H bonds and the electric field induced drift of H^+. According to our database on the species of vacancy-type defects acting as NRCs in AlN [6] and GaN [7], vacancy clusters comprised of a cation vacancy (V_{III}) and nitrogen vacancies (V_N), such as $V_{III}(V_N)_{2\sim4}$, are the most suspicious origins of the NRCs in the Mg-doped p-type AlGaN layers [8].

This work was supported by MOE program for implementation of innovative infection-control and digital technologies with low CO_2 emissions and MEXT Crossover Alliance, Japan.
[1] C. Moe *et al*., Appl. Phys. Lett. **96**, 213512 (2010). [2] M. Meneghini *et al*., Microelectron. Reliab. **50**, 1538 (2010). [3] A. Pinos *et al*., J. Appl. Phys. **109**, 103108 (2011). [4] F. Piva *et al*., Photonics Res. **8**, 1786 (2020). [5] J. Glaab *et al*., J. Appl. Phys. **131**,014501 (2022). [6] A. Uedono *et al*., J. Appl. Phys. **105**, 054501 (2009); J. Appl. Phys. **128**, 085704 (2020). [7] S. F. Chichibu *et al*, Appl. Phys. Lett. **86**, 021914 (2005); J. Appl. Phys. **123**, 161413 (2018); Appl. Phys. Lett. **112**, 211901 (2018). [8] S. F. Chichibu *et al*, Appl. Phys. Lett. **122**, 201105 (2023). Author for correspondence: chichibulab@yahoo.co.jp

Supplementary Information

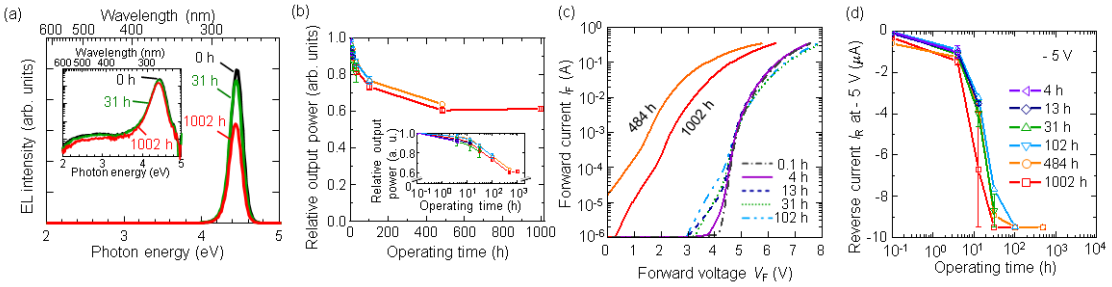

Fig. S1: (a) Room-temperature EL spectra of the 275-nm-band $Al_xGa_{1-x}N$ MQW LEDs before and after the operation (t_{op} = 0, 31, and 1002 h). (b) Relative optical output power of the LEDs as a function of t_{op}. (c) Forward current (I_F) - voltage (V_F) characteristics and (d) reverse current (I_R) at V= - 5 V for the LEDs as a function of t_{op}.

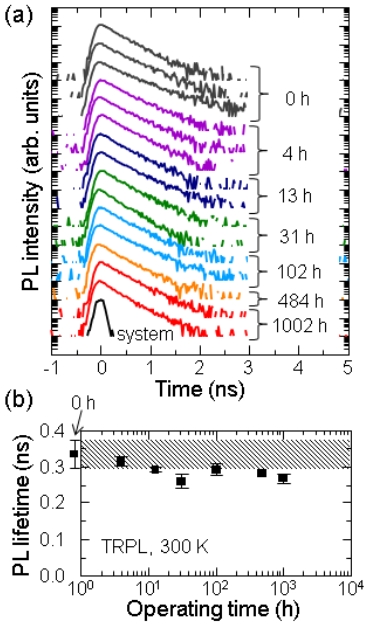

Fig. S2: (a) Room-temperature NBE PL intensities for a series of LED chips as functions of time after excitation (x-axis) and t_{op}. (b) Room-temperature τ_{PL}^{NBE} of the LED chips as a function of t_{op}. Shaded zone indicates τ_{PL}^{NBE} for a series of pristine LED chips showing little but distinguishable individual differences.

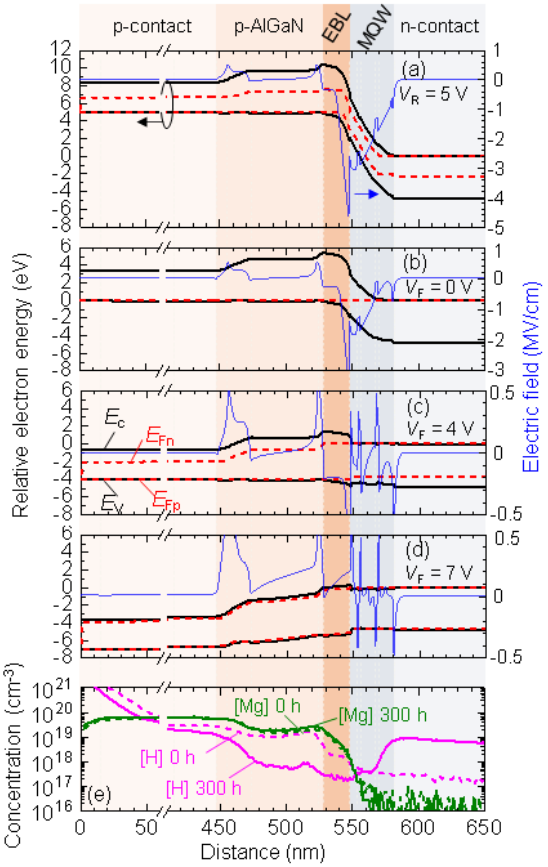

Fig. S3: Energy band profiles (black lines) and gross electric field (F) distributions (blue lines) of the LEDs calculated for (a) V_R = 5 V, (b) V_F = V_R = 0 V, (c) V_F = 4 V, and (d) V_F = 7 V, where E_{Fn} and E_{Fp} represent quasi Fermi levels for the electron and hole, respectively. In panels (a) - (d), relative electron energies are shown on left vertical axes and the electric fields ($F = -dE/dx$) are shown on right vertical axes, where positive F value indicates that F points from the surface (p) side to the bulk (n) side. (e) Concentration profiles of Mg ([Mg]) (green) and H ([H]) (magenta) quantified by SIMS measurement before (dotted lines) and after (solid lines) the operation for t_{op} = 300 h.

Impact of Interfacial Defects and Lattice Strain on NbN_x Films for Integration with Wide Bandgap Semiconductors

A. Drechsler[1, 2], P. Shea[1], and A. Christou[2]

[1] [1]*Northrop Grumman Mission Systems, ATL, Linthicum, MD, USA*

[2] *Department of Materials Science and Engineering, University of Maryland, College Park, MD, USA*

Niobium nitride (NbN) films have garnered significant attention due to their high critical temperature (T_c) and their usage in infrared-sensitive superconducting nanowire single photon detectors (SNSPDs). Devices fabricated from NbN have demonstrated single photon detection to mid-wave infrared wavelengths, which unlocks possibilities for novel applications such as long-range laser detection and ranging (LiDAR), interferometry of planetary emissions, quantum key decryption, and optical communications. To expand beyond a laboratory, however, these devices must be fabricated into focal plane arrays (FPAs), requiring integration with semiconducting device materials. In this work, we report progress on achieving a device structure comprised of a NbN SNSPD monolithically integrated with a wide bandgap semiconductor-based amplifier. This investigation is motivated by recent reports of monolithic integration of NbN with aluminum nitride (AlN) to provide a superconducting load for an amplifier [1].

NbN films for SNSPDs must be thin, typically <<100 nanometers. As a result, the film quality and defectivity, and ultimately SNSPD performance, are highly correlated to the interface between the NbN film and underlying lattice, lattice-mismatch strain, and deposition parameters of the NbN processing. In this talk, we investigate the impacts of the semiconducting interface on the NbN films utilized for SNSPD fabrication through XRD of grown films, AFM surface studies, cathodo-luminesce (CL), and TEM analysis. To optimize this interface, similar materials 6H-SiC (3.57% lattice mismatch) and wurtzite GaN (6.6% lattice mismatch) chosen to minimize intrinsic defect sources. XRD analysis of grown films indicates that growth on these substrates is possible with long range crystallinity, suggesting the presence of epitaxial growth for high quality films. Optimization of the stress of the film due to the lattice mismatch with the substrate is also investigated by modifying the growth temperature, pressure, and power to reduce lattice strain-induced defects. The presence of threading and other dislocations stemming from interface defects analyzed through CL and TEM will also be discussed.

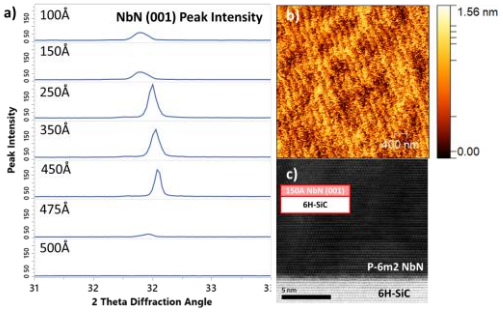

Figure 1: (001) NbN peak intensity measured in XRD, (b) AFM analysis of ultra-thin NbN films after growth, c) TEM of NbN/6H-SiC interface.

[1] R. Yan, G. Khalsa, S. Vishwanath, Y. Han, J. Wright, S. Rouvimov, D.S. Katzer, N. Nepal, B.P. Downey, D. Muller, H.G. Xing, D.J. Meyer, and D. Jena, Nature. **555,** 7695 (2018)

[+] Author for correspondence: adrechs@umd.edu

Supplementary Pages (Optional)

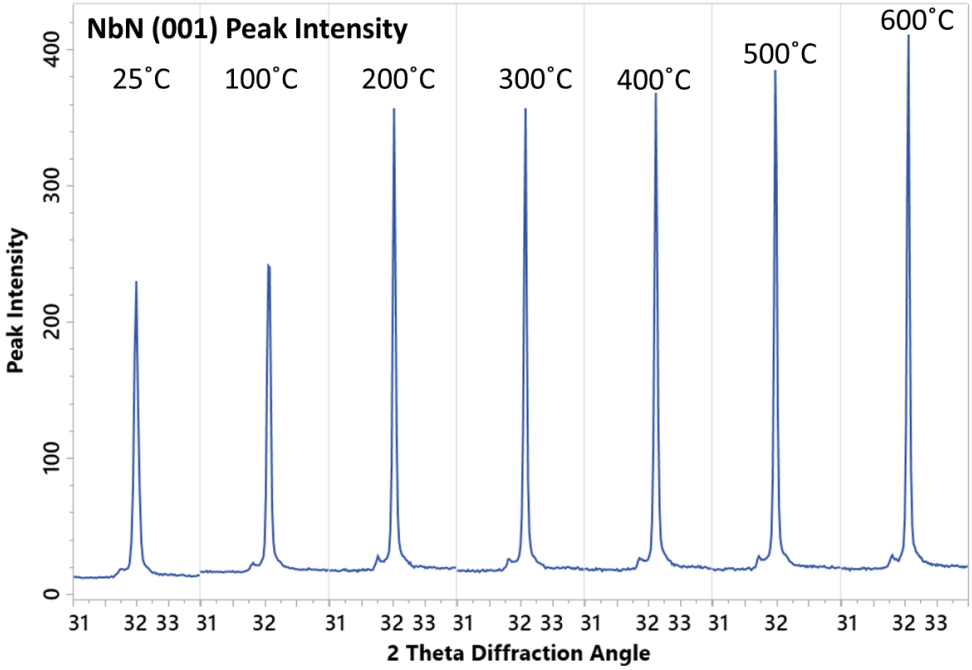

Figure 2: NbN (001) peak intensity at 250 angstroms thickness as a function of deposition temperature, indicating that increased growth temperature improves crystallinity.

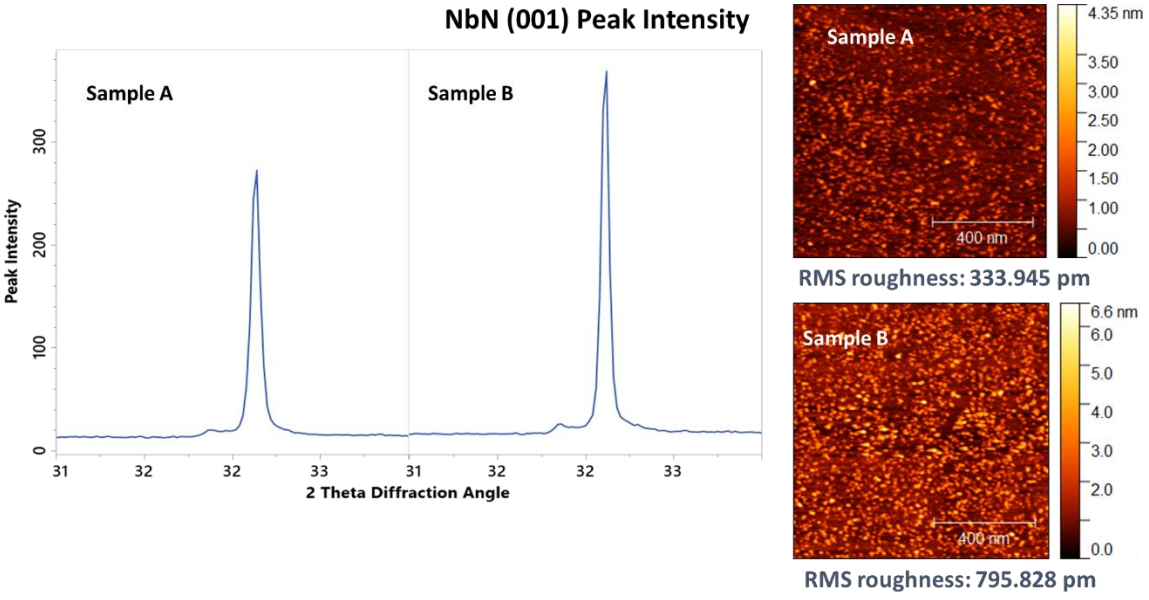

Figure 3: NbN (001) peak intensity compared to surface roughness of underlying semiconductor susbtrate, indicating the increased roughness at the interface promotes longer range crystalline growth.

Supplementary Pages (Optional)

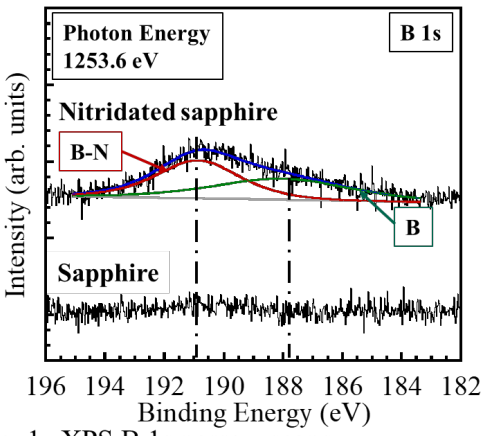

Fig. 1. XPS B 1s narrow scans for nitridated sapphire and bare sapphire

Fig. 1. XPS spectra (B1s) of sapphire w/o nitridation.

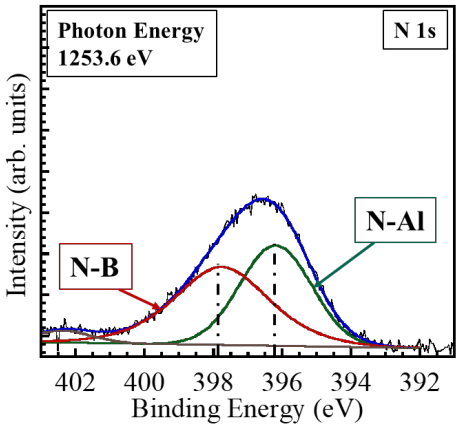

Fig. 2. XPS N 1s narrow scans for nitridated sapphire

Fig. 2. XPS spectra (N1s) of sapphire with nitridation.

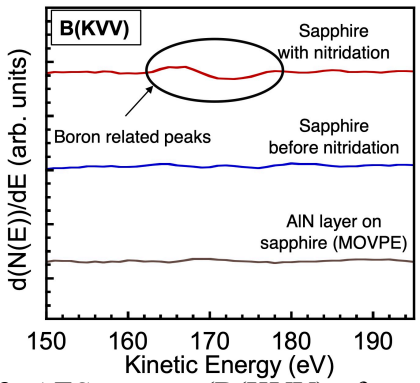

Fig. 3. AES spectra (B(KVV) of sapphire w/o nitridation. Those of AlN/sapphire grown by MOVPE is also shown.

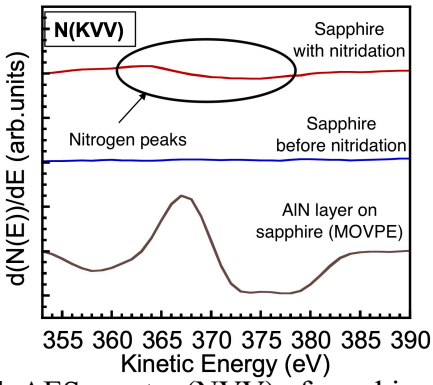

Fig. 4. AES spectra (NVV) of sapphire w/o nitridation. Those of AlN/sapphire grown by MOVPE is also shown.

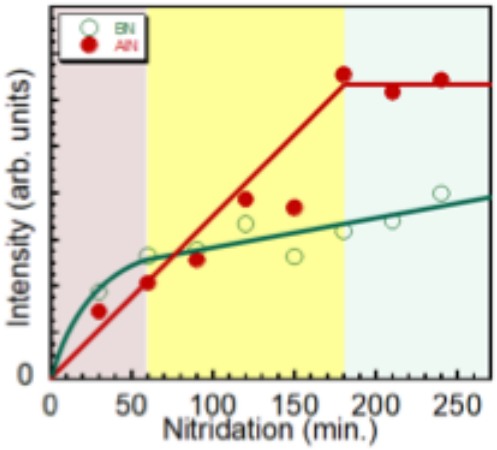

Fig. 5. Intensities of AlN and BN as a function of nitridation time.

Photoluminescence maps of surface defects in β-Ga_2O_3

M.D. McCluskey,[1,2,+] J. Huso,[2] C. Remple,[1] J.S. McCloy,[1] S. Rebollo,[3] S. Krishnamoorthy,[3] and J.S. Speck[3]

[1] Washington State University, Pullman, WA 99164-2814
[2] Klar Scientific, Pullman, WA 99163
[3] University of California, Santa Barbara, CA 93106

Monoclinic gallium oxide (β-Ga_2O_3) is an ultrawide bandgap semiconductor with potential applications in power electronics [1]. Photoluminescence (PL) spectroscopy is an important method to characterize dopants and defects in this material. Common features in the PL spectrum include the intrinsic UV band (Fig. 1), blue and green bands that involve donor-acceptor pairs, and red emission due to Cr^{3+} impurities.

PL mapping with excitation wavelengths ranging from 266 to 532 nm reveals the spatial distribution of these features with micron resolution. In Czochralski-grown β-Ga_2O_3, the Cr^{3+} emission intensity shows striations that are attributed due to inhomogeneities during growth [2]. In addition to defects in the bulk, PL microscopy has revealed several specific defects on the surface. Some of these localized centers are very bright UV emitters [3].

Homoepitaxial layers show defects that are observed via the shifts in the PL band, likely due to the strain field around a dislocation core. Damage due to high-intensity laser pulses results in significant changes in the intensity and energy of the UV band (Fig. 2). *In situ* PL spectroscopy performed with a pulsed 266 nm laser shows characteristic emission peaks attributed to Ga atoms ablated from the surface.

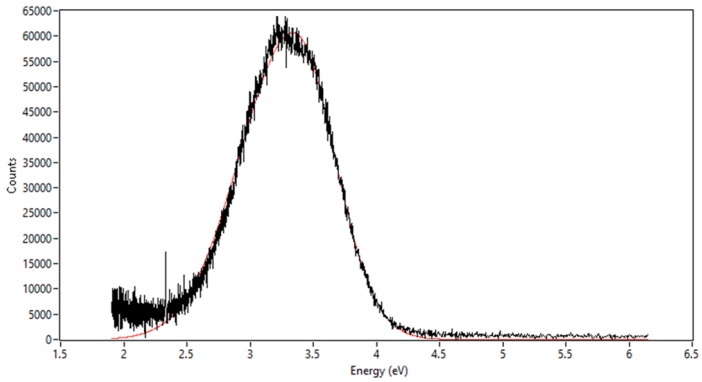

Fig. 1. UV band emission from β-Ga_2O_3 epilayer (266 nm excitation, room temperature).

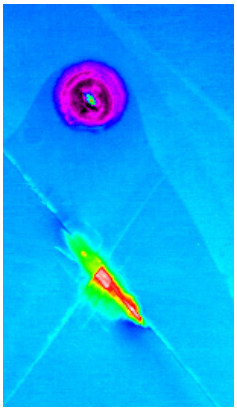

Fig. 2. PL map of the UV-band intensity for a damaged β-Ga_2O_3 epilayer (image width ~ 0.8 mm).

[1] M.D. McCluskey, J. Appl. Phys. **127**, 101101 (2020).
[2] C. Remple, J. Huso, and M.D. McCluskey, AIP Advances **11**, 105006 (2021).
[3] J. Huso, M.D. McCluskey, Y. Yu, Md. M. Islam, and F. Selim, Scientific Reports **10**, 21022 (2020).

[+] Author for correspondence: mattmcc@wsu.edu

Epitaxial growth and properties of wide bandgap *p*-type $NiGa_2O_4$ on β-Ga_2O_3 for high voltage *p-n* heterojunctions with superior performance at elevated temperatures

Kingsley Egbo[1], Brooks Tellekamp[1], William A. Callahan[1,2], Andriy Zakutayev[1]

[1]National Renewable Energy Laboratory, Golden, CO 80401, USA

[2]Advanced Energy Systems Graduate Program, Colorado School of Mines, Golden, CO 80401, USA

Gallium oxide (β-Ga_2O_3) is a promising wide bandgap oxide semiconductor material with properties well-suited for high power electronics, and recent results show superior high voltage performance compared to the commercial state of the art [1],[2]. Due to the difficulty in the *p*-type doping of Ga_2O_3, unipolar devices based on Ga_2O_3 are prevalent. Several studies have explored bipolar devices using polycrystalline *p*-type oxides such as Nickel oxide and Tin (II) oxide grown on Ga_2O_3 to form heterojunctions[3][4]. However, resulting interface defects and grain boundaries decrease the electrical performance of these devices which directly affects the power device performances, such as breakdown characteristics, on-resistance, and mobility. Hence, the development of high-quality heteroepitaxy of a *p*-type layer with low structural defects on *n*-type Ga_2O_3 is essential to improve device performance in Ga_2O_3-based bipolar devices. For operation at high temperature, thermodynamically stable interfaces are also critical. Recent observations show that $NiGa_2O_4$ forms as a thermodynamical reaction product between Ga_2O_3 and NiO at the p-n heterojunction interface during high temperature operation. Hence the possibility of developing a *p*-type $NiGa_2O_4$ on Ga_2O_3 can circumvent this interface reaction and lead to the development of thermodynamically stable high temperature devices.

In this work, we demonstrate the epitaxial growth of wide bandgap *p*-type $NiGa_2O_4$ thin films on Ga_2O_3 and the device performance of vertical *p-n* heterojunction diodes processed using these heterostructures. Undoped $NiGa_2O_4$ thin films were grown on three different orientations of β-Ga_2O_3 wafers and on a reference Al_2O_3 substrates by pulsed laser deposition. Structural characterizations of the $NiGa_2O_4$ thin films show that 002-oriented $NiGa_2O_4$ grows epitaxially on β-Ga_2O_3 (100) while $NiGa_2O_4$(220) was stabilized on β-Ga_2O_3 (010) orientation. But thin films of $NiGa_2O_4$ grown on Ga_2O_3(001) was polycrystalline. The reflection high energy diffraction (RHEED) patterns during growth were streaky indicating relatively flat surfaces. A bandgap of ~3.95 eV is obtained for $NiGa_2O_4$ thin films from spectroscopic ellipsometry.

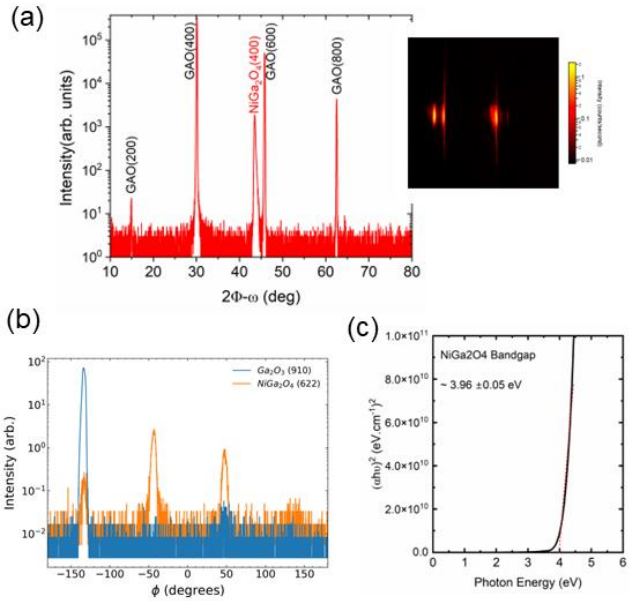

+ Author for correspondence: Kingsley.Egbo@nrel.gov

The fabricated $NiGa_2O_4$/β-Ga_2O_3 vertical p-n heterojunction devices demonstrated good specific on-resistance, excellent temperature dependent reverse leakage current and lower on-voltage compared to widely used NiO-Ga_2O_3 heterojunctions. These performances demonstrate that $NiGa_2O_4$/β-Ga_2O_3 p-n heterojunction diodes can be promising for high power devices with low on state power dissipation capable of operating at extreme environments.

Figure 1(a) Wide angle 2theta-omega scan of $NiGa_2O_4$(200) grown on Ga_2O_3(100). Inset shows a 2D frame showing single crystalline growth (b) Phi scan of the $NiGa_2O_4$ and Ga_2O_3 layers (c) Absorption coefficient of $NiGa_2O_4$ thin film obtained from spectroscopic ellipsometry measurement.

[1] S. J. Pearton *et al.*, "A review of Ga2O3 materials, processing, and devices," *Appl. Phys. Rev.*, vol. 5, no. 1, p. 011301, Mar. 2018, doi: 10.1063/1.5006941.

[2] A. J. Green *et al.*, "β-Gallium oxide power electronics," *APL Mater.*, vol. 10, no. 2, p. 029201, Feb. 2022, doi: 10.1063/5.0060327.

[3] K. Tetzner *et al.*, "SnO/β-Ga2O3 heterojunction field-effect transistors and vertical p–n diodes," *Appl. Phys. Lett.*, vol. 120, no. 11, p. 112110, Mar. 2022, doi: 10.1063/5.0083032.

[4] Sohel, S. H. *et al.* Gallium Oxide Heterojunction Diodes for Improved High-Temperature Performance. Preprint at http://arxiv.org/abs/2204.00112 (2022)

Supplementary Information:

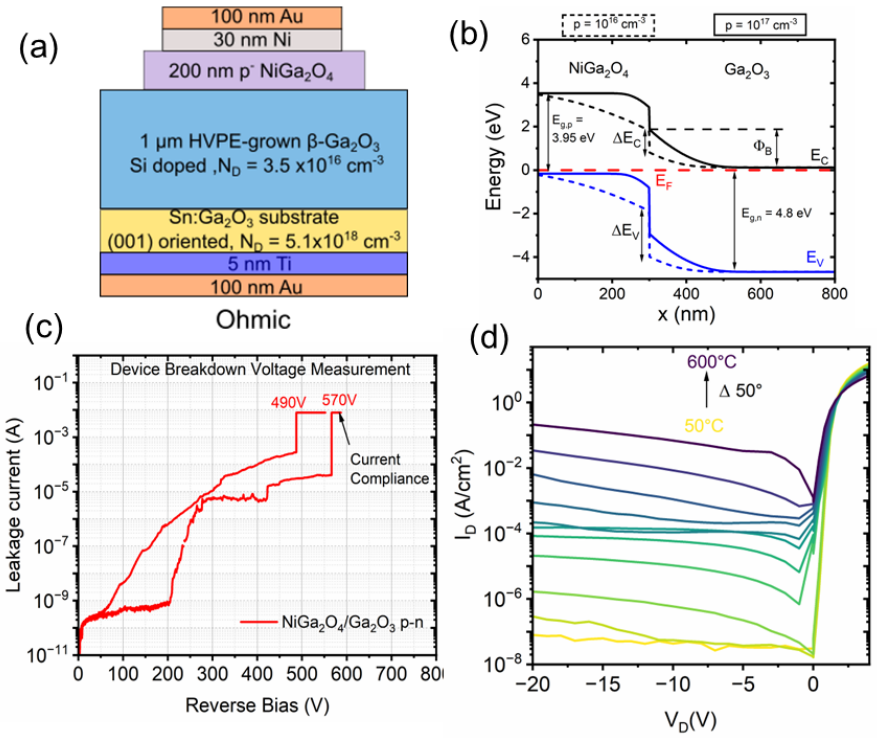

Figure 2(a) Schematic of the device structure for fabricated $NiGa_2O_4$/Ga_2O_3 heterojunction diode (b) Estimated band diagram of the *p*-$NiGa_2O_4$/*n*-Ga_2O_3 junction using values from literature and determined bandgap (c) Room temperature breakdown of two *p*-$NiGa_2O_4$/*n*-Ga_2O_3 diodes (d) Temperature dependent *J-V* characteristics of the diode showing rectification at 600°C operating temperature.

Quantum Oscillations in GaN/AlN 2D Hole Gas and Extraction of Light Hole Effective Mass

C. Chang,[1] J. Dill,[1] Z. Zhang,[1] Scott Crooker,[2] Oscar Ayala Valenzuela,[2] Ross McDonald,[2] D. Jena,[1] H.G. Xing[1]

[1] Cornell University, Ithaca, NY, USA
[2] Los Alamos National Laboratory, Los Alamos, NM, USA

Gallium Nitride (GaN) has been a leading contender in commercial high-frequency and high-power applications due to its internal polarization field and a wide bandgap of 3.4 eV [1]. However, while n-channel high-electron mobility transistors (HEMT) based on GaN's polarization-induced two-dimensional electron gas (2DEG) progress towards higher performance, its p-type counterpart has been lagging due to the low mobility of the polarization-induced two-dimensional hole gas (2DHG), hindering the development of GaN-based CMOS and an extraction of hole effective mass by Shubnikov de-Haas (SdH) oscillations and cyclotron resonance. In the absence of reliable and uniform experimental data, researchers have had to rely on theoretical calculations [3].

In this talk, we report the first observation of SdH oscillations in any p-type GaN platform and subsequent extraction of hole effective mass. Here, a technique pioneered by Chaudhuri *et. al.* [2] is used to form a high-density (~5×10^{13} cm^{-2} at 300 K) 2DHG at the heterointerface between GaN and a AlN substrate via the large internal electric fields induced by spontaneous and piezoelectric polarization. Magnetoresistance measurements up to 63 T is performed at the National High Magnetic Field Laboratory Pulsed Field Facility, showing Shubnikov de-Haas (SdH) oscillations with an onset at around B=25 T (Fig. 1). Fig. 2a shows R_{xx} with a polynomial background subtracted plotted against B^{-1} and Fig. 2b shows its power spectrum. A strong peak is located at f =168 T in the power spectrum at all temperatures corresponding to a density of 8.2×10^{12} cm^{-2}. In lower magnetic fields (< 9T), $R_{xx}(B)$ and $R_{xy}(B)$ are fitted to a classical two-band model (Fig. 3), revealing the coexistence of two carrier populations – low-mobility (~230 cm^2/Vs) heavy holes with a density of 4.2×10^{13} cm^{-2} and high-mobility (~1400 cm^2/Vs) light holes with a density of 7×10^{12} cm^{-2} in agreement with the density extracted from SdH frequency. Attributing the oscillations to the light holes, we extract their effective mass from the temperature-dependence of the amplitudes, yielding a value of 0.48 ± 0.02 m_0.

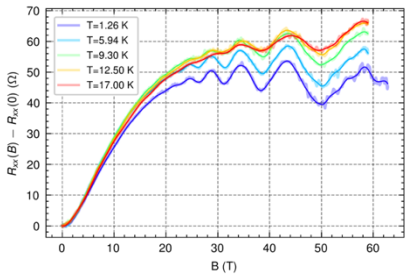

Fig 1. SdH oscillations in R_{xx}.

References
[1] S. Bader *et al*., IEEE. Trans. Electron Devices, **67**, 4010 (2020).
[2] R. Chaudhuri *et al.*, Science **365**, 1454 (2019).
[3] B. Santic, Semicond. Sci Technol. **18**, 219 (2003)

+ Author for correspondence: cc2737@cornell.edu

Suplementary Pages

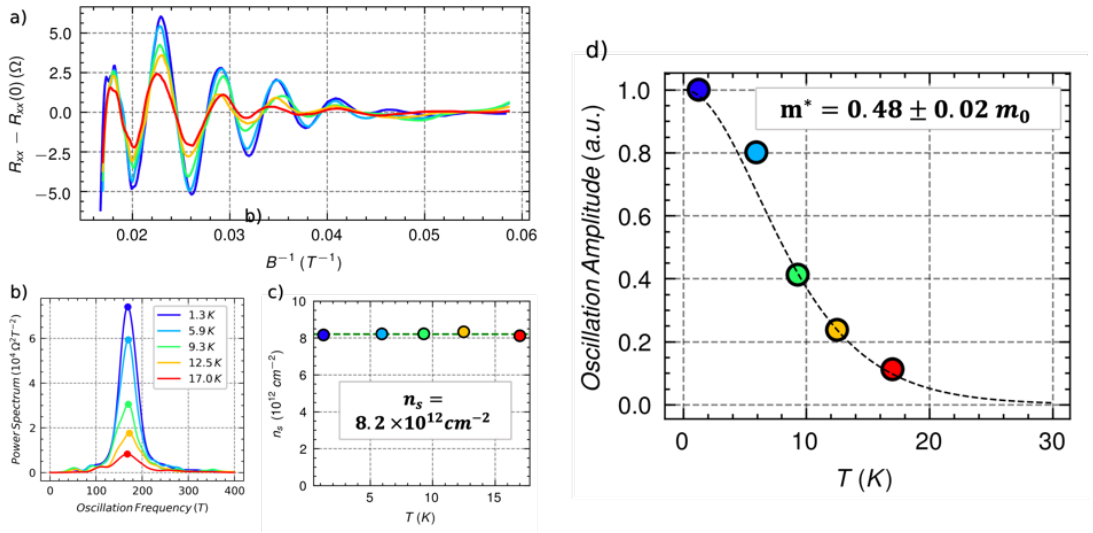

Fig 2. (a) R_{xx} vs B curves with polynomial background subtraction plotted against B^{-1}. (b) Power spectrum of (a), showing a single peak at f=168 T for all temperatures. (Inset) Density obtained from the frequency of the peak: n_s~8.2e12 cm^{-2}. (c) L-K fit of power spectrum amplitude as a function of T, yielding $m^*=0.48 \pm 0.02\ m_0$.

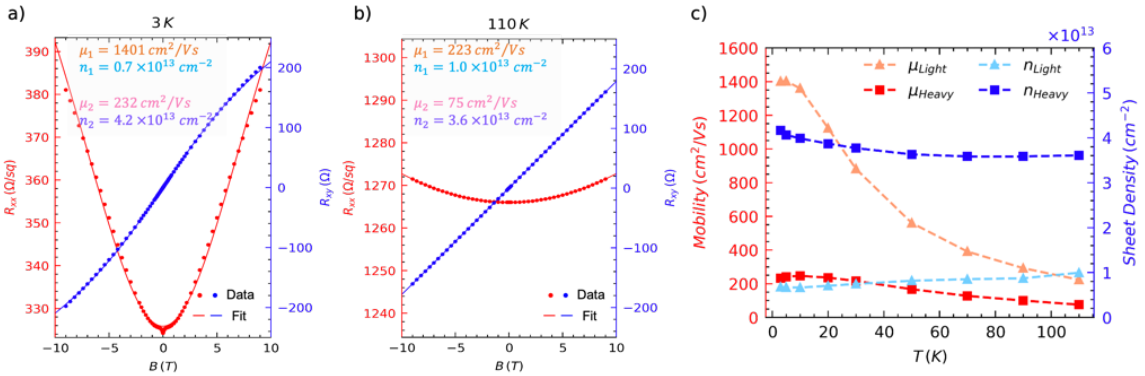

Fig 3. R_{xx} and R_{xy} vs B at (a) 3 K and (b) 110 K. Solid lines are simultaneous fits to the two-carrier Drude model. The best-fit values are shown. (c) Best-fit parameters as a function of temperature.

Reduced Metal Contact Resistances for Moire MoS_2 Interfaces

J Robertson[1], Z Zhang[2], J Chen[1], Y Guo[2],
1

[1] Engineering Dept, Cambridge University, Cambridge CB3 0FA, UK
[2] Wuhan University, Wuhan 430072, China.

We show how rotational Moire interfaces for electrical contacts between metals and monolayer MoS_2 can create weakly bonded physisorptive interface sites with weaker Fermi-level pinning. This creates smaller n-type Schottky barrier heights, giving the lowest contact resistances for In and a noble metal Ag, as seen experimentally, but previously unexplained. Analogous sites are found for p-type interfaces on WSe_2.

Scaling of semiconductor devices requires lower contact resistances by reducing Schottky barrier heights (SBH) for metals on transition metal dichalcogenide (TMD) contacts. Duan [1] achieved unpinned Fermi levels and physisorbed interfaces by using metal films mechanically transferred onto unmanufacturable exfoliated MoS_2. This effectively increases the interfacial bond length and makes physisorbed interfaces [2]. We suggest longer bonds can be formed by making Moire interfaces between contacts and TMDs.

The TMD lattice allows an alternative way to create longer interfacial bonds using Moire interfaces. These apply a rotational twist between MoS_2 layer and the metal contact layer [2]. There are three types of interface, on-top site (T), a hollow site (H), and Moire sites (M), Fig. 1. We calculate the interfacial binding energy of each metal interface, and find the most stable configuration, as a function of metal work function φ. The data shows two zones of physi- or chemi-sorptive interfaces. We then calculate SBHs for the various bonding sites for each contact metal and show these as a function of φ. The previous scattered pattern of SBHs sorts into two trends; most SBHs have a slope with φ of 0.24 for T or H interfaces. But Moire sites have a clear depinning trend for E_F, with the slope increasing to 0.37 (Fig. 2). This gives a small n-SBH to the MoS_2 conduction band, and lower contact resistances for In and Ag, as seen experimentally. Similar results are found for p-contacts on WSe_2.

[1] Y Liu…X Duan et al, Nature 393 696 (2017); [2] Z Zhang, et al, ACS AMI 14 11903 (2022)

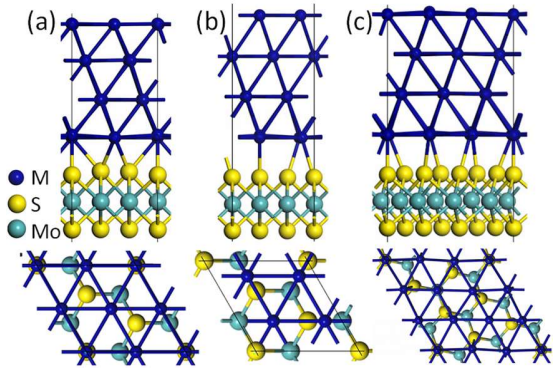

Fig. 1(a) Side and top view of on-top (b) hollow and (c) Moire interfacial sites.

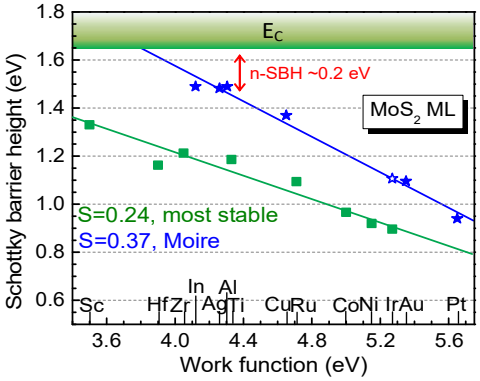

Fig. 2. SBH fit of T,H sites, and of M sites with only physisorption, omitting stars for Co, Ni. Ef depinning factor varies from 0.20 to 0.37.

A Generalized and Modular Approach to Tunnel-Junction Spectroscopy for Quantum Systems

M. Kavand,[1] Z. Phillips,[1] M. Hamilton,[1] W. Koll,[1] E. Perez-Hoyos,[1] D. Freedman,[2] M. Flatté,[3] J.A. Gupta, E. Johnston-Halperin[1]

[1] Department of Physics, The Ohio State University, Columbus, OH

[2] Department of Chemistry, Massachusetts Institute of Technology, Cambridge, MA

[2] Department of Physics, University of Iowa, Iowa City, IA

We present a generalized and modular scheme for tunneling spectroscopy of 0D quantum systems based on the exfoliation and stacking of 2D heterostructures. In this scheme, layers of graphene/graphite (gr) and hexagonal boronitride (hBN) are assembled into a gr/hBN/hBN/gr tunnel junction. The differential conductance (dI/dV) of this structure is sensitive to both direct tunneling through the insulating hBN and resonant tunneling through any impurity states within the bandgap. As a proof of principle, we demonstrate the ability to resolve a variety of structural defects in hBN as well as the direct observation of the HOMO and LUMO states of vanadyl pthalocyanine (VOPc) encapsulated at the interior hBN/hBN interface of the heterostructure (Fig. 1). The VOPc tunneling spectra directly correlate with scanning tunneling microscopy (STM) of witness samples and are consistent with density functional theory (DFT) of VOPc. This technique is extensible to a wide variety of 0D systems encapsulated at the hBN/hBN interface, including electrically (or redox) active molecular systems, adatoms, and point defects in 2D materials. This generality and flexibility provides an exciting opportunity for both electronic/structural characterization of these quantum states as well as potential applications in quantum information.

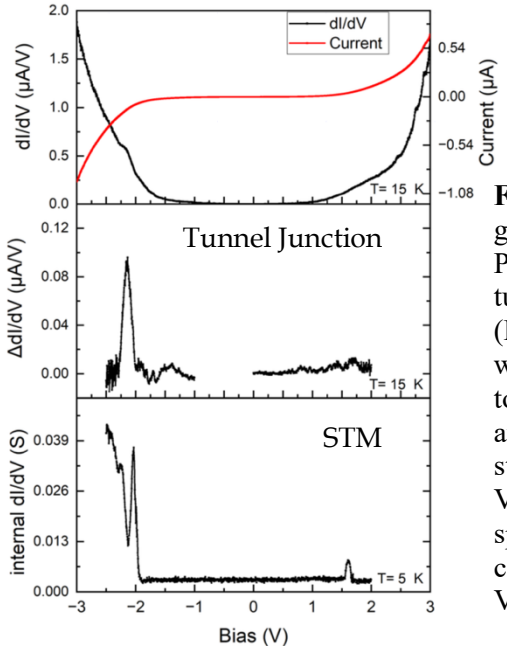

Figure 1. (Top Panel) IV and dI/dV acquired from a graphene/hBN/VOPc/hBN/graphene tunnel junction. Peaks in dI/dV correspond to steps in IV as resonant tunneling through VOPc molecular orbitals is allowed. **(Middle Panel)** Same dI/dV data from Top Panel, but with the direct tunneling background removed by fitting to a polynomial background. There is a clear resonance at -2.1 V representing the VOPc HOMO, and additional structure at positive bias that may correspond to the VOPc LUMO. **(Bottom Panel)** STM based tunneling spectra of a similar structure (graphite/hBN/VOPc) confirming the HOMO and LUMO energies of the VOPc.

[+] Author for correspondence: Johnston-Halperin.1@osu.edu

Supplemental Document Author Index

Bold page numbers indicate presenter

Supplemental Document Author Index